

# **Gamma-Hadron Classification for the Ground Based Atmospheric Cherenkov Telescope MACE**

By

**MRADUL SHARMA**

PHYS01201104002

Bhabha Atomic Research Centre,  
Mumbai - 400085,

**INDIA**

*A thesis submitted to the  
Board of Studies in Physical Sciences*

*In partial fulfillment of requirements  
For the Degree of*

**DOCTOR OF PHILOSOPHY**

of

**HOMI BHABHA NATIONAL INSTITUTE**



**June 2017**



# Homi Bhabha National Institute

## Recommendations of the Viva Voce Board

As members of the Viva Voce Board, we certify that we have read the dissertation prepared by Mr. Mradul Sharma entitled "Gamma-Hadron Classification for the Ground Based Atmospheric Cherenkov Telescope MACE" and recommend that it may be accepted as fulfilling the thesis requirement for the Degree of Doctor of Philosophy.

---

Chairman: Prof. S. Basu

Date: *S. Basu*  
8/6/17

---

Guide/Convener: Prof. D. K. Koul

Date: 8/6/17 *D. K. Koul*

---

Examiner: Prof. A. Kembhavi

Date: 08/06/2017 *A. Kembhavi*

---

Member: Prof. B. S. Acharya

Date: 8/6/2017 *B. S. Acharya*

---

Member: Prof. S. Bose

Date:

Final approval and acceptance of this thesis is contingent upon the candidate's submission of the final copies of the dissertation to HBNI.

I hereby certify that I have read this thesis prepared under my direction and recommend that it may be accepted as fulfilling the thesis requirement.

Date:

Place: Bhabha Atomic Research Centre

Mumbai

Prof. D. K. Koul

Guide

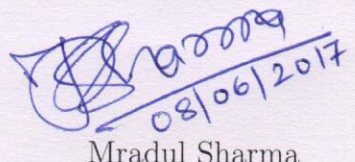
*08.06.2017*



## STATEMENT BY AUTHOR

This dissertation has been submitted in partial fulfillment of requirements for an advanced degree at Homi Bhabha National Institute (HBNI) and is deposited in the Library to be made available under rules of the HBNI.

Brief quotations from this dissertation are permissible without special permission, provided that the source is appropriately acknowledged. Requests for permissions for extended quotation from or reproduction of this manuscript in part or in whole may be granted by the Competent Authority of HBNI when in his or her judgement the proposed use of the material is in the interests of scholarship. In all other instances, however, permission must be obtained from the author.



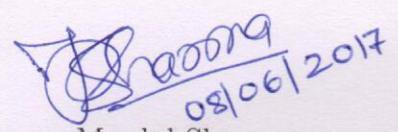
A handwritten signature in blue ink, appearing to read "Mradul Sharma". Below the signature, the date "08/06/2017" is written diagonally across the signature.

Mradul Sharma



## DECLARATION

I hereby declare that the investigations presented in this thesis have been carried out by me. The work is original and has not been submitted earlier as a whole or in part for a degree/diploma at this or any other Institution/University.



Mradul Sharma  
08/06/2017



## List of Publications arising from the thesis

### List of Publications relevant to this thesis: 3

#### Refereed Journals: 3

1. Gamma/hadron segregation for a ground based imaging atmospheric Cherenkov telescope using machine learning methods: Random Forest leads

**Mradul Sharma**, Jitadeepa Nayak, Maharaj Krishna Koul, Smarajit Bose and Abhas Mitra

*Research in Astronomy and Astrophysics, 14, 1491-1503 (2014)*

2. Validation of a new background discrimination method for the TACTIC TeV -ray telescope with Markarian 421 data

**Mradul Sharma**, J. Nayak, M.K. Koul, S. Bose, Abhas Mitra, V.K. Dhar, A.K. Tickoo, R. Koul

*Nuclear Instruments and Methods in Physics Research, A, 770, 42-47 (2015)*

3. Sensitivity estimate of the MACE gamma ray telescope

**Mradul Sharma**, Chinmay B., Bhatt N., Bhattacharyya S., Bose S., Abhas Mitra, Koul R., Tickoo A. K., Rannot, R. C.

*Nuclear Instruments and Methods in Physics Research, A, 851, 125-131 (2017)*

#### Conference Papers: 2

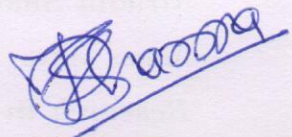
1. Gamma/Hadron segregation using Random Forest method in ground based Gamma Ray Astronomy: Random Forest Leads

**Mradul Sharma**, J. Nayak, M. K. Koul, S. Bose, N. G. Bhatt and Abhas Mitra  
*“31st Astronomical Society of India Meeting (ASI-2013)” Trivandrum, India, (2013)*

2. Application of Random Forest method in gamma-hadron segregation using Markarian(Mrk) 421 and Crab Nebula data of 2005-2006 observed by the TACTIC telescope

Mradul Sharma J. Nayak, M. K. koul, S. Bose, N. G. Bhatt, Abhas Mitra

*"National Symposium on VHE Gamma Ray Astronomy 25-27 November 2013", BARC, Mumbai, India*



Mradul Sharma



**Dedicated  
to  
My Parents**



I would never die for my beliefs because I might be wrong.

Bertrand Russell



## ACKNOWLEDGEMENTS

“In ordinary life, we hardly realize that we receive a great deal more than we give, and that it is only with gratitude that life becomes rich.” Dietrich Bonhoeffer

First of all, I would like to express my deep sense of gratitude to my ex-thesis adviser, Prof. Abhas Mitra. His sharp observations, intuitiveness of ideas, never say dying spirit and enthusiasm inspires me even today. After his superannuation, I was given a chance by Prof. D. K. Koul to complete my thesis work under his supervision. His unconditional support helped me greatly to complete my research work without any problem.

I want to express my sincere thanks to my doctoral committee who had been extremely supportive during the course of my thesis work. I had one of the most remarkable set of people in my doctoral committee. Professor Smarajit Bose is one of such pillars who taught me the complex maize of machine learning methods. He invited me to Indian Statistical Institute (ISI), Kolkata few times during the course of my thesis work. Prof. Bose spent long hours to teach me the fundamentals of the field. He helped me to understand the field by many examples, demonstrated by her project student: Miss. Jitadeepa Nayak. I am very thankful to Ms. Nayak for all her efforts.

Professor B. S. Acharya, another doctoral committee members, is one of the most remarkable people I found during various phases of my work. His constant suggestions to carry out simulation studies to understand various aspects of MACE telescope brought much needed clarity to understand MACE like high altitude atmospheric Cherenkov systems. Whenever I needed his time, he invited me the same day to TIFR (Tata Institute of Fundamental Research).

But let me add that the chairman of my doctoral committee, Prof. Saibal Basu, is the one who helped me to reach the stage of submitting my final thesis. I just can not imagine myself at this stage without his firm support. It will not be a hyperbole to say that the world is so much beautiful because of people like him. I will forever remain indebted to him for showing me, by example: what it means to be a support.

I am extremely grateful to Prof. A. K. Tickoo for teaching me the tricks of the trade of

data analysis of atmospheric Cherenkov telescope. I am also very thankful to my present division head, Dr. R. C. Rannot for his constant support. Despite being extremely busy in the installation of MACE telescope, he was always available whenever needed. I would also like to express my gratitude to Mr. Ramesh Koul, my ex-doctoral committee member and ex-Head ApSD for his all round support.

I am extremely thankful to Dr. Subir Bhattacharyya and Mr. Nilay Bhatt for their constant help, support and encouragement. Subir introduced me to the wonderful world of astrophysics. He is a wonderful teacher who created a conducive research eco-system. Nilay helped me actively in my PhD work. Many long discussions with him resulted in many insights about the MACE telescope. I am also extremely thankful to Mr. Chinmay with whom many brain storming sessions along with Nilay lead to all round understanding of MACE system performance. My heartfelt appreciation goes to Dr. V. K. Dhar who helped me to understand the intricate field of Artificial Neural Network with great clarity. I am also very thankful to Mr. Nilesh Chouhan for many discussions about the technical aspects of MACE. I also thank Dr. Himali Bhatt for Latex formatting of my thesis and preparing the wordcount maps of each chapter. I also express my gratitude to her for her inputs on thesis. I thank my colleagues Dr. S. Sahayanathan, Dr. K. K. Yadav, Dr. Sagar Godambe, Dr. Nizil, Mr. M. K. Koul, Dr. C. K. Bhat, Mr. Venugopal and Mr. Kishore for lively discussions. Special credit goes to Dr. K. K. Singh for familiarizing me with the paper work related to PhD work.

I am very much indebted to my parents who encouraged me at every stage of my life and supported me in all my endeavors. My father always taught me the virtue of hard work and valued academic excellence over any other craft. I also heartfully thank my sister Vandana and brother Avaneesh who were a part of my every endeavor. I also thank my brother in law: Pravin and sister in law: Alka for their constant support. I also express my heartfelt gratitude to my extended family, my father and mother in law for their boundless love and motivation. I am also thankful to my sister in laws: Sangeeta, Priya, Pooja, Nidhi and brother in laws: Mukesh, Sanjeev, Gauran and Manu. Special thanks to Mukesh who always taught me how not to get bogged down by adverse circumstances and focussing on the bigger picture. He has inspired me in many ways by sharing his deep insights on every query I had. I cherish the love showered on me by our next generation: Priyanshi, Parv, Kittu, Prankur & Preesha.

Finally, I would like to mention that without the presence of my wife, Sonia, I would not have even reached the stage of PhD registration. It was her insistence and persistence, which motivated me to work in the direction of PhD. She was also instrumental in inculcating in me the habit of carrying out the research work systematically. She is a true inspiration. In the serious business of mission mode life, a cool breeze came in the form of my daughter: Jiya. She gave a new meaning to life altogether. Irrespective of how long my day was, her first sight dissolved the entire tiredness of whole day. I feel truly blessed to be surrounded by wonderful people.

I will be truly sorry if by mistake I might have missed someone in my acknowledgments, it is not intentional.



# Contents

<b>Synopsis</b>	<b>v</b>
<b>List of Figures</b>	<b>xvii</b>
<b>List of Tables</b>	<b>xxi</b>
<b>1 VHE <math>\gamma</math> ray Astronomy</b>	<b>1</b>
1.1 Introduction . . . . .	3
1.2 Cosmic rays . . . . .	4
1.3 Spectrum . . . . .	6
1.4 Sources of cosmic rays . . . . .	8
1.5 Gamma rays . . . . .	10
1.5.1 Importance of $\gamma$ -ray astronomy . . . . .	12
1.5.2 $\gamma$ -ray production mechanism . . . . .	13
1.5.2.1 $\pi^0$ decay . . . . .	14
1.5.2.2 Synchrotron Radiation . . . . .	14
1.5.2.3 Inverse Compton Scattering . . . . .	15
1.5.2.4 Bremsstrahlung . . . . .	17
1.5.3 Gamma ray absorption . . . . .	17
1.5.4 $\gamma$ - $\gamma$ interaction . . . . .	18
1.5.4.1 $\gamma$ -ray absorption by pair production . . . . .	20
1.5.5 Cosmic $\gamma$ -ray horizon (CGRH) . . . . .	21
1.5.5.1 Determination of CGRH . . . . .	21
<b>2 Ground based <math>\gamma</math>-Ray Astronomy</b>	<b>23</b>

2.0.6	Ground based observatories . . . . .	25
2.1	Atmospheric Cherenkov Radiation . . . . .	29
2.1.1	Cherenkov light distribution . . . . .	31
2.1.2	Threshold energy for Cherenkov emission . . . . .	33
2.1.3	Height dependent Cherenkov emission . . . . .	33
2.1.3.1	Maximum angle for Cherenkov emission . . . . .	34
2.1.3.2	Cherenkov light pool . . . . .	34
2.1.3.3	Cherenkov light pulse duration . . . . .	35
2.2	Cherenkov Radiation in Extensive Air Showers . . . . .	37
2.2.1	Electromagnetic Showers . . . . .	37
2.2.1.1	Toy model of Electromagnetic showers . . . . .	38
2.2.2	Hadronic Showers . . . . .	40
2.2.3	The Imaging Atmospheric Cherenkov Technique . . . . .	41
2.2.3.1	Basic Principle . . . . .	43
2.2.3.2	Flux sensitivity of Cherenkov telescope . . . . .	45
2.3	Parameterization of Cherenkov Radiation . . . . .	46
2.3.1	Estimation of image parameters . . . . .	49
2.4	The TACTIC Telescope . . . . .	53
<b>3</b>	<b>Various machine learning methods</b>	<b>59</b>
3.1	Introduction . . . . .	61
3.2	Database used in this study . . . . .	64
3.2.1	Image parameters for classification . . . . .	64
3.3	Different classification methods . . . . .	67
3.3.1	Conventional method: Dynamic Supercuts . . . . .	67
3.3.2	Artificial Neural Network . . . . .	68
3.3.3	Naive Bayes Classifier . . . . .	69
3.3.4	Standard Discriminant Analysis . . . . .	70
3.3.5	Support Vector Machine . . . . .	71
3.3.5.1	Support Vector Machines for binary classification problem	72
3.3.5.2	Statement of linear SVM . . . . .	73
3.3.5.3	Optimal hyperplane for linear SVM . . . . .	74

3.3.5.4	Dual formulation . . . . .	76
3.3.5.5	Non linear SVM . . . . .	77
3.3.6	Random Forest Method . . . . .	79
3.3.6.1	Bagging . . . . .	79
3.3.6.2	Random Split Selection . . . . .	80
3.4	Comparison of Classification methods . . . . .	87
3.4.1	Evaluation . . . . .	88
3.4.2	Conclusion . . . . .	94
3.5	Other machine learning methods . . . . .	96
3.6	Random Forest method Application on Mrk421 observation . . . . .	96
3.6.1	Mrk 421 observation . . . . .	97
3.6.1.1	Database used for Mrk421 analysis . . . . .	98
3.6.1.2	Image parameters for classification . . . . .	100
3.6.1.3	$\gamma$ -hadron classification methods . . . . .	100
3.6.1.4	$\gamma$ -hadron segregation using the Random Forest method .	101
3.6.2	Variable Importance . . . . .	103
3.6.3	Alpha plot analysis for Mrk 421 using Random Forest . . . . .	103
3.7	Energy spectrum of Mrk 421 . . . . .	106
3.7.1	Result and Discussion . . . . .	109
<b>4</b>	<b>MACE Sensitivity estimate</b> . . . . .	<b>111</b>
4.1	The MACE telescope . . . . .	116
4.2	Generation of Monte Carlo simulation database . . . . .	118
4.2.1	Height dependent properties of Cherenkov radiation . . . . .	125
4.3	Integral Sensitivity . . . . .	127
4.4	Results and Discussion . . . . .	132
4.4.1	MACE telescope sensitivity in the high energy range . . . . .	134
4.4.2	Fermi 2FHL sources observable from MACE . . . . .	136
4.5	Appendix . . . . .	138
4.5.1	Effective Area after analysis for protons . . . . .	138
4.5.2	Length/width vs energy distribution . . . . .	139
4.5.3	2FHL Sources visible to MACE telescope . . . . .	140

4.5.4	MACE present status . . . . .	141
<b>5</b>	<b>Conclusion and Future outlook</b>	<b>143</b>
5.1	Future outlook . . . . .	146
5.1.1	Planned activities . . . . .	146
5.1.2	Outlook . . . . .	147
	<b>References</b>	<b>147</b>

# Synopsis



# Synopsis

Among the various fields of astronomy (Radio, Infrared, Optical, Ultraviolet, X-ray,  $\gamma$ -ray), ground based  $\gamma$ -ray astronomy is the youngest entrant. This field was pioneered by the Whipple group who made the first detection of TeV  $\gamma$ -rays from the Crab Nebula in the year 1989 [1]. Subsequently, over the next decade,  $\gamma$ -rays were detected from various astrophysical sources [2, 3, 4, 5, 6, 7, 8]. This field has seen remarkable progress in recent years with the source count increasing from just a single source in 1989 to 175 confirmed TeV  $\gamma$ -ray sources [9] as of now. The detection of cosmic  $\gamma$ -rays is based on the principle of the detection of Cherenkov photons produced by cosmic rays in the atmosphere. When cosmic rays enter the Earth's atmosphere, they interact with atmospheric nuclei by hadronic and electromagnetic interactions. Electrons and the cosmic  $\gamma$ -rays interact electromagnetically, i.e. they generate secondary particles by pair production and the bremsstrahlung process. The hadronic cosmic rays, namely protons and ionized nuclei, interact via the hadronic interaction and also give rise to a number of secondary particles. Such generation of secondary particles in the atmosphere is called an Extensive Air Shower (EAS). The hadronic showers create  $\pi^0$  particles that decay into  $\gamma$ -rays making it difficult to distinguish these hadronic showers from genuine showers initiated by  $\gamma$ -rays. The secondary particles generated in EAS move with relativistic speed and generate Cherenkov radiation in the atmosphere. The technique to detect the image generated by the Cherenkov photons produced in EAS is known as the Imaging Atmospheric Cherenkov Technique (IACT). The present generation of IACT based telescopes includes MAGIC [10], H.E.S.S.-I [11] and VERITAS [12]. MAGIC telescope consists of 2 x 17 m

diameter telescopes on the Canary island of La Palma. The VERITAS telescope is an array of 4 x 12 m diameter telescopes in southern Arizona, USA. H.E.S.S.-I consists of an array of 4 x 12 m diameter telescopes in Namibia. H.E.S.S.-II is a 28 m diameter telescope [13] installed in the centre of the H.E.S.S.-I array. All these telescopes except H.E.S.S.-II have energy threshold  $\sim 100$  GeV. In order to augment the capability of IACT based telescopes in the few GeV to few TeV energy range, an international consortium of worldwide researchers are setting up an open observatory known as the Cherenkov Telescope Array (CTA) [14]. CTA will consist of two large arrays of IACTs, one in the Northern Hemisphere with an emphasis to study extragalactic objects and a second array in the Southern Hemisphere to observe galactic sources. The Southern array which is being set up first will deploy IACT based telescopes of various diameters to cater to the wide energy range of few tens of GeV to  $> 100$  TeV. A compact array of 4 x 23 m diameter telescopes will cater to the lower end of the energy range.

In the same endeavour, Astrophysical Sciences Division, BARC<sup>†</sup>, India has also proposed an IACT based telescope known as the **MACE** (**M**ajor **A**tmospheric **C**herenkov **E**xperiment). MACE is a 21m diameter and 25 m focal length telescope presently being installed at Hanle in Ladakh, India (**32<sup>0</sup> 46' 46" N, 78<sup>0</sup> 58' 35" E**) at an altitude of 4270 m a.s.l. It will deploy a photomultiplier tube (PMT) based imaging camera consisting of 1088 pixels with a uniform pixel resolution of  $0.125^\circ$  and a field of view of  $\sim 3.4^\circ \times 4^\circ$ . Out of the 1088 pixels, the innermost 576 pixels ( $24 \times 24$ ) will be used for trigger generation. The trigger field of view is  $\sim 2.6^\circ \times 3^\circ$ . The light collector

---

<sup>0†</sup> Bhabha Atomic Research Centre

of the telescope will be made of 356 mirror panels of 984 mm  $\times$  984 mm size fixed at a square pitch of 1008 mm on a paraboloid shaped basket. Each panel will consist of four 488 mm  $\times$  488 mm facets of spherical mirrors made of aluminum with a quartz coating. The total light collector area will be  $\sim 337\text{m}^2$ . The mirror facets have a graded focal length which ensures that the on-axis spot size is minimum at the focal plane.

The conventional method for  $\gamma$ -hadron segregation, introduced by Hillas works efficiently in the high energy range ( $> 500$  GeV), however, its efficiency reduces drastically below this energy. Therefore, the ground based gamma ray astronomy community has started exploring various options including multivariate methods for data analysis. These methods fall under the umbrella of machine learning methods and employ statistical tools to decipher hidden relationships, if any, among a few or a collection of attributes/parameters with comparatively little computing infrastructure. Machine learning methods have been explored in the field of ground based gamma ray astronomy for quite some time with the earliest efforts being initiated by Bock [15]. Later on, for  $\gamma$ -hadron segregation, the effectiveness of tree based multivariate classifiers was demonstrated by two ground based observatories MAGIC [16] and HESS [17, 18, 19].

Since MACE telescope is expected to have an energy threshold below 100 GeV, we also employed a machine learning method named *Random Forest* (RF) to carry out the  $\gamma$ -hadron segregation. The algorithm for RF was developed by Leo Breiman and Adele Cutler<sup>\*</sup> and can be used for classification and regression problems. RF is an ensemble of simple tree predictors where each tree makes a prediction and the final

---

<sup>0\*</sup>\* <http://www.stat.berkeley.edu/breiman/RandomForests/>

prediction is made by aggregating over the ensemble. The classification tree forms the basic building block of this method. The principle of RF method is based on combining many binary decision trees constructed using several bootstrap samples taken from the training sample and from each node randomly choosing a subset of input variables. The RF method combines the concept of *bagging* [20] and *Random Split Selection* [21]. The classification tree is constructed by binary recursive partitioning of the data set. Each partitioning splits the data sets into different branches. In the present work, the basic aim of the application of RF is to segregate Cherenkov photons generated by the cosmic  $\gamma$ -rays from the background consisting of the Cherenkov photons generated by other cosmic ray particles like protons, electrons and alpha. For this purpose, the present problem is treated as a binary classification problem where one of the classes ‘ $\gamma$ ’ is to be segregated from the other class consisting of protons, electrons and alpha particles. Each entry of training sample consisting of two classes is known as an *event* and is characterized by a vector containing various image (Hillas) parameters. Since each tree in RF method is constructed by introducing a randomness, the collection of such randomly generated trees is known as the RF.

The research presented in the thesis involves determination of the sensitivity estimate for the MACE telescope by employing the *RF* method using a Monte Carlo simulation database. **Since the MACE telescope is expected to be operational by 2017, it was decided to first apply the RF method on the already operational IACT based telescope TACTIC observational data to validate it and then subsequently apply this method for carrying out the  $\gamma$ -hadron segregation for**

**the MACE telescope and then estimate its sensitivity.**

This thesis is divided into two parts. The first part deals with the application of various machine learning methods for  $\gamma$ -hadron segregation for TACTIC telescope. Various machine learning methods such as the Random Forest, Artificial Neural Network, Linear Discriminant, Naive Bayes Classifiers, Support Vector Machines as well as the conventional Dynamic Supercut method were evaluated and compared by simulating triggering events with the Monte Carlo method. It was demonstrated that the RF method is the most sensitive machine learning method for  $\gamma$ -hadron segregation. Thereafter, the Random Forest method was validated by re-analysing the Markarian 421 (Mrk 421) data collected by the TACTIC  $\gamma$ -ray telescope. Markarian 421 in a high state was observed by TACTIC during December 07, 2005 - April 30, 2006 for 202 h. Previous analysis of this data led to a detection of flaring activity from the source at energy  $> 1$  TeV. Within this data set, a spell of 97 h revealed strong detection of a  $\gamma$ -ray signal with daily flux of  $> 1$  Crab unit on several days. Application of this method led to an improvement in the signal detection strength by  $\sim 26\%$  along with a  $\sim 18\%$  increase in detected  $\gamma$  rays compared to the conventional Dynamic Supercuts method. The resultant differential spectrum obtained was represented by a power law with an exponential cut off  $\Gamma = -2.51 \pm 0.10$  and  $E_0 = 4.71 \pm 2.20$  TeV. Such a spectrum was consistent with previously reported results and justifies the use of RF method for analyzing data from atmospheric Cherenkov telescopes. The second part of this thesis deals with the estimation of sensitivity of the MACE telescope by using the RF method. In this study, we discuss the sensitivity estimate of the MACE telescope by using a substantially large

Monte Carlo simulation database at  $5^0$  zenith angle. Due to its very high altitude and large light collector area, the MACE telescope is able to achieve a low energy threshold which is estimated to be  $\sim 38$  GeV at  $5^0$  zenith angle. It will also be able to detect a minimum of  $\sim 2.7\%$  Crab flux in 50 hrs of observation.

### **The contents of the thesis are organized as follows**

- **Chapter 1:** We introduce the field of VHE  $\gamma$ -ray astronomy. Various  $\gamma$ -ray production mechanism will be discussed briefly.
- **Chapter 2:** We will discuss extensive air showers and Imaging Air Cherenkov Technique. This chapter will also discuss the estimation of Hillas parameters. We will also discuss the details of TACTIC telescope briefly.
- **Chapter 3:** We will discuss various machine learning methods such as RF method, Artificial Neural Network, Linear Discriminant method, Naive Bayes Classifiers and Support Vector Machines and compare them with the conventional method. The superiority of RF method will be brought out by using the Monte Carlo simulation database for the TACTIC telescope. This chapter will also discuss the validation of RF method by using the observational data on Mrk 421 collected with the TACTIC telescope.
- **Chapter 4:** We will introduce the MACE telescope in this chapter and will discuss the estimation of its sensitivity by using a huge Monte Carlo simulation database from 10 GeV – 20 TeV energies at  $5^0$  zenith angle.
- **Chapter 5:** Finally in Chapter 5, we present the main conclusions of the thesis along with the future plans.

# ReferencesSynop

- [1] T. C. WEEKES, M. F. CAWLEY, D. J. FEGAN, ET AL. “Observation of TeV gamma rays from the Crab nebula using the atmospheric Cerenkov imaging technique”. *ApJ*, **342**, 379–395 (1989).
- [2] M. PUNCH, C. W. AKERLOF, M. F. CAWLEY, ET AL. “Detection of TeV photons from the active galaxy Markarian 421”. *Nature*, **358**, 477 (1992).
- [3] J. QUINN, C. W. AKERLOF, S. BILLER, ET AL. “Detection of Gamma Rays with E greater than 300 GeV from Markarian 501”. *ApJL*, **456**, L83 (1996).
- [4] M. CATANESE, C. W. AKERLOF, H. M. BADRAN, ET AL. “Discovery of Gamma-Ray Emission above 350 GeV from the BL Lacertae Object 1ES 2344+514”. *ApJ*, **501**, 616–623 (1998).
- [5] F. AHARONIAN, A. AKHPERJANIAN, J. BARRIO, ET AL. “Evidence for TeV gamma ray emission from Cassiopeia A”. *A&A*, **370**, 112–120 (2001).
- [6] P. M. CHADWICK, K. LYONS, T. J. L. McCOMB, ET AL. “PKS 2155-304 - a source of VHE  $\gamma$ -rays”. *Astroparticle Physics*, **11**, 145–148 (1999).
- [7] Y. I. NESHPOR, A. A. STEPANYAN, O. P. KALEKIN, ET AL. “Blazar 3C 66A: Another extragalactic source of ultra-high-energy gamma-ray photons”. *Astronomy Letters*, **24**, 134–138 (1998).
- [8] Y. I. NESHPOR, N. N. CHALENKO, A. A. STEPANIAN, ET AL. “BL Lac: A New Ultrahigh-Energy Gamma-Ray Source”. *Astronomy Reports*, **45**, 249–254 (2001).

- [9] <http://tevcat.uchicago.edu/>.
- [10] J. ALEKSIĆ, S. ANSOLDI, L. A. ANTONELLI, ET AL. “The major upgrade of the MAGIC telescopes, Part II: A performance study using observations of the Crab Nebula”. *Astroparticle Physics*, **72**, 76–94 (2016).
- [11] G. GIAVITTO, T. ASHTON, A. BALZER, ET AL. “A major electronics upgrade for the H.E.S.S. Cherenkov telescopes 1-4”. *ArXiv e-prints* (2015).
- [12] J. HOLDER, R. W. ATKINS, H. M. BADRAN, ET AL. “The first VERITAS telescope”. *Astroparticle Physics*, **25**, 391–401 (2006).
- [13] Y. BECHERINI, M. PUNCH, AND H. E. S. S. COLLABORATION. “Performance of HESS-II in multi-telescope mode with a multi-variate analysis”. In F. A. AHARONIAN, W. HOFMANN, AND F. M. RIEGER, eds., “American Institute of Physics Conference Series”, vol. 1505 of *American Institute of Physics Conference Series*, pp. 741–744 (2012).
- [14] M. ACTIS, G. AGNETTA, F. AHARONIAN, ET AL. “Design concepts for the Cherenkov Telescope Array CTA: an advanced facility for ground-based high-energy gamma-ray astronomy”. *Experimental Astronomy*, **32**, 193–316 (2011).
- [15] R. K. BOCK, A. CHILINGARIAN, M. GAUG, ET AL. “Methods for multidimensional event classification: a case study using images from a Cherenkov gamma-ray telescope”. *Nuclear Instruments and Methods in Physics Research A*, **516**, 511–528 (2004).
- [16] J. ALBERT AND AND CO-AUTHORS. “Implementation of the Random Forest method for the Imaging Atmospheric Cherenkov Telescope MAGIC”. *Nuclear Instruments and Methods in Physics Research A*, **588**, 424 (2008).
- [17] S. OHM, C. VAN ELDIK, AND K. EGBERTS. “ $\gamma$ /hadron separation in very-high-energy  $\gamma$ -ray astronomy using a multivariate analysis method”. *Astroparticle Physics*, **31**, 383–391 (2009).

- [18] A. FIASSON, F. DUBOIS, G. LAMANNA, J. MASBOU, AND S. ROSIER-LEES. “Optimization of multivariate analysis for IACT stereoscopic systems”. *Astroparticle Physics*, **34**, 25–32 (2010).
- [19] F. DUBOIS, G. LAMANNA, AND A. JACHOLKOWSKA. “A multivariate analysis approach for the imaging atmospheric Cherenkov telescopes system H.E.S.S.” *Astroparticle Physics*, **32**, 73–88 (2009).
- [20] L. BREIMAN. “Technical Note: Some Properties of Splitting Criteria”. *Machine Learning*, **24**(1), 41–47 (1996).
- [21] T. DIETTERICH. “Technical Note: Some Properties of Splitting Criteria”. *Machine Learning*, **24**(1), 1–22 (1998).



# List of Figures

1.1	Summary of Chapter 1 . . . . .	2
1.2	Cosmic ray spectra from various experiments . . . . .	8
1.3	Cosmic ray EBL spectra . . . . .	19
1.4	$\gamma\text{-}\gamma$ pair production reaction. . . . .	20
1.5	The CGRH estimated from a sample of 15 blazars . . . . .	22
2.1	Summary of Chapter 2 . . . . .	24
2.2	TeV $\gamma$ -ray sources as shown in TeV catalogue. . . . .	26
2.3	Geometrical interpretation of Cherenkov radiation. . . . .	30
2.4	Spectra of Cherenkov light emitted by vertical $\gamma$ -ray showers . . . . .	32
2.5	The distribution of Cherenkov emission angle with height. . . . .	34
2.6	Cherenkov emission from a single particle moving downwards . . . . .	35
2.7	Cherenkov pulse duration [71]. . . . .	36
2.8	Electromagnetic and hadronic Extensive Air Showers . . . . .	38
2.9	Heitler model for EM shower development . . . . .	39
2.10	Monte Carlo simulation of low/high energy $\gamma$ -protons . . . . .	42
2.11	Imaging Atmospheric Cherenkov Technique . . . . .	43
2.12	1 TeV $\gamma$ , 2 TeV proton image on camera . . . . .	47
2.13	cartoon of few image parameters . . . . .	48
2.14	TACTIC telescope . . . . .	54
2.15	Comparison of light curves from TACTIC, CAT, TA . . . . .	56
3.1	Summary of Chapter 3 . . . . .	60
3.2	Hillas parameters distribution for Gamma, Proton for TACTIC telescope	66
3.3	Schematic of a typical artificial neural network . . . . .	69

3.4	Classification problem . . . . .	72
3.5	Statement of linear SVM. . . . .	74
3.6	A maximal margin hyperplane with its support vectors in linear SVM. . . . .	74
3.7	projection of data into higher dimensional space . . . . .	77
3.8	Bootstrap sampling . . . . .	80
3.9	Random Forest algorithm . . . . .	81
3.10	Classification tree . . . . .	83
3.11	The Error ( $\sqrt{\sigma^2}$ =rms) of estimated hadronness . . . . .	84
3.12	Signal vs background acceptance . . . . .	90
3.13	Gamma acceptance as a function of projected hadron rejection . . . . .	91
3.14	Precision Recall curves . . . . .	94
3.15	The decision-plot of various machine learning methods . . . . .	97
3.16	Various Hillas parameters for simulated and observed background events	99
3.17	Random Forest cut value optimization . . . . .	102
3.18	The variable importance estimated by the Random Forest method . . . . .	104
3.19	On source $\alpha$ plot for Mrk 421 . . . . .	106
3.20	spectrum from Crab nebula and Mrk 421 using TACTIC . . . . .	108
4.1	Summary of Chapter 4 . . . . .	112
4.2	MACE 21m diameter dish in Hyderabad. . . . .	113
4.3	The MACE camera layout . . . . .	118
4.4	Hillas parameters distribution for Gamma, proton and alpha particles . . . . .	122
4.5	Hillas parameters distribution for Gamma and electrons . . . . .	123
4.6	The Pearson parametric correlation coefficient . . . . .	124
4.7	Height dependent Cherenkov emission spectrum . . . . .	125
4.8	Cherenkov Photon density distribution for 100GeV $\gamma$ ,300GeV proton . . . . .	126
4.9	Development of 100 GeV $\gamma$ and 300 GeV proton showers. . . . .	127
4.10	Integrated longitudinal distribution of Cherenkov photons . . . . .	128
4.11	Effective area (Trigger/Analysis) . . . . .	130
4.12	Integral sensitivity of the MACE telescope at $5^\circ$ zenith angle . . . . .	132
4.13	Trigger/Analysis effective area for MACE/MAGIC-I . . . . .	134
4.14	2FHL sources detectable by MACE . . . . .	137

4.15	Trigger/Analysis effective area for protons . . . . .	138
4.16	Length and width distribution of $\gamma$ and proton with Energy . . . . .	139
4.17	Installation progress for MACE . . . . .	141
5.1	Summary of Chapter 5 . . . . .	144



# List of Tables

1.1	gamma ray energy ranges	3
1.2	gamma ray energy ranges	21
2.1	Properties of selected air-Cherenkov instruments	29
3.1	Confusion matrix	88
3.2	Misclassification rate and signal strength	92
3.3	Dynamic Supercuts selection criteria [89]	101
3.4	Detailed Spell wise analysis report of Mrk 421 data due to RF (DSC)	105
4.1	Monte Carlo simulation database	120
4.2	Sources selected from second Fermi high energy catalogue	140

1

# VHE $\gamma$ ray Astronomy

## 1. VHE $\gamma$ RAY ASTRONOMY

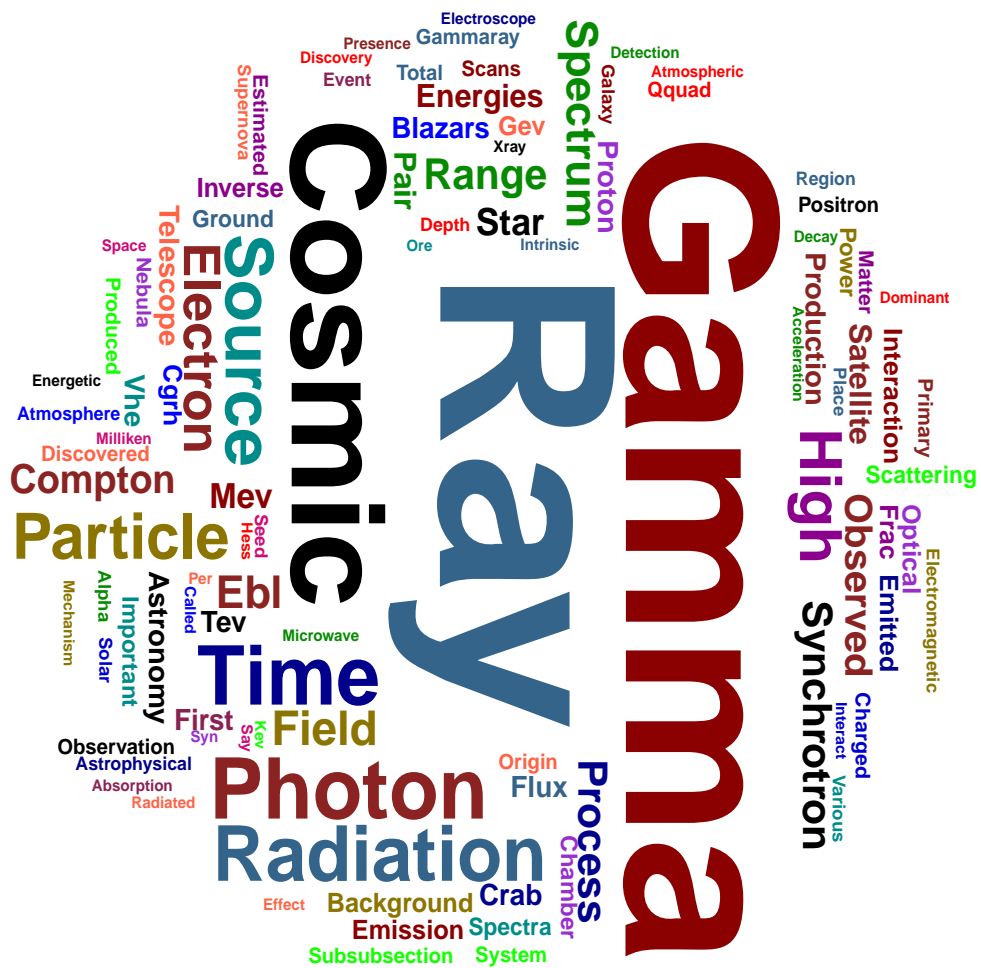


Figure 1.1: Summary of Chapter 1. The size of word represents the number frequency.

## 1.1 Introduction

Among the various fields of astronomy (Radio, Infrared, Optical, Ultraviolet, X-rays, gravitational wave astronomy,  $\gamma$ -rays) ground based very high energy (VHE)  $\gamma$ -ray astronomy is one of the the youngest entrants. This field was pioneered by the Whipple group who made the first detection of TeV  $\gamma$ -rays from the Crab Nebula in the year 1989 [1]. Since then this field has seen remarkable progress.

Energy Range (eV)	Energy Range	Classification	Platform
$5.5 \times 10^5 - 1 \times 10^7$	0.51 - 10 MeV	low/nuclear	satellite
$1.0 \times 10^7 - 3 \times 10^7$	1 - 30 MeV	medium	satellite
$3.0 \times 10^7 - 1 \times 10^{10}$	30 MeV - 10 GeV	high	satellite
$1.0 \times 10^{10} - 1 \times 10^{14}$	10 GeV - 100 TeV	very high	ground
$1.0 \times 10^{14} - 1 \times 10^{17}$	100 TeV - 100 PeV	ultra high	ground
$1.0 \times 10^{17} - 1 \times 10^{20}$	100 PeV - 100 EeV	extremely high	ground

Table 1.1: gamma ray energy ranges

With the advent of more and more sensitive telescopes based on atmospheric Cherenkov technique, an unprecedented number of VHE sources has populated the gamma ray sky. The source count in this field has increased from just a single source in 1989 to 175 confirmed TeV  $\gamma$ -ray sources. The scientific motivation for VHE gamma ray astronomy is multi-faceted. The origin of cosmic rays since its discovery is one of the long standing

## 1. VHE $\gamma$ RAY ASTRONOMY

---

questions. The cosmic rays span the highest energy end of electromagnetic spectrum covering energies from  $10^6$  eV –  $10^{20}$  eV. Broadly speaking, the entire energy range can be subdivided into various sub energy ranges, as given in Table 1.1.

### 1.2 Cosmic rays

In early 1900s, Henri Becquerel discovered that certain elements are unstable and transmute to other elements by emitting particles. These *particles* were named as *radiation* and the process was referred to as *radioactive decay*. It was observed that an instrument named *electroscope* would spontaneously discharge in the presence of radioactive materials. However, when the electroscope was taken to higher altitude, it was noticed that the electroscopes were still discharging although the radioactive matter was absent. It was inferred that this discharge was taking place in presence of some unknown background radiation. In order to investigate the origin of this background, the measurement of radiation level at different heights was carried out with electroscope in a balloon by Austrian physicist **Victor. F. Hess**. Hess went as high as 5 kms in his balloon. It was quite interesting to observe that the radiation levels were increasing with increasing height. It was inferred that the radiation is entering the atmosphere from outer space and this radiation was named as *cosmic Radiation*. This radiation is now known as the *Cosmic Rays*. He wrote [2] ...

- *The results of the present observations are most easily explained by assuming that this radiation enters the atmosphere from above; It was also found that this radiation produced ionization even in closed vessels. It was also observed that this phenomenon was taking place at the same rate even during the nights and solar*

## **1.2. Cosmic rays**

---

*eclipse. So, sun as the source of this radiation was also ruled out ...*

This radiation, very soon was experimentally observed by the Wilson cloud chamber. For the discovery of the cosmic rays, Victor Hess was awarded Nobel prize in 1936 [3].

A nice description of early history of Cosmic Ray Studies is given in [4]. Soon after the discovery of cosmic rays, a flurry of activity took place in the field of cosmic rays. The discovery of tracks in a cloud chamber was successfully carried out by Skobelzyn (1929) [5,6] in the Soviet Union. By using the electroscopes and ion chambers, Milliken and his students [7] had resolved important question that their origin was extra terrestrial. Milliken coined the term *cosmic rays*. Anderson was the graduate student of Milliken who asked him to build a cloud chamber to study the cosmic radiation. This chamber started operation in 1932 and tracks of positive and negative particles were observed. Although Milliken insisted that positive particles must be proton, Anderson by placing a 0.6-cm lead plate across the middle of the chamber observed that a particle moving upward and losing energy as it passed through the plate; its momentum before entering the plate was  $63 \frac{MeV}{c}$  and  $23 \frac{MeV}{c}$  on exiting. It had to be a positive particle and positron was discovered [8,9]. Another discovery of an elementary subatomic particle called the *muon* in cosmic ray was announced by Seth Neddermeyer and Carl Anderson. The positron and the muon were the first of series of subatomic particles discovered using cosmic rays. In 1938, Auger discovered "extensive air showers" [10] by noticing that two detectors located many meters apart, at Alps, both signaled the arrival of particles at exactly the same time. Based on his measurements, Auger concluded that he observed showers with energies of  $10^{15}$  eV. Kenneth Greisen, Vadem Kuzmin and Georgi Zatsepin

## **1. VHE $\gamma$ RAY ASTRONOMY**

---

in 1966 pointed out [11] that high energy cosmic rays would interact with the cosmic microwave background and the maximum energy of cosmic ray particles could not have energies greater than  $5 \times 10^{19}$  eV. The Fly's Eye cosmic ray research group [12] in 1991 observed a cosmic ray event with an energy of  $3 \times 10^{20}$  eV. The AGASA group, Japan [13] in 1994 reported an event with an energy of  $2 \times 10^{20}$  eV. The latest available result is presented in [14]. The measured flux of ultrahigh energy cosmic rays is in the energy range  $10^{17.2}$  to  $10^{20.5}$  eV. They also observed two breaks in the energy spectrum. The observed break was consistent with the GZK cutoff and the ankle. The measured energy of the GZK cutoff was  $\sim 5.6 \times 10^{19}$  eV.

### **1.3 Spectrum**

Cosmic rays can be divided into two types: Primary cosmic rays and secondary cosmic rays. Primary cosmic rays are stable charged particles accelerated to enormous energies by astrophysical sources. They predominantly consist of protons or hydrogen nucleus. The charged component of primary cosmic rays is [15] as follows:

**Protons**             $\sim 86\%$

**$\alpha$  particles**         $\sim 11\%$

**Electrons**             $\sim 1\%$

**Heavy nuclei**         $\sim 2\%$

Apart from it, there is a very small proportion of positrons and anti protons. The neutral component of primary cosmic rays are  $\gamma$ -rays (0.01%), neutrinos and antineutrinos [16]. The secondary cosmic rays are particles produced by the interactions of primary cosmic rays with the interstellar gas or atmospheric nuclei. Broadly, cosmic rays can be divided

### 1.3. Spectrum

---

into four categories:

- Galactic cosmic rays – coming from outside the solar system.
- Extragalactic cosmic rays – coming from outside our galaxy.
- Solar Energetic Particles – associated with solar flares and other energetic solar events.
- Anomalous Cosmic Rays – coming from the interstellar space at the edge of the heliopause.

The cosmic ray spectra observed by various experiments is shown in Figure 1.2. It is clear from the figure that the cosmic ray flux decreases from  $\sim 1$  particle  $m^{-2} s^{-1}$  at energies around 100 GeV to below 1 particle  $m^{-2} \text{ year}^{-1}$  for the energy  $10^{16}$  eV. The spectrum of primary cosmic rays shows a typical power law distribution with spectral index of -2.7 from a few GeV to  $3 \times 10^{15}$  eV. This region of spectrum is known as the "Knee".

$$\frac{dN}{dE} \sim E^{-2.7} \quad (1.1)$$

Beyond  $3 \times 10^{15}$  eV, the spectrum steepens with a spectral index of -3 and for energies more than  $3 \times 10^{18}$  eV – the ankle, a flattening is observed. An upper limit on the energy of cosmic ray sources was theoretically estimated by Greisen [17]. This suppression at the highest energy end was independently estimated by Greisen and Kuzmin & Zatsepin [11]. This cut off is known as the GZK cut off. Cosmic ray experiments like HiRes [18] has shown the suppression of CR spectrum by a factor of two in comparison to the power law extrapolation above  $3 \times 10^{19}$  eV.

## 1. VHE $\gamma$ RAY ASTRONOMY

---

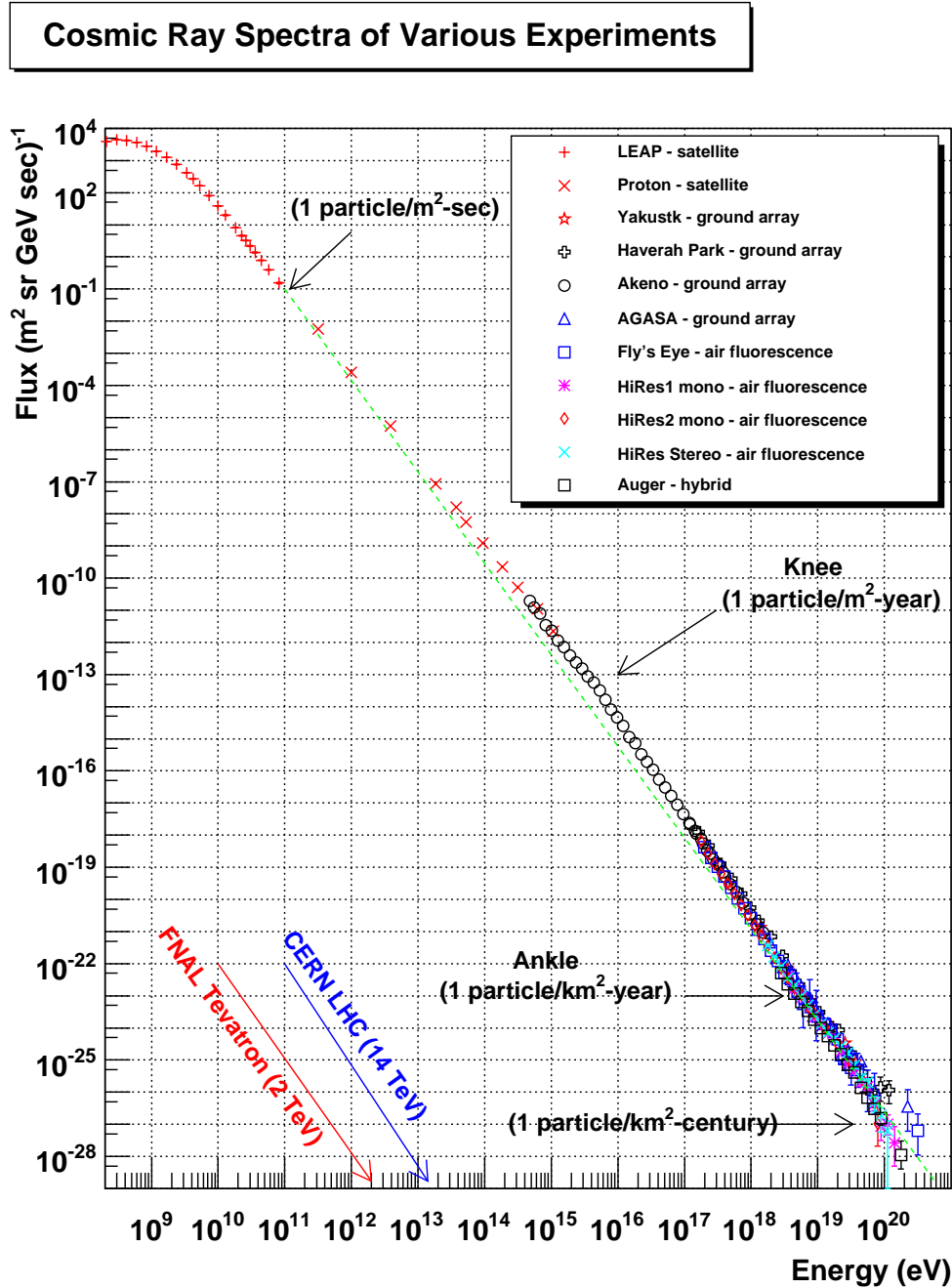


Figure 1.2: Cosmic ray spectra from various experiments (adapted from <http://www.physics.utah.edu/~whanlon/spectrum.html>)

## 1.4 Sources of cosmic rays

The most important plausible sources of cosmic rays are the following:

## **1.4. Sources of cosmic rays**

---

- **Supernova Remnant** : accelerates the particles at the shock front of energies up to the knee region (one acceleration mechanism). It is to be noted that the origin of knee is unknown. During the final stages of the star evolution when the gravitational pressure takes over the thermal pressure generated by the fusion reaction, the star core collapse takes place followed by explosion. The expanding outer shell of the star is known as the supernova remnant (SNR). The total energy radiated by supernova are  $\sim 10^{49}$  ergs [19].
- **Active Galactic Nuclei (AGNs)** : AGNs are the compact region at the centre of a galaxy with their luminosity much higher than the normal galaxy over some or all the bands of the electromagnetic spectrum. AGNs are the most probable astrophysical sources of Ultra high Energy Cosmic Rays (UHECR) accelerating particles up to  $10^{21}$  eV.
- **Gamma Ray Burst (GRBs)** The GRBs are extragalactic and extremely energetic transient emissions of gamma rays. The total energy radiated by GRBs are  $\sim 10^{51-54}$  ergs, i.e. their energy exceeds hundred times the total energy radiated by a supernova.
- **Binary star systems** : One of the companions of such a system is neutron star or black hole. The compact star accretes mass from the companion star. The particle acceleration in these systems are possible either due the internal shocks in the jets formed in the vicinity of the compact object or due to the termination of pulsar wind. The VHE gamma rays are then produced due to

## 1. VHE $\gamma$ RAY ASTRONOMY

---

the presence of optical photons or gas supplied by the companion star.

- **Star-forming galaxies** : These are young galaxies with very high star formation rate compared to regular galaxies and inject very large kinetic power into the interstellar medium via supernova explosions and supersonic stellar winds and generate cosmic rays.

### 1.5 Gamma rays

Unlike the charged components of the cosmic radiation, cosmic  $\gamma$ -ray photons are not influenced by magnetic fields and therefore, are the best entity to point back to their source location to understand the origin of cosmic rays. Therefore, the study of gamma rays allows to understand the physical properties of the sources and the acceleration mechanisms at work.

The first study of Gamma ray astronomy in 100 MeV range was initiated by Morrison [20] where he estimated the flux of cosmic gamma-ray sources. Although the flux of cosmic gamma rays were overestimated, it initiated a series of space based experiments to detect the gamma ray emission from astrophysical sources. In 1961, the *Explorer XI* satellite [21] carried the first gamma-ray telescope into Earth's orbit. This satellite detected 22 cosmic  $\gamma$ -ray events and 22,000 events due to charged cosmic rays but nonetheless the field of Gamma-ray astronomy was born. The next satellite, *Vela* was a set of satellites, launched in pairs in the years 1963 to 1970 detected the first gamma ray burst in 1963. In the year 1975,

---

<sup>0</sup>\* <http://heasarc.gsfc.nasa.gov/docs/heasarc/missions/explorer11.html>

## **1.5. Gamma rays**

---

European Space Agency (ESA) launched *Cos-B* satellite. It was the first satellite dedicated to study the gamma rays. During six years of its operation, it carried out an extensive survey of the Galaxy in the energy range 50 MeV – 5 GeV. *Compton Gamma-ray Observatory* was launched in the year 1991 to study the high energy photons from 20 KeV – 30 GeV energy range. Apart from the detection of gamma rays from Milky way, it discovered point sources of Gamma-rays outside the plane of the galaxy.

Most of what we know of gamma rays has come from satellite based observations, but at energies above tens of GeV, study of gamma rays from ground-based detectors have made considerable progress. Giuseppe Cocconi suggested to measure gamma ray sources at TeV energies at the International Cosmic Ray Conference (ICRC) in Moscow in 1959 [22]. He over estimated the flux of gamma rays from the Crab Nebula. He suggested that the flux could be  $\sim 1000$  times higher than the background. Chudakov and his group built a system of 12 telescopes in Katsiveli, Crimea, near the shore of the Black Sea in 1960. The first method of searching for high energy gamma rays of cosmic origin was published in 1961 by Zatsepin and Chudako [23]. They observed a number of sources as possible gamma ray emitters. They had a total of 47 scans of Crab Nebula, 191 scans of Cygnus A, 20 scans of Cassiopea A, 20 scans of Virgo A, 7 scans of Perseus A and 7 scans of Sagittarius A [24]. There was no significant detection of gamma ray from any of these sources. They gave a upper limit of  $5.5 \times 10^{-11}$  photons per  $\text{cm}^2$  per second in  $\sim 5.5$  h of observation for the threshold of  $\sim 4 - 5$  TeV. However, it is inter-

## **1. VHE $\gamma$ RAY ASTRONOMY**

---

esting to note that now we know that above 4 TeV, the flux from Crab nebula is  $2.5 \times 10^{-12}$  photons per  $\text{cm}^2$  per second, i.e. they over estimated the Crab flux 20 times. But this observation ruled out the estimated flux from the Crab nebula by Cocconi. With the Crimea experiment, the experimental foundation of the field of gamma ray astronomy was laid. In 1967, the construction of a 10 m diameter, F/0.7 telescope on Mount Hopkins at the Whipple observatory [25] at a height of 2300 m above sea level (a.s.l.) was started. The telescope started operation in 1968 with ten PMTs. Trevor Weekes joined this project in 1966. For next 2 decades, Trevor Weekes and his team worked tirelessly. A key milestone came in 1985 when the Cherekov photons distribution was parameterized by Hillas [26]. The major breakthrough in the field of ground based gamma ray astronomy happened in the year 1989 where the very first confirmed detection of gamma way signal from Crab nebula at  $9\sigma$  statistical significance [1] was demonstrated by the Whipple telescope and the field of ground based gamma ray astronomy was formally born.

### **1.5.1 Importance of $\gamma$ -ray astronomy**

Over the last two decades, the field of  $\gamma$ -ray astronomy has acquired a solid scientific foundation. Due to a wealth of invaluable scientific information provided by this branch of astronomy, its contribution was recognized at the 33rd International Cosmic Ray Conference (ICRC) [27] by a modification to the organization of its scientific program. Since 2013, ICRC now devotes a dedicated gamma-ray sessions which is further sub-divided into experimental, instrumentation and theoretical branches [28]. Since the  $\gamma$ -rays are uncharged, they can travel in straight

line and therefore, carries a signature of the original direction of the astrophysical source. This aspect of  $\gamma$ -rays makes them one of the most valuable tools to study not only the location of the source, but also it can help in understanding and therefore unravelling the physical processes operating inside the astrophysical laboratory. One of the most fundamentals questions which can be addressed by the  $\gamma$ -ray astronomy is to determine the origin of cosmic rays. The contribution of galactic cosmic rays to the total cosmic rays, their spectrum and astrophysical properties is the domain of interest. Apart from it, the dynamics of relativistic outflow like jet and winds [29] can very well be studied by this field. Observation of  $\gamma$ -rays can also provide clue about the dark matter annihilation [30].  $\gamma$ -ray astronomy also plays very important role in constraining the intergalactic magnetic and photon radiation fields in the Universe [31]. Fundamental physics questions like violation of the Lorentz invariance can also be studied [32] by using the  $\gamma$ -ray photons. A very nice review [33] about  $\gamma$ -ray astronomy describes the happenings of the field in a coherent way.

### 1.5.2 $\gamma$ -ray production mechanism

The radiation (optical-UV-X-rays) from stars is characterized by blackbody radiation. However, the gamma ray emission is characterized by non thermal radiation. Since the gamma rays are uncharged, apart from studying the non thermal universe, its study has a direct linkage towards understanding the origin of cosmic rays, a profound question since last one century. Gamma rays can be produced by leptonic as well as Hadronic particles. The main production process for gamma rays are:

## 1. VHE $\gamma$ RAY ASTRONOMY

---

### 1.5.2.1 $\pi^0$ decay

High energy protons interact with the matter and decay into a variety of  $\pi$  mesons.

Approximately one third of them are  $\pi^0$  mesons which immediately decay into two  $\gamma$ -rays. The minimum kinetic energy of a proton to produce a  $\pi_0$  meson is given by

$$E_{th} = 2 m_{\pi_0} c^2 \left(1 + \frac{m_{\pi_0}}{m_p}\right) \sim 280 MeV \quad (1.2)$$

The energy of the  $\gamma$ -ray photon emitted by a  $\pi^0$  at rest is peaked at  $E_\gamma = m_{\pi_0} c^2 / 2 = 67.5$  MeV.

### 1.5.2.2 Synchrotron Radiation

Synchrotron Radiation is emitted when a charged particle is accelerated in the presence of magnetic field. The synchrotron power radiated by a relativistic electron is given by [34]

$$P_{syn} = \frac{2}{3} r_e^2 c \gamma^2 \beta^2 B^2 \sin^2 \alpha \quad (1.3)$$

where  $r_e = e^2/m_e c^2$  is the classical electron radius and  $\gamma$  is the Lorentz factor of the electron. For isotropic distribution of mono energetic electrons

$$P_{syn} = \frac{4}{3} \beta^2 \gamma^2 c \sigma_T U_B \quad (1.4)$$

where  $\sigma_T$  is the Thomson cross section and  $U_B = B^2/8\pi$  is the magnetic field energy density. Because of the higher mass of proton than electron ( $m_p \sim 1836 m_e$ ), syn-

chrotron radiation from protons is negligible. Only electrons/positrons contribute to the synchrotron emission. The synchrotron spectrum emitted by an electron of energy  $\gamma m_e c^2$  moving with pitch angle  $\alpha$  can be written as [34]

$$P_{syn}(\gamma, \nu) = \frac{\sqrt{3} e^3 B \sin \alpha}{m_e c^2} F\left(\frac{\nu}{\nu_c}\right) \quad (1.5)$$

where  $\nu$  is the frequency of the emitted photon and

$$\nu_c = \frac{3 e B \gamma^2}{4\pi m_e c} \sin \alpha \quad (1.6)$$

is the critical frequency. The synchrotron power function  $F(x)$  contains a modified Bessel function. The shape of the synchrotron spectrum is estimated by estimating the shape of  $F(x)$ . The peak of synchrotron spectrum is located at  $\approx 0.29(\nu/\nu_c)$ .

### 1.5.2.3 Inverse Compton Scattering

In the Inverse Compton process, a low energy photon, called the seed photon, say generated by the Synchrotron radiation, is upscattered by a relativistic particle, say electron and a considerable fraction of electron energy is transferred to the photon to increase its energy. The energy of Compton boosted photon is given by [35, 36]

$$E_\gamma \simeq 4/3 \langle \epsilon \rangle \gamma^2 \quad for \quad \gamma \epsilon \ll m_e c^2 \quad (1.7)$$

and

## 1. VHE $\gamma$ RAY ASTRONOMY

---

$$E_\gamma \simeq \langle E_e \rangle / 2 \quad \text{for} \quad \gamma \epsilon \gg m_e c^2. \quad (1.8)$$

The seed photons for the Inverse Compton scattering may be produced by Synchrotron radiation, star field, cosmic microwave background etc.

Example <sup>1</sup> [37]: An Isotropic radio photons at  $\nu_0 = 1$  GHz, inverse Compton up-scattered by electrons having Lorentz factor  $\gamma = 10^4$  will have the average frequency

$$\langle \nu \rangle = 10^9 \text{ Hz} \frac{4}{3} (10^4)^2 \approx 1.3 \times 10^{17} \text{ Hz} \quad (1.9)$$

which corresponds to the X-ray radiation. Likewise, if an electron is having an energy of  $\sim 1.7 \times 10^{13}$  eV and it hits an microwave background seed photon with energy  $\sim 7 \times 10^{-4}$  eV, this seed photon will be up scattered to a photon of energy 1 TeV.

In the Thomson regime, the radiative power emitted due to inverse Compton scattering of an isotropic soft photon distribution can be written as [34]

$$P_{com} = \frac{4}{3} \beta^2 \gamma^2 c \sigma_T U_{ph} \quad (1.10)$$

where  $U_{ph}$  is the energy density of the seed photons. We can have a comparison of power emitted due to Synchrotron and Inverse Compton process by comparing the

---

<sup>1</sup><http://www.cv.nrao.edu/course/astr534/InverseCompton.html>

equation (1.4) and (1.10). By this comparison, we get

$$\frac{P_{syn}}{P_{com}} = \frac{U_B}{U_{ph}} \quad (1.11)$$

It is to be noted that Synchrotron and inverse-Compton losses both have the same electron-energy dependence ( $\propto \gamma^2$ ). Therefore, the effects of both Inverse Compton and Synchrotron losses on the spectra are indistinguishable.

#### 1.5.2.4 Bremsstrahlung

When a charged particle, say electron, moves in a electric field, say in the field of atomic nucleus, it gets accelerated by the strong nuclear charge and an electromagnetic radiation [38] is produced. It is called the *Bremsstrahlung* radiation or free-free emission. This radiation plays an important role in the theory of extensive air showers. This radiation is of two types: thermal and relativistic. Thermal Bremsstrahlung occurs when the particles are at uniform temperature. Their characteristic behavior is described by Maxwell-Boltzmann distribution. In astrophysical context, such process is operating in intra cluster medium consisting of cold ionized plasma and accretion disk of [39, 40]. The Relativistic Bremsstrahlung process operates in the dense astrophysical environment such as  $\gamma$ -Cygni supernova remnant [41].

#### 1.5.3 Gamma ray absorption

The absorption of gamma rays can takes place via  $\gamma$ -matter interaction and  $\gamma\gamma$  interaction. In Gamma matter interaction, the  $\gamma$  radiation ionizes the matter via

## 1. VHE $\gamma$ RAY ASTRONOMY

---

three processes: the photoelectric effect, Compton scattering, and pair production. Photoelectric effect and Compton scattering are two main process through which gamma rays interact with the matter. The interacting  $\gamma$ -rays lose either full or a part of its energy in such process. The photoelectric effect is dominant form of energy transfer in X-rays and Gamma ray photons below 50 KeV energy. In this process, gamma ray photon interacts with the medium and the electron transfers its total energy to an atomic electron. This electron is ejected and the kinetic energy of emitted electron is equal to the energy of incident photon minus the binding energy. However, the cross section of this process becomes too small at higher energies. The Compton scattering is the dominant process in the  $\gamma$ -ray energy in the range from few hundred keV to 10 MeV and pair production is dominant process of energy loss from high energy to very high energy range. In pair production, an elementary and its antiparticle (electron-positron, or muon-antimuon, or proton-antiproton) is created in the field of nucleus. If the  $\gamma$ -ray photon is present, it produces a pair of electron and positron. It is one of the most important processes in the field of very high energy gamma ray astronomy. The threshold for pair production is  $> 1.02$  MeV. The pair production process becomes a dominant process above 30 MeV.

### 1.5.4 $\gamma$ - $\gamma$ interaction

The extragalactic background light (EBL)<sup>2</sup> is produced by the first stars formed in the universe. The EBL consists of radiation from the infrared (IR), through the optical, ultraviolet (UV) excluding the cosmic microwave background (CMB).

---

<sup>2</sup>The EBL, defined as the emission in the 0.1 to 1000  $\mu$ m wavelength region.

## 1.5. Gamma rays

---

This radiation is dominated by emission from all the stars. For constraining the

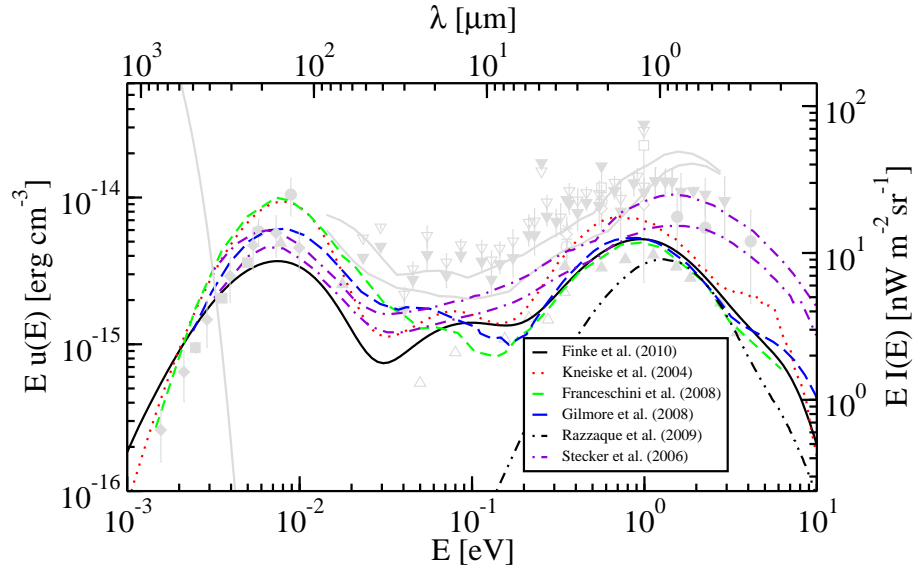


Figure 1.3: Cosmic ray EBL spectra from various experiments. This Figure is adapted from [42]

EBL intensity, modeling is an important tool. Figure 1.3 shows many EBL measurements, constraints and models [42]. The EBL affects the spectrum of VHE sources, predominantly blazars, in the  $\sim$ 10 GeV to 10 TeV energy regime and plays an important role in the propagation of high energy  $\gamma$ -rays, predominantly emitted by blazars. Therefore, the study of high energy blazars allows one to constrain the EBL models. In addition to it, once the EBL determination is available from various observation, this knowledge allows the determination of intrinsic spectrum of VHE  $\gamma$ -ray sources, thereby providing insights into the high energy astrophysical processes like particle acceleration mechanisms operating in these sources.

## 1. VHE $\gamma$ RAY ASTRONOMY

---

### 1.5.4.1 $\gamma$ -ray absorption by pair production

When a VHE  $\gamma$ -rays travels from cosmological distances, it suffers en-route absorption because of its interaction with low energy photons provided by the EBL. If the

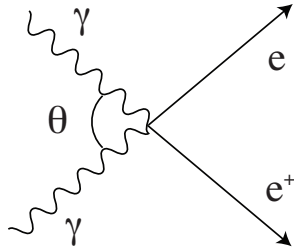


Figure 1.4:  $\gamma$ - $\gamma$  pair production reaction.

energy of  $\gamma$ -ray photon is  $E_\gamma$  and the energy of EBL photon is  $E_{ebl}$ , then the interaction of high energy photon with the EBL photons lead to particle anti-particle pair creation when the total  $\gamma$ -ray energy in the center of momentum frame system exceeds the rest frame energy of the two particles [43]. This means that some of high energy  $\gamma$ -ray photons will not arrive at the telescopes, i.e., the  $\gamma$ -ray photons from the distant sources will be attenuated by the EBL. The threshold for the creation of an  $e^+ + e^-$  pair is given by [44]:

$$\epsilon_{th}(E_\gamma, \theta, z) = \frac{2(m_e c^2)^2}{E_\gamma(1 - \cos \theta)} \quad (1.12)$$

For head on collisions, i.e.  $\theta = 0$ , we get  $\epsilon_{th} E_\gamma = 0.26 \times 10^{12}$ . Here all the energies are in eV. Some important results are shown in Table 1.2. This table is adapted from [35]

Radiation	Energy	$E_\gamma$
2.7 K CMBR	$6.0 \times 10^{-4}$ eV	$\approx 4 \times 10^{14}$ eV
starlight	$\sim 2.0$ eV	$\approx 10^{11}$ eV
X-rays	$\sim 1.0$ KeV	$\approx 3 \times 10^{11}$ eV

Table 1.2: gamma ray energy ranges

### 1.5.5 Cosmic $\gamma$ -ray horizon (CGRH)

Cosmic  $\gamma$ -ray horizon is a measure of opacity of the universe towards  $\gamma$ -ray photons.

It can act as a probe of estimating the distance of astrophysical  $\gamma$ -ray sources. It is to be noted that the density of EBL depends on the redshift, therefore, the probability of such interaction is a function of the redshift of the emitting sources.

The distance travelled by the  $\gamma$ -ray photon can be given in terms of the optical depth. It is given by  $e^{-\tau(E,z)}$ . The coefficient  $\tau(E, z)$  is called optical depth. **The cosmic  $\gamma$ -ray horizon (CGRH) is the energy at which the optical depth is equal to unity.**

#### 1.5.5.1 Determination of CGRH

Suppose we know the intrinsic spectrum of high energy  $\gamma$ -ray emitting sources. When this spectra is compared with the observed spectra, the difference in their spectra is caused by the EBL. The blazars emit photons through synchrotron emission and inverse Compton scattering. Using a simultaneous observation of a set of 15 blazars from Fermi LAT satellite, Imaging atmospheric Cherenkov telescopes

## 1. VHE $\gamma$ RAY ASTRONOMY

---

(IACT) (H.E.S.S., MAGIC, VERITAS) and from the data covering the entire electromagnetic spectrum (radio - $\gamma$ -rays) [45], the observed spectrum of blazars were modelled. Their spectrum from infrared to  $\gamma$ -rays was fitted to obtain the intrinsic spectra of blazars upto few tens of GeV, till the energy range when imaging atmospheric Cherenkov telescope covers the higher energies. The  $\gamma$ -ray photons flux in the TeV energy range gets attenuated by the EBL. By comparing the difference in the flux between the intrinsic spectra of blazars with that of obtained from the IACT, the optical depth was estimated. Once the optical depth was available experimentally, one can estimate the CGRH. The estimated CGRH from a sample of 15 blazars is shown by Figure 1.5. This Figure is adapted from [46]. The shaded region represents the uncertainties from the EBL modeling of observed data.

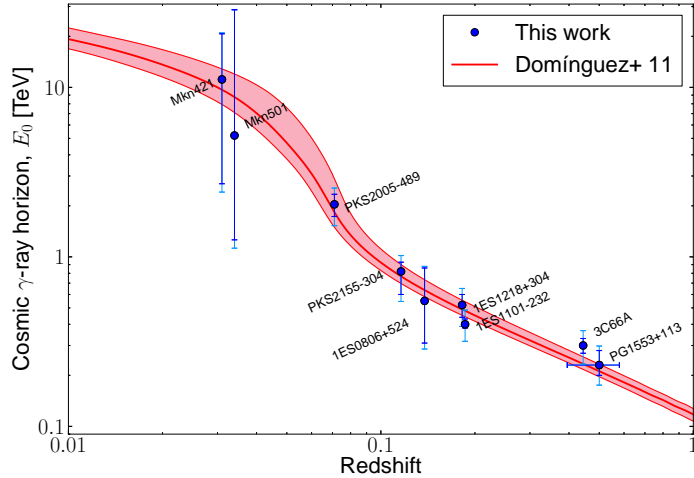


Figure 1.5: The CGRH estimated from a sample of 15 blazars by [46]. Dark blue lines are statistical uncertainties; light blue lines are statistical and 20% systematic uncertainties. The red line is a model.

2

## Ground based $\gamma$ -Ray Astronomy

## 2. GROUND BASED $\gamma$ -RAY ASTRONOMY



Figure 2.1: Summary of Chapter 2. The size of word represents the number frequency.

---

Ground based  $\gamma$ -ray astronomy is a rather new discipline. The first successful detection of the TeV source, Crab Nebula [1] took place in the year 1989. With a small lull in the field, the next detection took place in the year 1992 when the second TeV  $\gamma$ -ray source Markarian 421 [47] was detected and subsequently in 1996, the Mrk501 [48] was detected. Slowly a series of such extragalactic sources [49, 50, 51, 52, 53] were discovered. With the advent of more and more sensitive systems, the catalogue [54] of TeV  $\gamma$ -ray sources saw the addition of newer and newer sources. With just a single source in 1989, this field has now 175 confirmed TeV  $\gamma$ -ray sources (Figure 2.2 [54]).

### 2.0.6 Ground based observatories

The study of universe in  $\gamma$ -rays from ground is challenging because the  $\gamma$ -rays get absorbed in the atmosphere. Before the successful implementation of ground based detection of  $\gamma$ -rays, satellite was the only medium available for investigating the high energy universe. Presently the study of known universe in MeV to  $\sim$  10 GeV range is carried out by satellite-borne instrument Fermi Large Area Telescope (Fermi-LAT) [55] which has a field of view  $\sim$  2 steradian. The Fermi telescope spans a broad  $\gamma$ -ray energy range from tens of MeV to  $\sim$  300 GeV, although it is to be noted that the sensitivity of telescope beyond 10 GeV is quite poor. The biggest constraining factor for the poorer sensitivity of satellite based experiments is its limited effective area. As long as there was no substantial improvement in the effective area, there was very little chance of probing the very high energy universe effectively. This goal was attained by the successful working of ground based telescopes based on detecting atmospheric Cherenkov radiation. The medium of detecting the Cherenkov radiation can either be water or air. The water based Cherenkov

## 2. GROUND BASED $\gamma$ -RAY ASTRONOMY

---

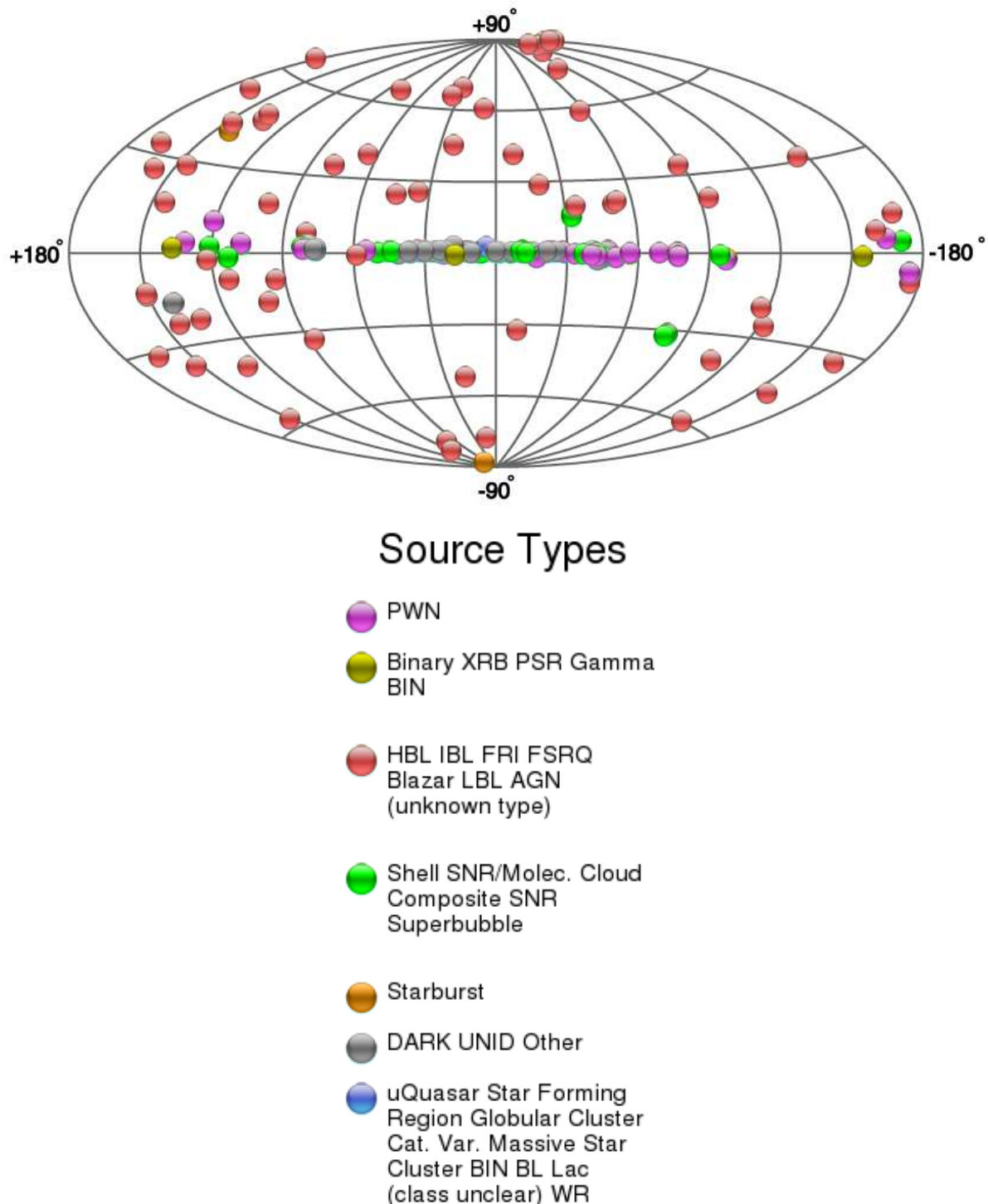


Figure 2.2: TeV  $\gamma$ -ray sources as shown in TeV catalogue.

---

detectors detect the Cherenkov radiation produced in the clear water. Such detectors consist of many water tanks distributed over a large area. The *High Altitude Water Cherenkov Observatory (HAWC)* [56, 57, 58, 59] is a  $\gamma$ -ray observatory located in Mexico at an altitude of 4100 meters at  $18^\circ 59'41''N$   $97^\circ 18'30.6''W$ . It is a continuously operated, TeV gamma-ray observatory with more sensitivity angular resolution and background rejection than the *Milagro*  $\gamma$ -ray observatory [60, 61] in New Mexico. The HAWC observatory consists of an array of 300 water Cherenkov detectors. The prompt emission from gamma ray burst above 50 GeV can also be detected by this instrument. This observatory is in operation and produced some interesting results [62]. HAWC has observed Crab between November 2014 and February 2016 on a daily basis. They obtained a continuous 400-days light curve. In their observation, they did not detect any flaring activity from Crab in the TeV energy range. Their result is in contrast with the results obtained from AGILE satellite which reported [63] the discovery of strong  $\gamma$ -ray flares from the Crab Nebula. The observation from HAWC will be relevant in assessing the variability of from this important source, i.e. Crab. This detector has the capability to observe extragalactic source like Mrk421, Mrk501 on a daily basis. The one year continuous observation from November 2014 to February 2016 of Mrk421 has shown that the source is emitting flux at the steady level whereas in the case of Mrk501 observation, although the source was emitting at a steady level on 6th of April 2016, it detected Mrk 501 with a flux 2.2 times larger than the Crab Nebula flux [64]. HAWC is working as a prime survey instrument for high-energy  $\gamma$ -ray astrophysics. It will help in understanding the high energy universe with unprecedented sensitivity.

## 2. GROUND BASED $\gamma$ -RAY ASTRONOMY

---

When the medium of Cherenkov photon generation is air, various observatories has made significant advances in the field of high energy  $\gamma$ -ray universe. The successful detection of TeV  $\gamma$ -rays in 1989 proved to be a turning point in studying the very high energy universe which was earlier inaccessible to satellite based telescopes. These telescopes work on the principle of detecting very feeble and brief ( $\sim$  ns) Cherenkov light pulse generated by the relativistically moving electron in the atmosphere. Compared to  $\sim 1 \text{ m}^2$  effective area of satellite based telescope, the effective area of ground based telescopes is  $\sim 10^5 \text{ m}^2$ . Although it should be noted that the ratio of  $\gamma$ -rays to hadron events is  $\sim 10^{-3}$ , and hence the  $\gamma$ -hadron segregation is a major issue. However, this issue is well addressed by Imaging Atmospheric Cherenkov Technique (IACT) based telescopes. And by using a stereoscopic system with two or more telescopes, the rejection of hadronic events improves by a factor of 100, angular resolution and energy resolution improves and becomes better than  $\sim 0.1^\circ$  and 15% respectively [31]. In order to get the maximum sensitivity of an stereoscopic array, the telescope spacing should be large enough to provide a sufficient baseline but small enough that multiple telescopes fit within the Cherenkov light pool. The optimum spacing for stereoscopic system has provided unprecedented sensitivity to IACT based telescopes with respect to any satellite based telescope in the  $\gamma$ -ray energy window. A summary IACT based telescope is given in Table 2.1.

A very good review on IACT instruments is available in [31, 65, 66]. Depending on optimum cuts, the telescope systems such as H.E.S.S., VERITAS (Table 2.1) could detect the sources of  $\sim 1\%$  of the strength of the Crab Nebula [66]<sup>1</sup>. Although the IACT based telescope have very good dynamic range in the high energy end, the lowest possible  $\gamma$ -ray

---

<sup>1</sup>( $\nu F_\nu \sim 3 \times 10^{-13} \text{ erg cm}^{-2} \text{ s}^{-1}$  around 1 TeV)

## 2.1. Atmospheric Cherenkov Radiation

---

Instrument	Lat. (°)	Long. (°)	Alt. (m)	Tels.	Area (m <sup>2</sup> )	Pixels	FoV (°)	Thresh. (TeV)	Sens. (% Crab)
H.E.S.S.	-23	16	1800	4	428	960	5	0.1	0.7
VERITAS	32	-111	1275	4	424	499	3.5	0.1	1
MAGIC	29	18	2225	1	234	574	3.5 <sup>†</sup>	0.06	2
CANGAROO	-31	137	160	3	172	427	4	0.4	15
Whipple	32	-111	2300	1	75	379	2.3	0.3	15
HEGRA	29	18	2200	5	43	271	4.3	0.5	5
CAT	42	2	1650	1	17.8	600	4.8 <sup>†</sup>	0.25	15

Table 2.1: Properties of selected air-Cherenkov instruments, including two of historical interest (HEGRA and CAT). <sup>†</sup> These instruments have pixels of two different sizes. This table is Adapted from [65].

detection is in the range of  $\sim 10$  GeV because of the limitation induced by the fluctuations in air-shower development. The present day Cherenkov instruments is still away from this fundamental limit.

In this chapter, we introduce the fundamentals of atmospheric Cherenkov radiation. We will also briefly discuss the TACTIC (TeV Atmospheric Cherenkov Telescope with Imaging Camera) telescope.

## 2.1 Atmospheric Cherenkov Radiation

When a charge particle moves through a medium with speed more than the phase velocity of light, the emitted radiation is known as the *Cherenkov* radiation. This radiation was experimentally discovered by P. A. Cherenkov in 1934 [67]. Frank and Tamm in 1937 [68] gave its theoretical interpretation. All three shared Nobel prize in 1958 [69]. The emission of radiation is due to an asymmetric polarization of the medium in the front and at the rear of the particle. This asymmetry gives rise to a varying electric dipole momentum and hence the radiation is produced. Figure 2.3 shows the geometrical interpretation of atmospheric Cherenkov radiation. The emission is observed only at particular angle only

## 2. GROUND BASED $\gamma$ -RAY ASTRONOMY

---

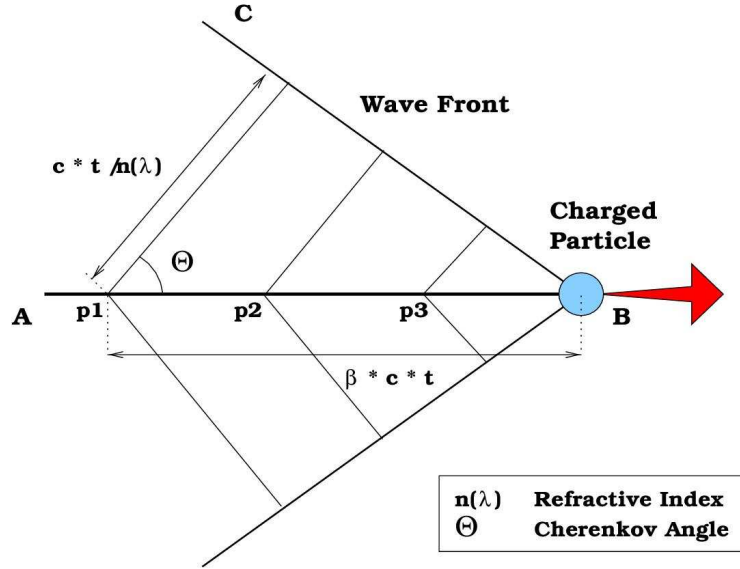


Figure 2.3: Geometrical interpretation of Cherenkov radiation.

with respect to the particle track. The angle is known as the **Cherenkov angle** ( $\theta$ ). A plane wavefront BC is formed when the waves from the arbitrary points P1, P2, P3 over the AB track are coherent. This coherence takes place when the particle and light travel time is same, i.e. time for the particle to travels from A to B = light travelling time from A to C [70].

$$\cos \theta = \frac{\frac{c}{n(\lambda)} \Delta T}{\beta \cdot c \cdot \Delta T} \quad (2.1)$$

where  $\Delta T$  is the time in which the particle moves from A to B,  $n$  is the refractive index of the medium,  $v = \beta c$  is the particle's velocity. The Cherenkov radiation is represented by equation (2.1). The main characteristics of Cherenkov radiation are:

- for a given medium there is a minimum velocity for a particle called **critical velocity**.

$$\beta_{min} = \frac{1}{n} \quad (2.2)$$

## 2.1. Atmospheric Cherenkov Radiation

---

below which no radiation takes place. At  $\beta_{min}$ ,  $\theta = 0^\circ$  i.e. radiation is emitted along the particle track. On the other hand, if particle moves slower than the radiation ( $v < c/n$ ), the equation (2.1) has no solution and hence no radiation takes place.

- The angle of emission is maximum when  $\beta = 1$ , i.e. the particle is ultra relativistic. Therefore,

$$\theta_{max} = \cos^{-1} \left( \frac{1}{n} \right) \quad (2.3)$$

- In the x-ray region,  $n(\omega)$  is always  $< 1$ , so the radiation is forbidden. So emission in the x-ray region is impossible because the refractive index n is less than unity.

In addition to above conditions, two further conditions need to be fulfilled to achieve coherence:

- The length  $l$  of the track of the particle in the medium should be large compared with the wavelength  $\lambda$  of the radiation in question, otherwise diffraction effects will become dominant.
- The velocity of the particle must be constant during its passage through the medium, i.e. the differences in the times for particle to traverse successive distances  $\lambda$  should be small compared with the period  $\frac{\lambda}{c}$  of the emitted light.

### 2.1.1 Cherenkov light distribution

The number of Cherenkov photons per unit of track length of the particle and per unit of wavelength (i.e. the intensity of Cherenkov radiation) is given by the Frank-Tamm formula [68]:

$$\frac{d^2N}{dxd\lambda} = \frac{2\pi\alpha z^2}{\lambda^2} \times \left( 1 - \frac{1}{\beta^2 n^2(\lambda)} \right) \quad (2.4)$$

## 2. GROUND BASED $\gamma$ -RAY ASTRONOMY

---

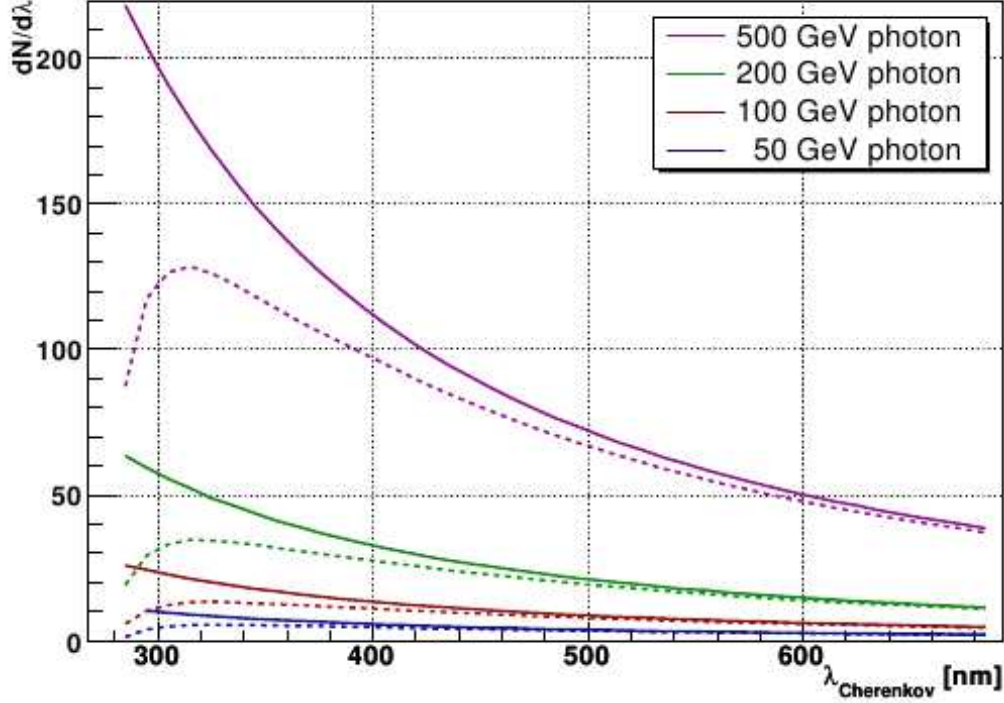


Figure 2.4: Spectra of Cherenkov light emitted by vertical  $\gamma$ -ray showers of different primary energy at 10 km height is represented by solid curves while the corresponding detected spectra (effect of absorption by ozone and scattering) at observational level is represented by dashed curves. This figure has been adopted from [71].

where  $\alpha = e^2/\hbar c = 1/137$  is the structure constant.

Therefore, the number of photons per unit length and radiation wavelength depends on charge and velocity of the particle. Since the intensity is proportional to  $1/\lambda^2$ , **short wavelengths dominate**. Most of the photons in Cherenkov emission are therefore produced in a short wavelength range i.e. in UV and blue.

For electron moving along a track of length  $l$ , the number of emitted Cherenkov photon in the wavelength range  $\lambda_1$  and  $\lambda_2$  is then given by [72]

$$N = 2\pi\alpha l \times \left( \frac{1}{\lambda_2} - \frac{1}{\lambda_1} \right) \times \left( 1 - \frac{1}{\beta^2 n^2(\lambda)} \right) \quad (2.5)$$

## 2.1. Atmospheric Cherenkov Radiation

---

The differential photon spectrum of Cherenkov photons is shown in Figure 2.4 for photons emitted at 10 km and observed at 2 km altitude. There is a clearcut difference in the observed and emitted Cherenkov photon spectrum. The atmospheric absorption is more efficient toward the shorter wavelengths. It happens due to atmospheric absorption of cherenkov photons.

### 2.1.2 Threshold energy for Cherenkov emission

The threshold energy ( $E_{min}$ ) for a particle to emit Cherenkov radiation in the atmosphere is given by

$$E_{min} = \gamma_{min} m_0 c^2 = \frac{m_0 c^2}{\sqrt{1 - \beta_{min}^2}} = \frac{m_0 c^2}{\sqrt{1 - 1/n^2}} \quad (2.6)$$

where  $m_0$  is the rest mass of the particle.

At the sea level, the refractive index of air is  $\sim 1(1.00029)$ , the equation (2.3) shows that the maximum emission angle for the cherenkov radiation is  $\sim 1.3^\circ$ . Therefore, the energy threshold for Cherenkov radiation on ground for electrons, muons, and protons are 21.3 MeV, 4.4 GeV, and 39.1 GeV respectively.

### 2.1.3 Height dependent Cherenkov emission

The energy threshold for Cherenkov radiation production depends on the height of atmosphere because the refractive index of medium is a function of height. The height dependent energy threshold for Cherenkov radiation is given by [72]

$$E_{min} = \frac{m_0 c^2}{\sqrt{2\eta_0 e^{-h/h_0}}} \quad (2.7)$$

## 2. GROUND BASED $\gamma$ -RAY ASTRONOMY

---

where  $\eta_0 = 2.9 \times 10^{-4}$ ,  $h_0 \sim 8$  km is scale height of atmospheric pressure. As the height of the observation location increases, the threshold energy for Cherenkov radiation increases. For electron,  $E_{min}$  is 42 MeV at an altitude of 10 km.

### 2.1.3.1 Maximum angle for Cherenkov emission

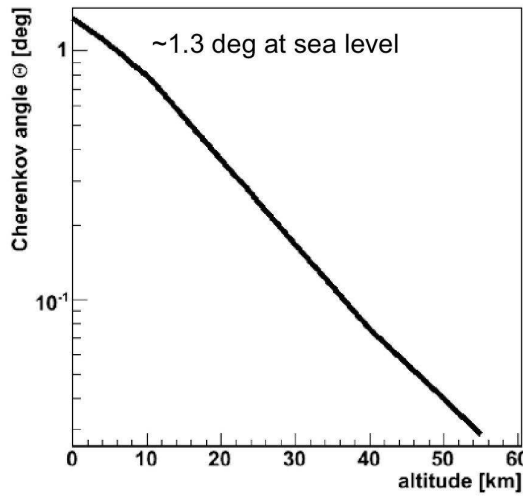


Figure 2.5: The distribution of Cherenkov emission angle with height.

The maximum angle  $\theta_{max}$  for particles with  $\beta \sim 1$  can be obtained from the expression

$$\cos \theta_{max} = \frac{1}{1 + \eta_0 \exp(-h/h_0)} = 1 - \eta_0 \exp(-h/h_0) \quad (2.8)$$

Therefore, the angle of Cherenkov emission decreases with the increase in height. This dependence is shown in Figure 2.5.

### 2.1.3.2 Cherenkov light pool

A cartoon of Cherenkov emission from a single particle moving downwards is shown in Figure 2.6. The Cherenkov emission from a charged particle is characterized a cone with an emission angle of  $\sim 1^\circ$ . As the charged particles move downward in the atmosphere,

## 2.1. Atmospheric Cherenkov Radiation

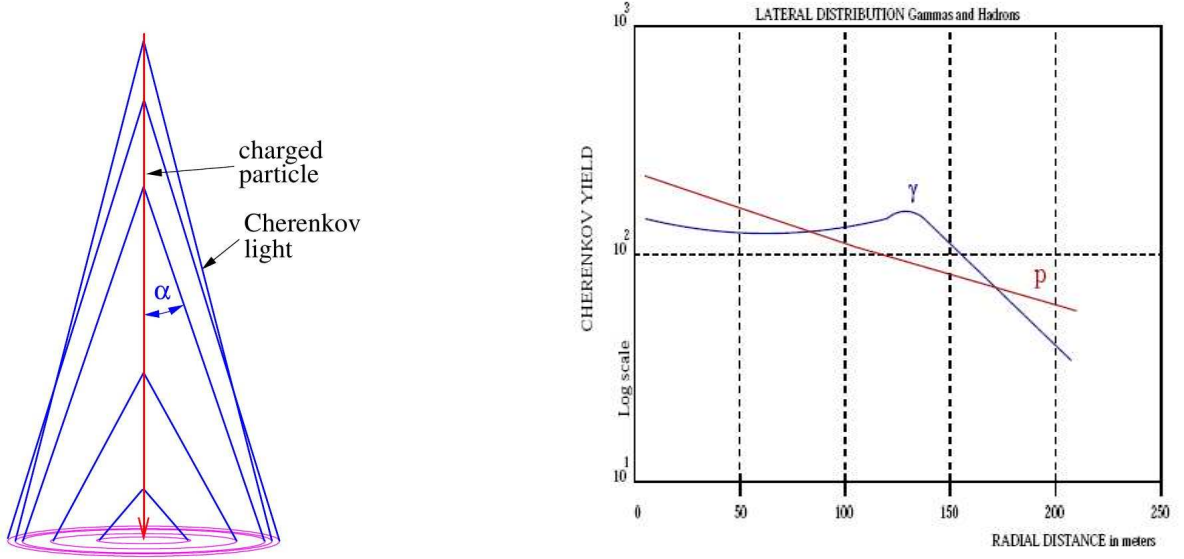


Figure 2.6: The left panel of above figure shows the atmospheric Cherenkov emission from a single particle moving downwards [73]. The right panel shows the Lateral Cherenkov photon distribution for ( $1\text{ TeV}$ )  $\gamma$ -rays photons and ( $2\text{ TeV}$ ) protons shower.

the Cherenkov radiation generates a light pool as it reaches the observation level. The lateral distribution of Cherenkov pool typically has a radius of  $\sim 120 - 125$  meters. The resultant Cherenkov pool on the ground has  $\sim 100$  photons  $m^{-2}$ . Such a lateral distribution for  $1\text{ TeV}$   $\gamma$  and  $2\text{ TeV}$  protons [74] is shown in the right panel of Figure 2.6. The flat distribution of Cherenkov photons takes place on account of focussing of Cherenkov photons because of changing Cherenkov emission angle.

### 2.1.3.3 Cherenkov light pulse duration

In a dispersive medium like atmosphere, the emission angle for Cherenkov radiation is different for different wavelengths and this angle also changes with the change in height. Hence the Cherenkov pulse has a spread. The observed duration along the particle track

## 2. GROUND BASED $\gamma$ -RAY ASTRONOMY

---

at a distance  $r'$  as shown in Figure 2.7 is

$$\Delta t = \frac{r'}{\beta \cdot c} \cdot (\tan \theta'_{max} - \tan \theta_{max}). \quad (2.9)$$

Let us consider the emissions of Cherenkov photons at two points A and B, assuming

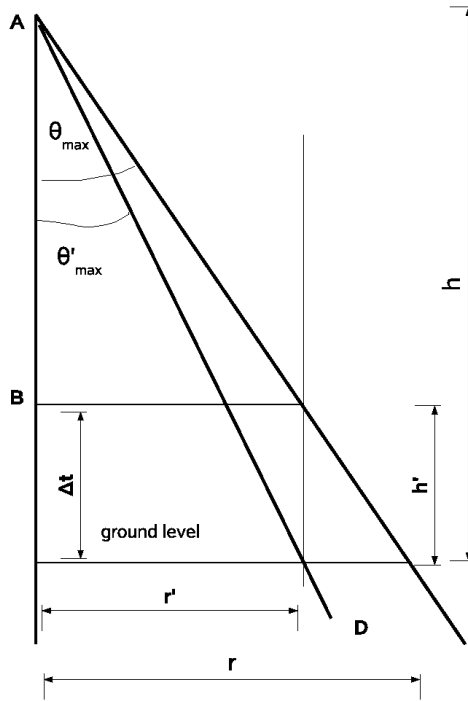


Figure 2.7: Cherenkov pulse duration [71].

that photons are emitted along the track of the particle. The measured time difference between the detection of photons can be written as

$$\delta t = \frac{\eta_0 h_0}{c} (exp^{-h'/h_0} - exp^{-h/h_0}). \quad (2.10)$$

## 2.2. Cherenkov Radiation in Extensive Air Showers

---

Let us take  $h' = 6 \text{ km}$  and  $h = 10 \text{ km}$ , we get  $\delta t \sim 1.3 \text{ ns}$ . The total pulse duration will be the sum of these two effects (i.e. spread in pulse width because of difference in Cherenkov emission angles because of different wavelengths and because of different height. When the development of a  $1 \text{ TeV}$   $\gamma$  photon induced EAS shower is simulated through the Monte Carlo procedure, the value of Cherenkov pulse duration turns out to be  $\sim 5 \text{ ns}$ .

## 2.2 Cherenkov Radiation in Extensive Air Showers

When the cosmic rays enter the atmosphere, they interact with atmospheric nuclei by hadronic and electromagnetic interaction. Electrons and  $\gamma$ -rays interact electromagnetically, i.e. they generate secondary particles by '*pair production*' and '*Bremsstrahlung*'. The hadronic cosmic rays, namely protons and ionized nuclei interact via the hadronic interaction and also give rise to a numbers of secondary particles. The generation of secondary particles in the atmosphere is called the *Extensive Air Shower*.

### 2.2.1 Electromagnetic Showers

In the electromagnetic case, the loss of energy is due to '*pair production*' and '*Compton scattering*'. A very high energy  $\gamma$ -ray photon of minimum energy 1.022 MeV in the presence of atmospheric nuclei converts into relativistic electron-positron pairs (*'pair production'*). The first such interaction takes place at a height of  $\sim 20 \text{ km}$  above sea level (a.s.l.). These secondary electrons and positrons lose energy mainly via *Bremsstrahlung* to produce  $\gamma$ -rays. The resulting  $\gamma$ -rays produce more electron-positron pairs and these pairs in turn again produce more  $\gamma$ -rays. This cascade stops when ionization becomes the dominant channel to lose energy. The energy at which this condition is satisfied is called

## 2. GROUND BASED $\gamma$ -RAY ASTRONOMY

---

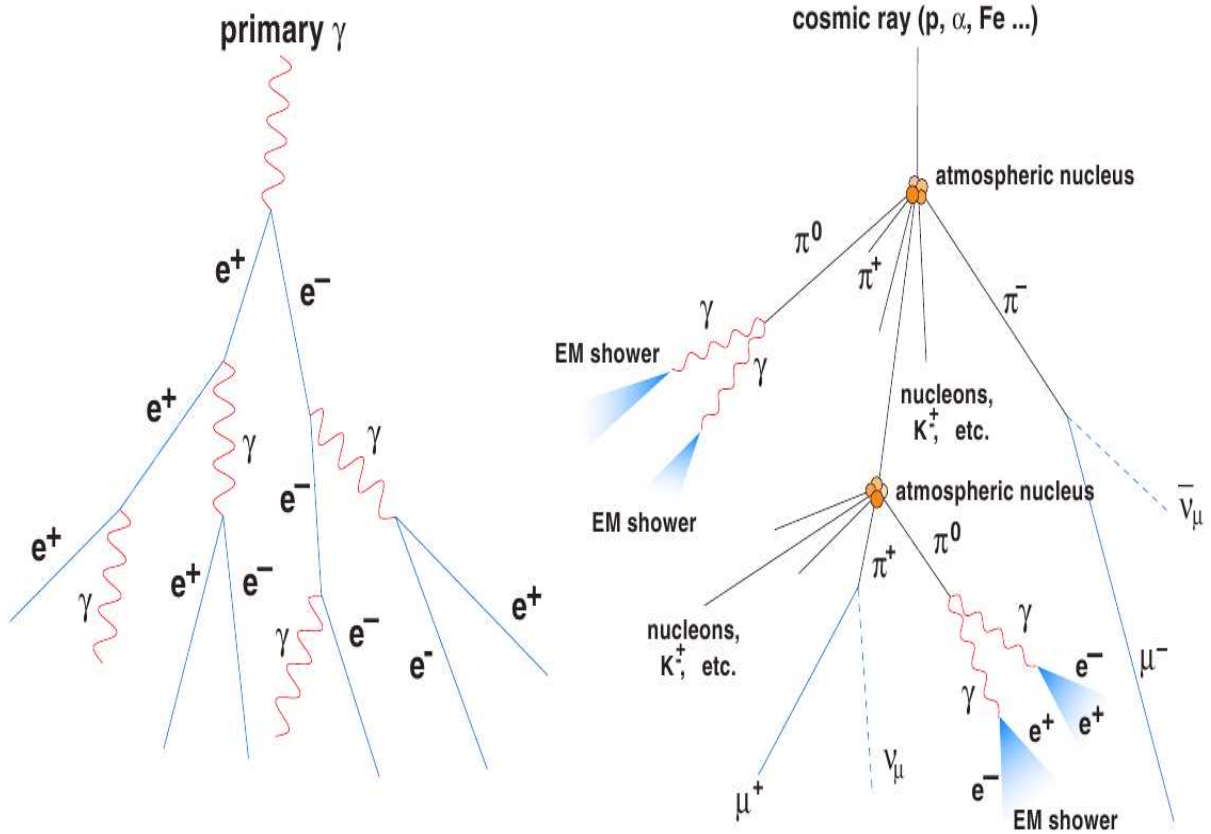


Figure 2.8: Electromagnetic and hadronic Extensive Air Showers

the critical energy  $E_c$  (which is  $\sim 83$  MeV for an electron in air). Almost simultaneously, when the average photon energy falls below 1.02 MeV, pair production stops and the number of secondary shower particles reaches its maximum. This height is known as the shower maximum. The shower maxima happens between  $\sim 13$  km and  $\sim 7$  km for  $\gamma$  rays energies between  $\sim 50$  GeV to few TeV. After shower maxima, the number of shower particles decay exponentially and the shower rapidly dies down.

### 2.2.1.1 Toy model of Electromagnetic showers

The basic approximation of the development of electromagnetic showers was introduced by Heitler [15]. This model considered the processes of pair production and Bremsstrahlung

## 2.2. Cherenkov Radiation in Extensive Air Showers

---

radiation emitted by the light charged leptons. It was assumed that at each vertex, the energy is equally distributed between particles produced and the radiation and both the radiation length for electron and interaction length for photon have same value, i.e.  $X_0^\gamma = X_0^e = X_0$ . (*Radiation Length* is defined as the length over which the electron is left with  $\frac{1}{e}$  of its original energy. This equals  $7/9$  of the mean free path for pair production. The radiation length for electron ( $X_0$ ) for Bremsstrahlung is  $36.8 \text{ g cm}^{-2}$  in air). The interaction length in another unit is defined as  $R = X_0 \ln 2$

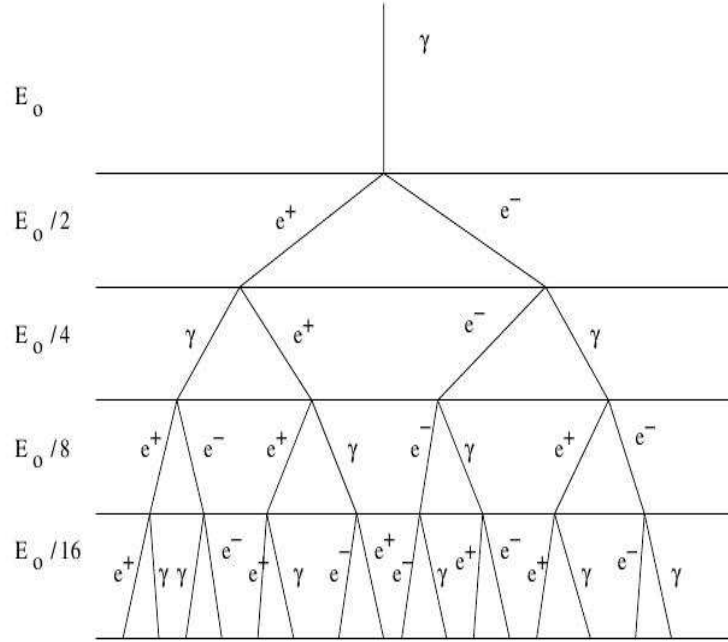


Figure 2.9: Heitler model for EM shower development

According to this simple model (Figure 2.9), after  $n$  radiation length, the number of particles is  $N(n) = 2^n$  with an mean energy of  $\frac{E_0}{2^n}$ . At the shower maximum, the total number of particles ( $e/e^{-1}$  and photons) are

$$N_{max} = E_0/E_c = 2^n. \quad (2.11)$$

## 2. GROUND BASED $\gamma$ -RAY ASTRONOMY

---

Therefore, the number of particles produced in an electromagnetic shower is given by

$$N(>E) = \int_0^{n(E)} Ndn = \int_0^{n(E)} 2^n dn = \frac{E_0/E}{\ln 2} \quad (2.12)$$

From this equation, the differential energy spectrum of the particles is given by

$$dN/dE \propto 1/E^2 \quad (2.13)$$

Therefore, according to Heitler model, we get

- The depth at which the shower reaches its maximum is proportional to the logarithm of the primary  $\gamma$ -ray energy.
- The number of particles at shower maxima are proportional to the energy of the primary  $\gamma$ -ray energy.

Both of above conclusions are supported by the study carried out by Monte Carlo simulations.

### 2.2.2 Hadronic Showers

When the high energy cosmic ray proton enters the top of atmosphere, it decays into pions. The hadronic showers mainly contain the decaying products of pions. Out of these pion products, the neutron pions decay into  $\gamma$ -rays, which again initiates the showers having the electromagnetic characteristics and therefore, these events are impossible to distinguish from those generated by the electromagnetic case. The schematic of electromagnetic and hadronic extensive air showers is shown in Figure 2.8. Nearly 90% of the

## 2.2. Cherenkov Radiation in Extensive Air Showers

---

secondary particles in a hadronic shower are pions and remaining 10% are kaons and antiprotons. Out of total pions, one third of neutral pion ( $\pi^0$ ) from the hadronic showers decay into  $\gamma$ -rays. Once the gamma rays from neutral pions are produced, they decay as an electromagnetic shower and hence it is impossible to distinguish this hadronic shower portions from genuine  $\gamma$ -ray initiated showers. The interaction length for protons is  $\sim 83$  gm  $cm^{-2}$  whereas for gamma rays it is  $\sim 36.8$  gm  $cm^{-2}$ . Therefore, the hadronic showers penetrate deeper into atmosphere compared to electromagnetic showers of similar energy. In case of hadronic showers, the transverse momentum carried out by pions and kaons is reflected in the larger lateral extent of extensive air shower compared to the electromagnetic showers. The intrinsic difference in the extensive air showers produced because of  $\gamma$  rays and protons is shown in Figure 2.10 [75].

The segregation of  $\gamma$ -rays initiated showers from the sea of cosmic ray showers is quite challenging because hadronic showers with the neutral pion decay in the  $\gamma$ -rays, in addition of cosmic rays outnumbering the  $\gamma$ -rays.

### 2.2.3 The Imaging Atmospheric Cherenkov Technique

When the high energy cosmic rays enter the atmosphere, they generate secondary particles in extensive air showers. These particles move with relativistic speeds and generate Cherenkov radiation in the atmosphere. The ground based detectors are used to detect this radiation. Such detectors collecting the Cherenkov photons falling on these telescopes are known as the Imaging Atmospheric Cherenkov Technique based telescopes. These telescopes consist of having a camera which collect the Cherenkov photons after getting reflected from the mirror. The camera consists of photomultiplier tubes which is

## 2. GROUND BASED $\gamma$ -RAY ASTRONOMY

---

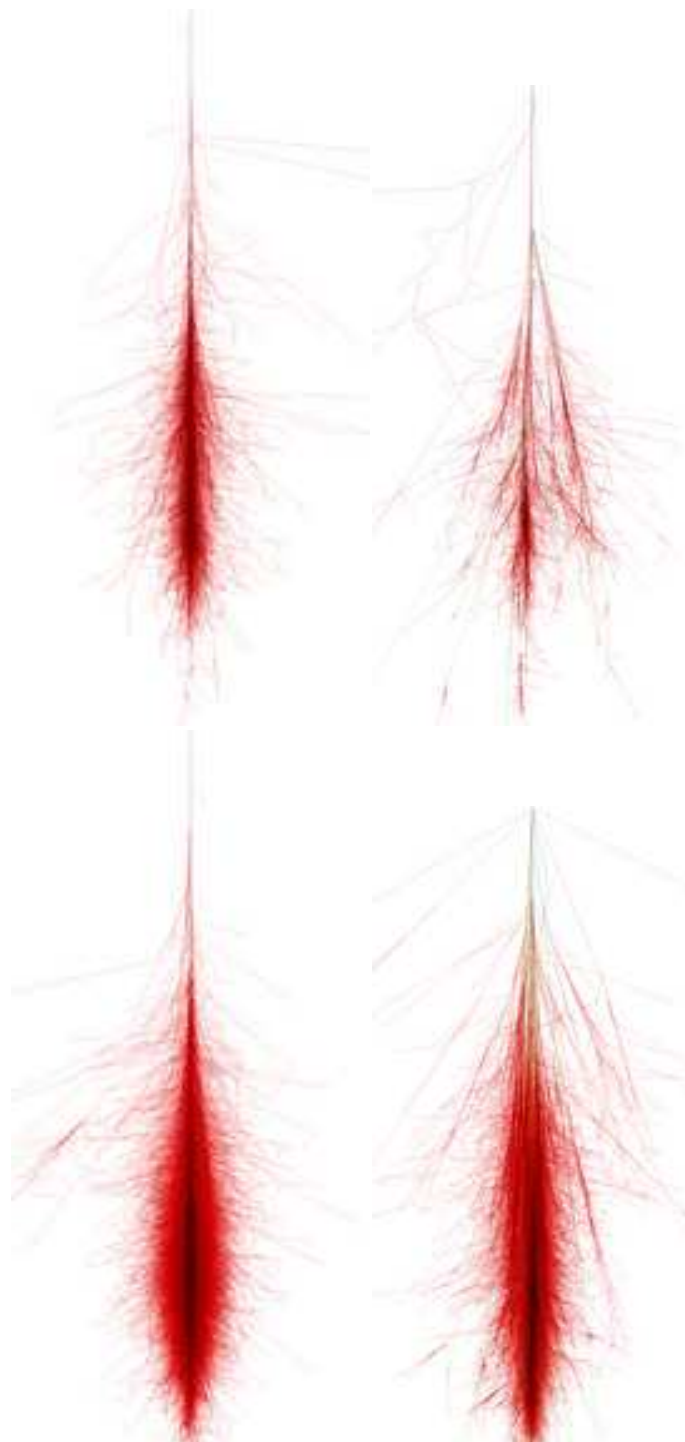


Figure 2.10: Monte Carlo simulation of a) 100 GeV  $\gamma$ : top left panel b) 100 GeV protons:top right panel, c) 1 TeV  $\gamma$ : bottom left panel b) 1 TeV protons:bottom right panel

## 2.2. Cherenkov Radiation in Extensive Air Showers

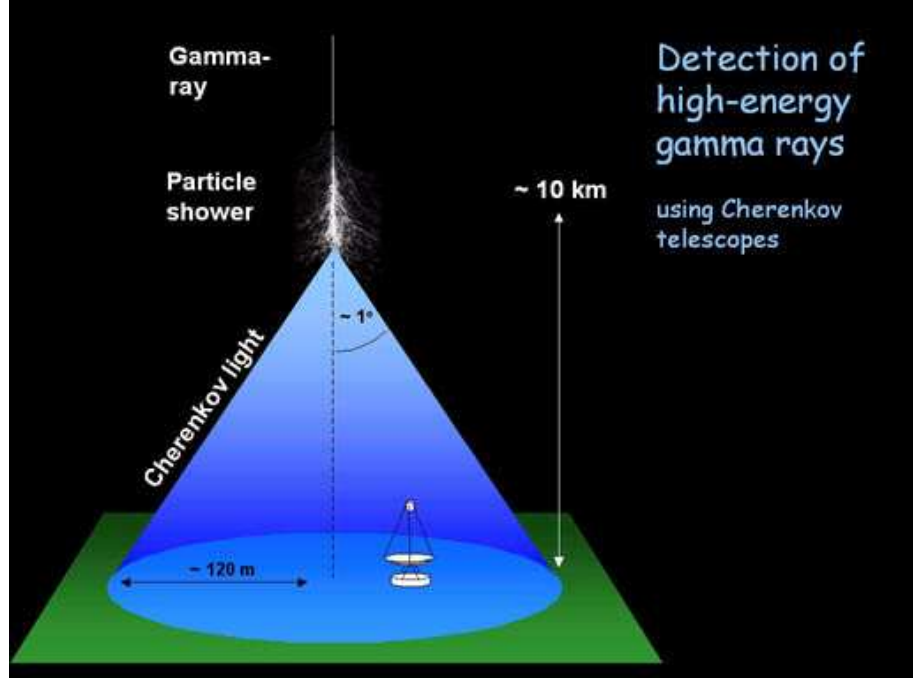


Figure 2.11: Imaging Atmospheric Cherenkov Technique

connected by the fast electronics which digitize the Cherenkov photon pulse and record it. The spatial distribution of such photons on the camera plane is known as the Image. This image is detected by the telescope, that is why this telescope is known as the **Imaging Atmospheric Cherenkov Technique** based telescope or simply IACT. The basic philosophy of this technique is shown in Figure 2.11.

### 2.2.3.1 Basic Principle

For an Atmospheric Cherenkov telescope, to a first approximation, we can derive an expression for the energy threshold at the trigger level . This approximation has been adopted from [76]. The light signal detected by the PMT camera is given by

$$S = \int_{\lambda_2}^{\lambda_1} kE(\lambda)T(\lambda)\eta(\lambda)Ad\lambda \quad (2.14)$$

## 2. GROUND BASED $\gamma$ -RAY ASTRONOMY

---

where  $C(\lambda)$  is the Cherenkov photon flux,  $E(\lambda)$  is the shower Cherenkov emission spectrum (proportional to  $1/\lambda^2$ ),  $T(\lambda)$  is the atmospheric transmission and  $k$  is a constant which depends on the shower and the geometry. The sky noise  $B$  is given by:

$$B = \int_{\lambda_2}^{\lambda_1} B(\lambda) \eta(\lambda) \tau A \Omega d\lambda. \quad (2.15)$$

where  $B(\lambda)$  is the night sky background,  $A$  is the mirror area,  $\eta(\lambda)$  is the photon collection efficiency,  $\tau$  is the trigger resolving time,  $\Omega$  is the solid angle. The signal must be detected above the fluctuations in the night-sky background during the integration time ( $\tau$ ) of the pulse counting system. The signal to noise ratio, therefore, at the trigger level is given by

$$\frac{S}{N} = \frac{S}{\sqrt{B}} = \int_{\lambda_2}^{\lambda_1} C(\lambda) [\eta(\lambda) A / \Omega B(\lambda) \tau]^{1/2} d\lambda. \quad (2.16)$$

The smallest detectable light pulse is inversely proportional to S/N; the minimum detectable gamma ray then has an energy threshold,  $E_T$  given by

$$E_T \propto \frac{1}{C(\lambda)} \sqrt{\frac{B(\lambda) \Omega \tau}{\eta(\lambda) A}} \quad (2.17)$$

It is clear from the equation 2.17 that for a IACT based telescope, the energy threshold can be lowered by

- installing the telescope at darker sites.
- using a large light collector area.
- increasing the mirror reflectivity

## 2.2. Cherenkov Radiation in Extensive Air Showers

---

- increasing the quantum efficiency of PMT

### 2.2.3.2 Flux sensitivity of Cherenkov telescope

If  $S$  is the number of gamma rays detected from a given source in a time  $T$ , and  $A_\gamma$  is the collection area for gamma-ray detection, then  $\gamma$ -ray signal at some energy threshold  $E$  is given by

$$S = F_\gamma(E)A_\gamma T \quad (2.18)$$

The telescope will register a background  $B$ , given by

$$B = F_{cr}A_{cr}(E)\Omega T \quad (2.19)$$

where  $A_{cr}(E)$  is the collection area for the detection of cosmic rays of energy  $E$ . The cosmic ray background has a power law spectrum

$$F_{cr}(> E) \propto E^{-1.7} \quad (2.20)$$

And if we assume that the gamma-ray source has the form

$$F_\gamma(> E_\gamma) \propto E_\gamma^{-a_\gamma} \quad (2.21)$$

Then the standard deviation is

$$N_\sigma \propto \frac{S}{\sqrt{B}} \propto E^{(0.85-a_\gamma)} \frac{A_\gamma}{\sqrt{A_{cr}\Omega}} \sqrt{T} \quad (2.22)$$

## 2. GROUND BASED $\gamma$ -RAY ASTRONOMY

---

The minimum number of standard deviations ( $\sigma$ ) for a reliable source detection is generally taken as 5. It is clear from the last equation that in order to get a confirm detection, the collection area for the  $\gamma$ -rays should be as large as possible. At the same time the product  $A_{cr}\Omega$  should be as small as possible. Therefore, the success of IACT based telescopes depends on efficient rejection of cosmic rays background in addition to high retention of  $\gamma$ -rays.

### 2.3 Parameterization of Cherenkov Radiation

The spatial distribution of Cherenkov photons on the camera plane is known as the Image. This distribution of Cherenkov photons is different for  $\gamma$ -rays and protons and hence  $\gamma$ -hadron segregation can be carried out on the basis of their shape and orientation. A typical Cherenkov photons distribution on the image plane of the camera generated by carrying out the Monte Carlo simulation for  $> 1$  TeV  $\gamma$  and 2 TeV protons energy range for a hypothetical camera shown in Figure 2.12.

A representative cartoon of Hillas parameter is shown in Figure 2.13. The image parameterization was introduced by *Hillas* and hence these parameters are known as Hillas parameters [26]. Image properties (analyzed off line) provide the information about the nature, the energy and the incoming direction of the primary particle of the shower. The Hillas parameters are characterized by carrying out the moment analysis [77, 78] of the images. Various image parameters and their correlation with the atmospheric Cherenkov radiation is summarized below.

- **Length (L) & Width (W)** : The rms spread of Cherenkov light along the ma-

### 2.3. Parameterization of Cherenkov Radiation

---

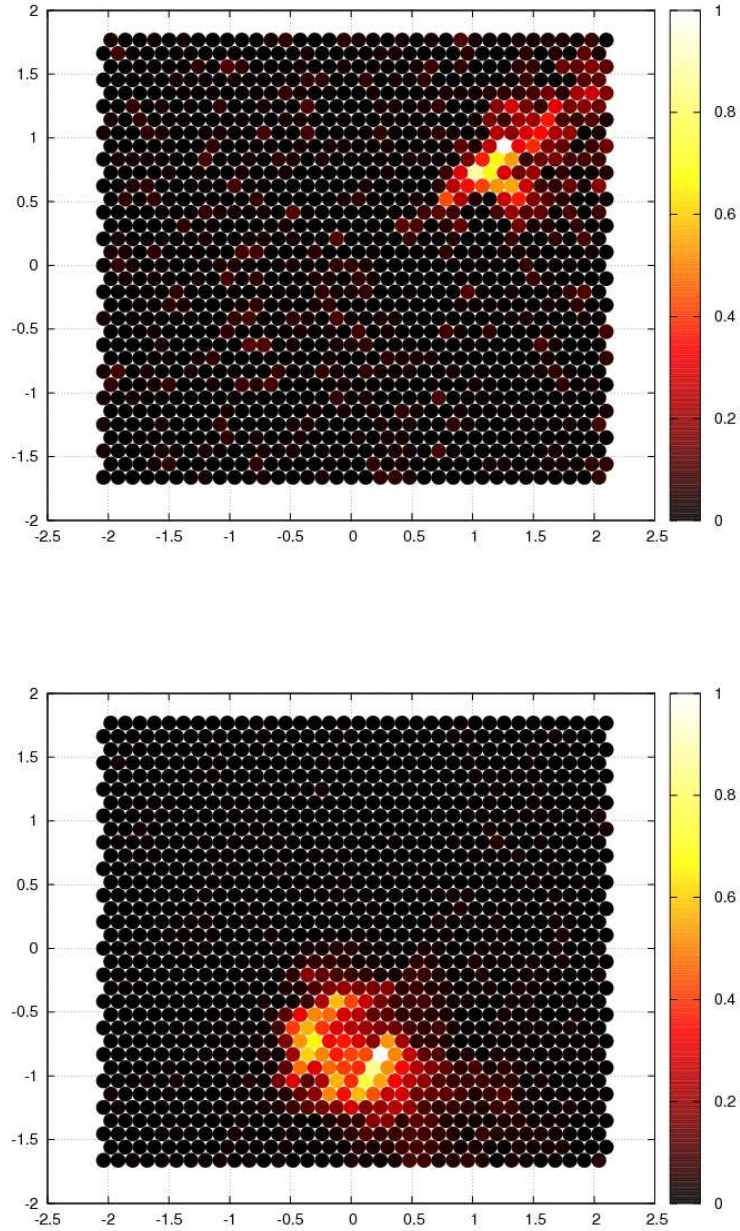


Figure 2.12: spatial distribution of cherenkov photons on the image plane of the camera. The top panel shows the distribution of  $\gamma$ -ray photons initiated shower in  $> 1$  TeV energy range. The bottom panel shows it for proton initiated shower for energies  $> 2$  TeV.

major/minor axis of image is known as the Length/width of an image. The Hillas parameter length demonstrates to the longitudinal development of the shower, whereas,

## 2. GROUND BASED $\gamma$ -RAY ASTRONOMY

---

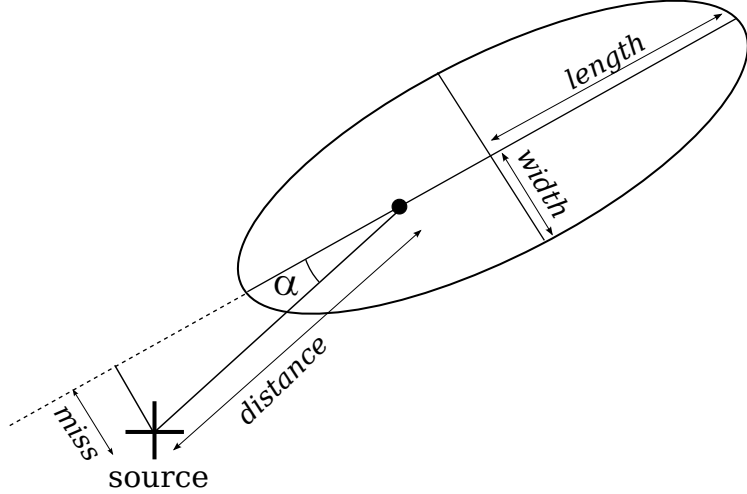


Figure 2.13: cartoon of few image parameters

the parameter width represents the lateral development of the shower.

- **Distance (D):** A first level measure of  $\gamma$ -initiated extensive air showers core distance is given by the distance parameter. The distance parameter represents the distance from the image centroid to the position of  $\gamma$ -ray source in the field of view. It is defined as the angle between the shower axis and the line joining the shower maximum and the telescope.
- **Size (S):** The total number of photoelectrons in a Cherenkov image is represented by the size parameter. This parameter is related to the energy of the primary cosmic ray particle.
- **Miss (M):** It is the perpendicular distance between the major axis of the image and the centre of the field of view of the camera. The shower orientation is related to this parameter.
- **Azwidth:** This parameter represents the RMS angular size along a line perpendicular

## 2.3. Parameterization of Cherenkov Radiation

---

ular to the line connecting the centroid of the image to the center of field of view.

The shape and orientation parameters are related to it.

- **Frac2 (F2):** It is defined as the ratio of the sum of the two highest pixel signal to the sum of all the signals and represents the degree of light concentration and thereby the compactness of the image.
- **Alpha ( $\alpha$ ):** It is the angle of the image between a line joining the centroid of the image to the centre of the field of view. It is a measure of the orientation of the shower axis. The  $\gamma$ -ray initiated showers are pointed towards the centre of the imaging camera (if the observed source is kept in the centre of the camera) and hence have very small value of  $\alpha$  compared to the angles subtended by the background events on account of their isotropic distribution. It is one of the strongest parameters for gamma-hadron segregation.
- **Asymmetry:** It is defined as the third moment of the intensity distribution along the major axis. It describes the skew of the image along its major axis.
- **Leakage:** It is defined as the ratio between the light content in the camera two outer most pixels to the total light content.

### 2.3.1 Estimation of image parameters

Estimation of the image parameters are carried out on the basis of moment analysis. The mathematical estimation is adapted from [71]. The zero order moment is the size. The first-order moments describe the position of the image. The second-order moments represent the extent of the image. In order to estimate various image parameters, the first

## 2. GROUND BASED $\gamma$ -RAY ASTRONOMY

---

step involves the determination of the image axis. It can be described as the equation of a straight line with slope  $m$  and intercept  $C$

$$y = Mx + C \quad (2.23)$$

The constants  $M$  and  $C$  are estimated by  $\chi^2$  minimization, i.e. by minimizing the signal weighted sum of squares of perpendicular angular distances of the pixels. Suppose  $x_i$  and  $y_i$  denote the pixel coordinates of the  $i^{th}$  pixel with origin being the center of the camera and  $s_i$  denotes the calibrated signal in the PMT, we can write the expression for  $\chi^2$  as

$$\chi^2 = \sum_{i=1}^n \frac{s_i (y_i - M x_i - C)^2}{1 + M^2} \quad (2.24)$$

where  $n$  is the total number of pixels. Assuming that both  $x_i$  and  $y_i$  have equal errors  $M$  and  $C$  can be obtained by differentiating the equation (2.24). The following quantities can be defined according to their standard definitions,

$$\langle x \rangle = \frac{\sum_{i=1}^n (s_i x_i)}{\sum_{i=1}^n s_i} \quad \langle y \rangle = \frac{\sum_{i=1}^n (s_i y_i)}{\sum_{i=1}^n s_i} \quad (2.25)$$

$$\langle x^2 \rangle = \frac{\sum_{i=1}^n (s_i x_i^2)}{\sum_{i=1}^n s_i} \quad \langle y^2 \rangle = \frac{\sum_{i=1}^n (s_i y_i^2)}{\sum_{i=1}^n s_i} \quad (2.26)$$

$$\langle x^3 \rangle = \frac{\sum_{i=1}^n (s_i x_i^3)}{\sum_{i=1}^n s_i} \quad \langle y^3 \rangle = \frac{\sum_{i=1}^n (s_i y_i^3)}{\sum_{i=1}^n s_i} \quad (2.27)$$

### 2.3. Parameterization of Cherenkov Radiation

---

$$\langle xy \rangle = \frac{\sum_{i=1}^n (s_i x_i y_i)}{\sum_{i=1}^n s_i} \quad (2.28)$$

$$\langle x^2 y \rangle = \frac{\sum_{i=1}^n (s_i x_i^2 y_i)}{\sum_{i=1}^n s_i} \quad \langle xy^2 \rangle = \frac{\sum_{i=1}^n (s_i x_i y_i^2)}{\sum_{i=1}^n s_i}. \quad (2.29)$$

Spread of the images in different directions can then be defined in terms of moments as

$$\sigma_{x^2} = \langle x^2 \rangle - \langle x \rangle^2 \quad \sigma_{y^2} = \langle y^2 \rangle - \langle y \rangle^2 \quad (2.30)$$

$$\sigma_{xy} = \langle xy \rangle - \langle x \rangle \langle y \rangle. \quad (2.31)$$

Some other higher order moments are

$$\sigma_{x^3} = \langle x^3 \rangle - 3 \langle x^2 \rangle \langle x \rangle + 2 \langle x \rangle^3 \quad (2.32)$$

$$\sigma_{y^3} = \langle y^3 \rangle - 3 \langle y^2 \rangle \langle y \rangle + 2 \langle y \rangle^3 \quad (2.33)$$

$$\sigma_{x^2 y} = \langle x^2 y \rangle - 2 \langle xy \rangle \langle x \rangle - \langle x^2 \rangle \langle y \rangle + 2 \langle x \rangle^2 \langle y \rangle \quad (2.34)$$

$$\sigma_{xy^2} = \langle xy^2 \rangle - 2 \langle xy \rangle \langle x \rangle - \langle y^2 \rangle \langle x \rangle + 2 \langle y \rangle^2 \langle x \rangle. \quad (2.35)$$

## 2. GROUND BASED $\gamma$ -RAY ASTRONOMY

---

Defining

$$d = \sigma_{y^2} - \sigma_{x^2} \quad (2.36)$$

$$z = \sqrt{d^2 + 4(\sigma_{xy})^2}. \quad (2.37)$$

The constants of the image axis are then written as follows:

$$M = \frac{d + z}{2\sigma_{xy}} \quad (2.38)$$

$$C = \langle y \rangle - M \langle x \rangle. \quad (2.39)$$

The image parameters can be calculated from these moments and can be written as

$$\text{length}, \quad L = \sqrt{\frac{\sigma_{x^2} + \sigma_{y^2} + z}{2}} \quad (2.40)$$

$$\text{width}, \quad W = \sqrt{\frac{\sigma_{x^2} + \sigma_{y^2} - z}{2}}. \quad (2.41)$$

Since  $\langle x \rangle$  and  $\langle y \rangle$  are the coordinates of the image centroid, therefore

$$\text{distance}, \quad D = \sqrt{\langle x \rangle^2 + \langle y \rangle^2} \quad (2.42)$$

$$\text{miss}, \quad Ms = \sqrt{\frac{1}{2}((1 + \frac{d}{z})\langle x \rangle^2 + (1 - \frac{d}{z})\langle y \rangle^2) - \frac{2\sigma_{xy}\langle x \rangle \langle y \rangle}{z}} \quad (2.43)$$

$$alpha, \quad \alpha = \sin^{-1} \left( \frac{Ms}{D} \right) \quad (2.44)$$

$$azwidth, \quad Az = \sqrt{(L^2 \sin^2 \alpha + W^2 \cos^2 \alpha)} \quad (2.45)$$

$$asymmetry = \frac{(\sigma_{x^3} \cos^3 \phi + \sigma_{y^3} \sin^3 \phi + 3\sigma_{x^2 y} \cos^2 \phi \sin \phi + 3\sigma_{x y^2} \cos \phi \sin^2 \phi)^{1/3}}{L} \quad (2.46)$$

$$concentration \quad F2 = \frac{s_{Ist\ max} + s_{IIInd\ max}}{\sum_{i=1}^n s_i}. \quad (2.47)$$

Where  $s_{Ist\ max}$  and  $s_{IIInd\ max}$  are maximum and second maximum signal respectively contained in pixels of an image. The Hillas parameters in different energy ranges, i.e.  $E_\gamma > 1$  TeV and  $E_\gamma > 20$  GeV will be shown in chapter 3 and chapter 4 respectively.

## 2.4 The TACTIC Telescope

The TACTIC (TeV Atmospheric Cherenkov Telescope with Imaging Camera)  $\gamma$ -ray telescope [79] is an IACT based telescope which has been in operation at Mt. Abu ( $24.6^\circ N$ ,  $72.7^\circ E$ ,  $\sim 1300$  m asl), Rajasthan in Western India for the study of TeV  $\gamma$ -ray emissions from astrophysical sources. The telescope employs a 349-pixel photomultiplier tube imaging camera with a uniform pixel resolution of  $\sim 0.3^\circ$  and a  $\sim 5.9^\circ \times 5.9^\circ$  field-of-view to collect atmospheric Cherenkov events generated by extensive air shower due to charged cosmic-rays or  $\gamma$ -rays. The TACTIC telescope is shown in Figure 2.14.

The TACTIC telescope uses an F/1 type tracking light-collector of  $\sim 9.5$

## 2. GROUND BASED $\gamma$ -RAY ASTRONOMY

---



Figure 2.14: TACTIC telescope

$\text{m}^2$  area. It consists of aluminium coated 34 front-face glass spherical mirrors of 60 cm diameter each with a focal length  $\sim 400\text{cm}$ . The innermost 121 pixels ( $11 \times 11$  matrix) are used for generating the event trigger based on the philosophy of Nearest Neighbour Non-collinear Triplets. The telescope employs a CAMAC based 12-bit Charge to Digital Converters (CDC). The data acquisition and control system [80] runs on the QNX (version 4.25) real-time operating system. The digitization of triggered events are carried out by

## 2.4. The TACTIC Telescope

---

CAMAC based 12-bit Charge to Digital Converters (CDC). These CDC have a full scale range of 600 pico coulombs. The relative gain of the photomultiplier tubes is monitored regularly [81] once in 15 minutes by flashing a red LED, placed at a distance of  $\sim 1.5$  m from the camera.

The data acquisition and control of the TACTIC is handled by a network of PCs. One PC is used to monitor the scaler rates and control the high voltage of the PMTs. The LED calibration and the data acquisition of the events is handled by the other PC. These two PCs, named as *rate stabilization* and the *data acquisition nodes* respectively, along with a master node form the multi node Data Acquisition and Control network of the TACTIC Imaging telescope. The telescope has a pointing and tracking accuracy of better than  $\pm 3$  arc-minutes. The tracking accuracy is checked on a regular basis with so called “pointing runs”, where an optical star having its declination close to that of the candidate  $\gamma$ -ray source is tracked continuously for about 5 hours. The pointing run calibration data is then incorporated so that appropriate corrections can be applied. TACTIC records cosmic-ray events with a rate of  $\sim 2.0$  Hz at a typical zenith angle of  $15^\circ$  and is operating at a  $\gamma$ -ray threshold energy of  $\sim 1$  TeV.

The first detection from the TACTIC telescope was a very interesting results in which TACTIC telescope detected Markarian 501 in high flaring state [82]. The flaring activity in terms of flux enhancement increased by a factor of 10-Crab-flux during a contemporaneous multiwavelength observations in April 1997 by Whipple group along with Telescope array [83] and HEGRA. The TACTIC telescope observed Markarian 501 in April-May 1997 during its very first observing campaign. The source was detected with

## 2. GROUND BASED $\gamma$ -RAY ASTRONOMY

---

a statistical significance of  $14.2\sigma$ . The corresponding source light curve is displayed in Figure 2.15. The light curves showed excellent morphological similarity during the flar-

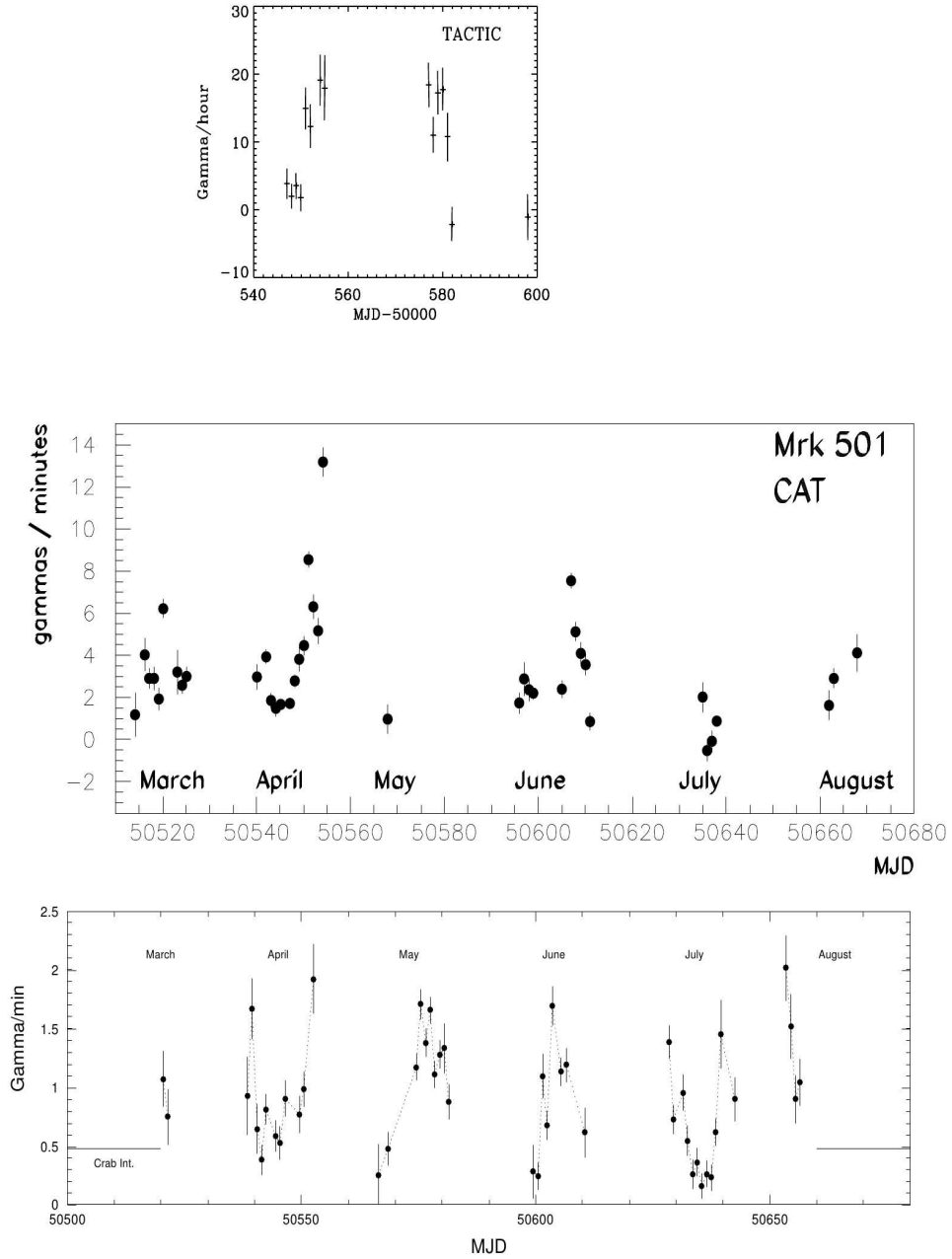


Figure 2.15: Comparison of light curves from: (a) top TACTIC (b) middle CAT (c) bottom TA

ing episodes extending for several days. During the observation of Markarian 501 from

## 2.4. The TACTIC Telescope

---

TACTIC ( (April 9 - May 30, 1997), the source was found flaring at nearly 2 Crab units. The energy threshold of TACTIC was  $\sim (0.7 \pm 0.2)$  TeV. This result was in excellent agreement with the source spectrum inferred by independent observations carried out by the CAT, HEGRA and the Whipple groups.

Thereafter, TACTIC telescope detected various extragalactic sources [84, 85, 86, 87, 88, 89, 90] during the course of its operation. A comprehensive review of the observation of standard astrophysical source Crab Nebula by the TACTIC telescope was carried out [91] by taking  $\sim 400$  h from 2003-2010. The resulting  $\gamma$ -ray rate for the on-source data is determined to be  $\sim (9.31 \pm 0.48)h^{-1}$ . A power law fit  $\frac{d\Phi}{dE} = f_0 E_0^{-\Gamma}$  with  $f_0 \sim (2.66 \pm 0.29) \times 10^{-11} cm^{-2}s^{-1}TeV^{-1}$  and  $\Gamma \sim 2.56 \pm 0.10$  was observed. The spectrum matches reasonably well with that obtained by other groups. A recent upgrade of TACTIC telescope led to a substantial improvement in the detection sensitivity of the TACTIC telescope. Compared to  $5\sigma$  detection of signal in  $\sim 25$  h, the upgrade lead to the detection of signal in  $\sim 13$  h.



# 3

## Various machine learning methods

### 3. VARIOUS MACHINE LEARNING METHODS

---

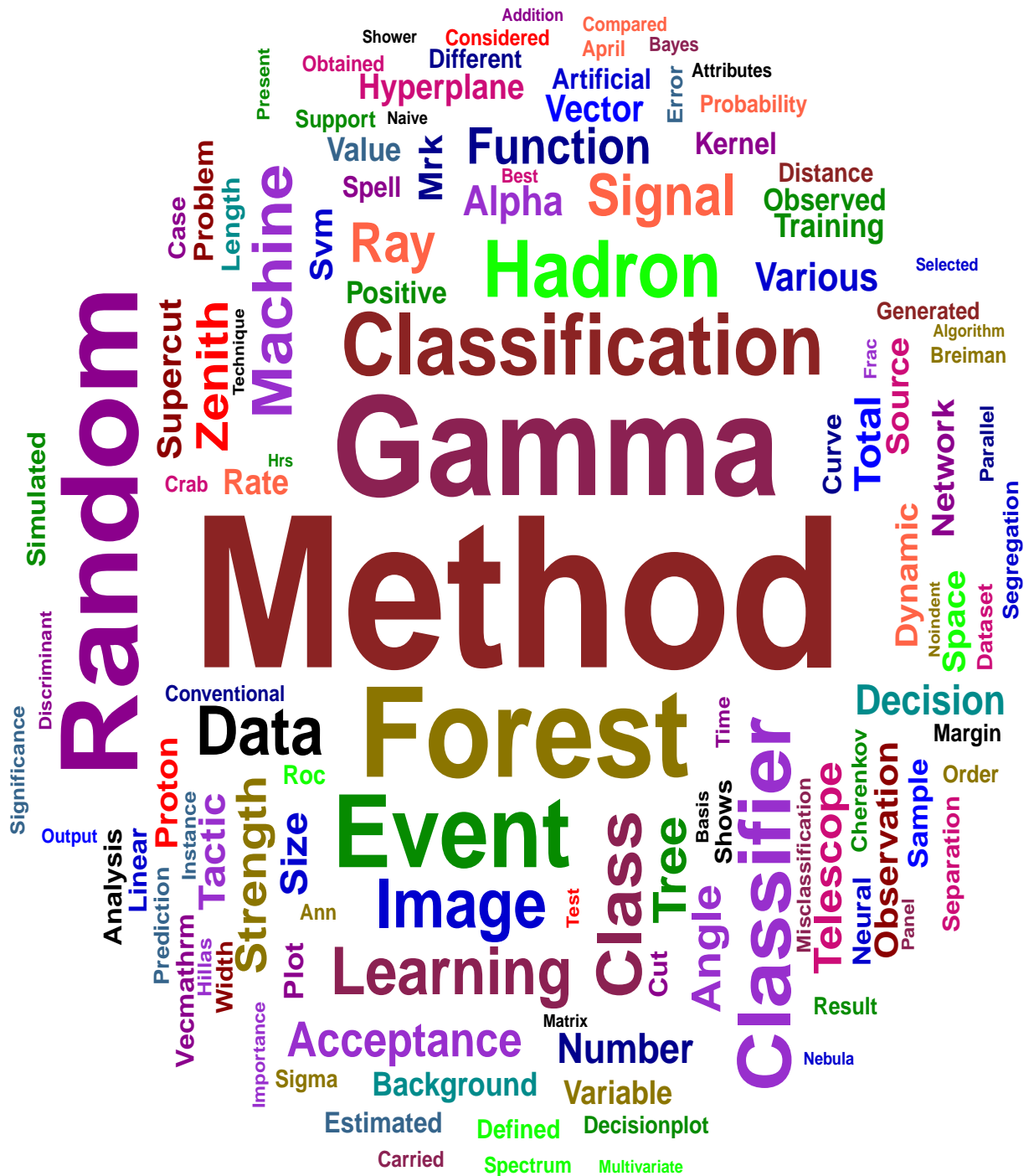


Figure 3.1: Summary of Chapter 3. The size of word represents the number frequency.

### 3.1. Introduction

---

In this chapter, we present a detailed case study of  $\gamma$ -hadron segregation for ground based atmospheric Cherenkov telescope. We have evaluated and compared various supervised machine learning methods such as Random Forest, Support Vector Machine, Artificial Neural Network, Naive Bayes Classifiers, Standard Discriminant Analysis as well as the conventional dynamic Supercuts method by taking the Monte Carlo simulated events triggering the TACTIC Cherenkov telescope. It is demonstrated that the Random forest method is the most sensitive machine learning method for  $\gamma$ -hadron segregation. Subsequently, this chapter will discuss the validation of Random Forest method by re-analysing the Markarian 421 (Mrk 421) data collected by the TACTIC  $\gamma$ -ray telescope.

## 3.1 Introduction

Multidimensional datasets are very difficult to handle with the conventional methods. Therefore, when multidimensional data is encountered, the efficiency of these methods reduces drastically as any inter dependence among various parameters is beyond the realm of conventional methods. In the case of ground based atmospheric Cherenkov systems, the typical characterization of signal involves multidimensional data. The present day Cherenkov systems operate in an energy regime where the conventional methods are losing their edge on account of fading differences among the discriminating attributes/parameters between signal and background. Therefore, the ground based gamma-ray astronomy community has started exploring various options including multivariate methods.

The machine learning methods fall under the umbrella of multivariate methods. The simplicity and intrinsic ability of these methods to scrub out inter dependence, if

### **3. VARIOUS MACHINE LEARNING METHODS**

---

any, among various attributes/parameters has made the field of machine learning methods as one of the fastest growing scientific disciplines. These methods employ statistical tools to decipher hidden relationship, if any, among few or a collection of attributes/parameters with comparatively very little computing infrastructure.

Machine learning methods have become one of the most popular tools to solve the problems in the data driven world. These methods were originated from the studies of computational learning theory and pattern recognition in which computers were enabled to solve the problem without explicitly being programmed. Here the algorithm learns and makes prediction by learning from the data itself. Prior to 1980s, almost all learning methods were based on linear decision surfaces and had nice theoretical properties. In 1980s, non linear decision surfaces were employed by decision trees and Neural networks. However, these methods suffered from local minima problem as well as had little theoretical basis. In 1990s, the computational learning theories were used in developing efficient learning algorithm for non linear functions having good theoretical properties. Support vector Machines are one of these machine learning methods. Machines learning methods can broadly be classified into three categories. These are: Supervised learning, Unsupervised learning and Reinforcement learning. In supervised learning, the input and output labels are available whereas no labels are available in unsupervised learning.

The machine learning methods have been explored in the field of ground based gamma ray astronomy for quite sometime. The earliest efforts were initiated by Bock et. al. [92]. Later on, for  $\gamma$ -hadron segregation, the effectiveness of tree based

### 3.1. Introduction

---

multivariate classifiers was demonstrated by two operational ground based observatories: MAGIC [93] and HESS [94, 95, 96]. It is to be noted that no machine learning method is sacrosanct as far as its superiority over other multivariate methods exist. Each dataset is unique and the classifier performance is dependent on the dataset under investigation. Therefore, in order to assess the suitability of a classifier, each dataset needs to be probed independently.

In this Chapter (3), we compare and evaluate various supervised machine learning methods to assess their suitability for  $\gamma$ -hadron segregation. A total of 5 machine learning methods, namely *Random Forest*, *Artificial Neural Network*, *Linear Discriminant method*, *Naive Bayes Classifier* and *Support Vector Machine with Radial Basis Function and polynomial kernel* have been investigated. They are selected in a way to represent a type of machine learning stream. The Random Forest method represents the logic based algorithm. The Artificial Neural Network methods are Perceptron based techniques. The Standard Discriminant method and Naive Bayes Classifier are statistical learning methods. The Support Vector Machine represents a rather new (1992) machine learning technique. The plan of the chapter is as follows: Section 3.2 involves the description of the simulation database employed to compare various machine learning methods. The subsequent sections provide an overview of all the machine learning methods. The final two sections deal with the critical analysis of all the classifiers and the conclusion respectively.

### 3. VARIOUS MACHINE LEARNING METHODS

---

## 3.2 Database used in this study

A Monte Carlo simulated database was generated by using the CORSIKA air shower code [97] with the Cherenkov option. The simulations were carried out for the TACTIC telescope [98] at the Mount Abu observatory altitude of  $\sim 1300\text{m}$ . The showers were generated at zenith angles of  $5^0$ ,  $15^0$ ,  $25^0$ ,  $35^0$  and  $45^0$ . The imaging camera with a total of 349 pixels was considered with the innermost 121 pixels being used for generating the trigger. The Cherenkov photons triggered the telescope after encountering the wavelength dependent photon absorption, reflection coefficient of the mirror facets, light cone used in the camera and the quantum efficiency of photomultiplier tubes. All the triggered events underwent the usual image cleaning procedures [99] to eliminate the background noise. The simulated events triggering the telescope were selected according to the differential spectral index 2.6 and 2.7 for  $\gamma$  and protons respectively. In order to have a robust and well contained image inside the camera, the pre-filtering cuts of Size (photoelectrons)  $\geq 50$  and  $0.4^0 \leq \text{Distance} \leq 1.4^0$  were applied.

### 3.2.1 Image parameters for classification

Various Hillas image parameters [26] like length, width, distance, size (photoelectron), zenith angle can be used as classifying parameters for  $\gamma$ -hadron segregation. However, the size parameter as well as the zenith angle parameter are not strictly separation parameters of gamma and hadronic showers. Zenith angle, for instance, by itself can not be used to separate the events although different image parameters depend on it. Same is true with the size (photoelectron) parameter. A typical problem with these parameters is that in

### **3.2. Database used in this study**

---

case the training samples for gammas and hadrons have a different distribution in these parameters, only then these parameters may be reckoned as separation parameters. This may lead to a rather risky situation, and which is typically handled by preparing the training samples in such a way that their distributions on those parameters (typically size and zenith) are as close as possible. In this way, the uncertainty associated with separation by such parameters as separation parameters have been avoided. Following this, these parameters could still be used for separation. In this study, such complexities have been taken into account.

In addition to these parameters, a derived parameter 'dens', defined [100] as

$$\text{dens} = \frac{\log_{10}(\text{size})}{\text{length} \times \text{width}} \quad (3.1)$$

was also used.

The frequency distribution of various Hillas parameters simulated for the TACTIC telescope is shown in Figure 3.2. A total of two sets of image parameters were considered. The idea was to investigate various classifiers as a function of image attributes/parameters. In the first instance, only 5 image parameters: length, width, distance, size and Frac2 were considered from the simulation database. In the second case, we considered a total of 7 parameters. Here, in addition to the above mentioned 5 parameters, two additional parameters: *zenith angle* and *dens* parameter were also included. However for the classification purpose, alpha parameter was not considered. The alpha is a very powerful parameter as it carries the signature of the progenitor ( $\gamma$  or

### 3. VARIOUS MACHINE LEARNING METHODS

---

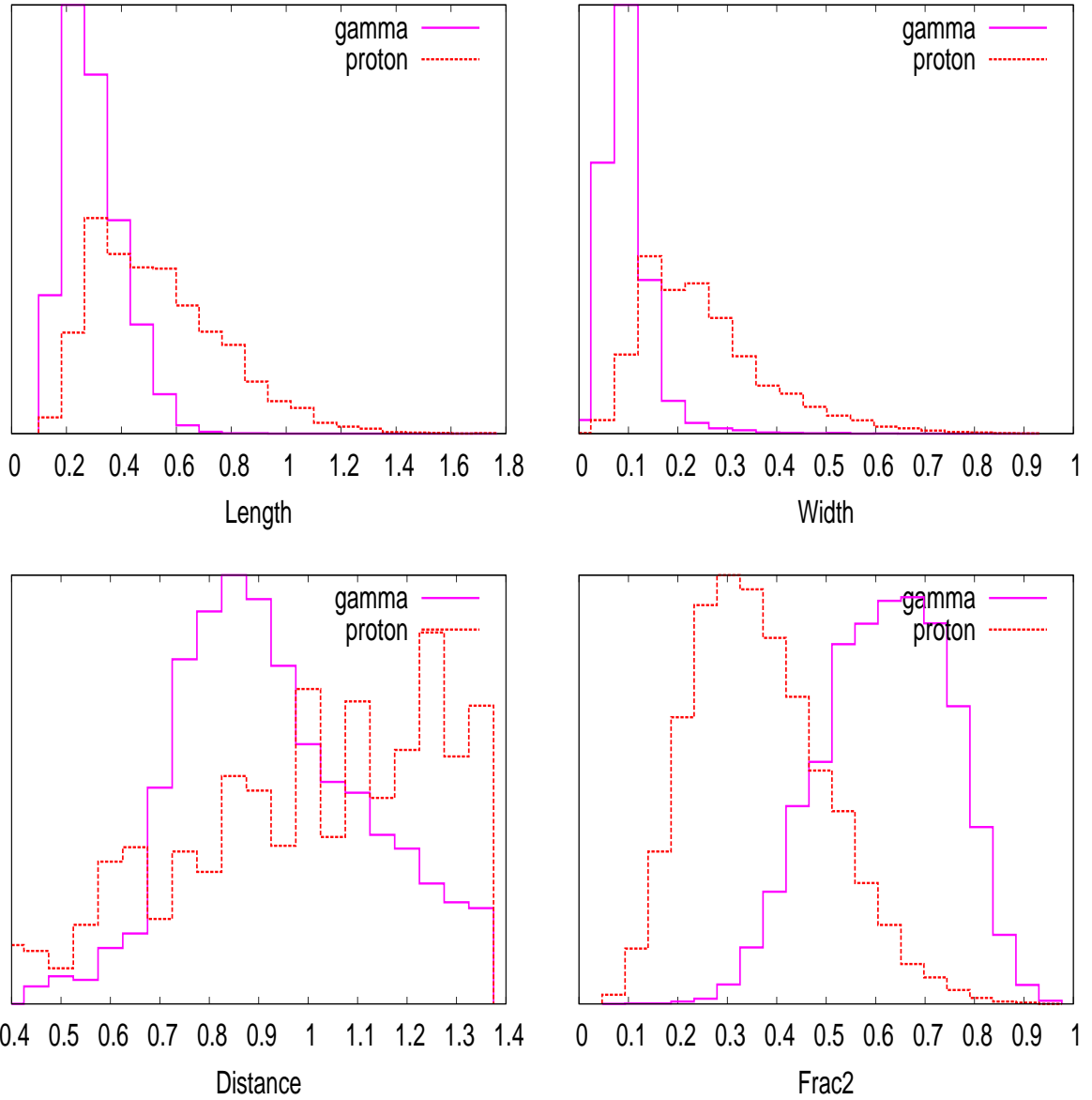


Figure 3.2: Frequency distribution of Hillas parameters distribution for Gamma, Proton initiated showers triggering the TACTIC telescope.

proton). The alpha distribution is expected to be flat for cosmic ray protons whereas it reflects a peaky behaviour, generally  $\leq 18^\circ$  for  $\gamma$ -rays. In order to remove any bias of such a strong parameter, it was not considered for the classification purpose. Moreover, this parameter plays a crucial role in the estimation of signal strength. If the alpha parameter

### 3.3. Different classification methods

---

is used in the classification then the hadronic background can not be evaluated.

## 3.3 Different classification methods

The problem of  $\gamma$ /hadron segregation is formulated as a two class problem:  $\gamma$  represents one class and the hadron is the second class. In literature, a large varieties of multivariate classification methods exist. However, to have a tractable analysis, a few representative supervised machine learning methods were selected. The classification was carried out by using 4 different machine learning methods, namely *Random Forest (RF)*, *Artificial Neural Network (ANN)*, *Linear Discriminant method (LDM)*, *Naive Bayes (NB) Classifier and Support Vector Machine (SVM) with Radial Basis Function (RBF) and polynomial kernel*. Except the RF and the Dynamic Supercuts method, rest of the methods were used from a commercially available package named STATISTICA [101]. The Random Forest method was studied by using the original Random Forest code [102].

### 3.3.1 Conventional method: Dynamic Supercuts

The spatial distribution of Cherenkov photons on the image plane of the camera is parameterized on the basis of shape and size (light content) of each such image. The conventional parameterization leads to the estimation of the image parameters [26]. In this technique, various sequential cuts in the image parameters are applied so as to maximize the  $\gamma$ -ray like signal events and reject maximum number of background events. However, this scheme has a disadvantage because the width and length parameters grow with the primary energy. It is observed that width and length of an image are well correlated with the logarithm of size. And size of the image provides an estimate of the primary energy. This method of scaling the width and length parameters with the size is known

### 3. VARIOUS MACHINE LEARNING METHODS

---

as the dynamic Supercuts method [103, 104]. By employing this method, the optimum number of cut parameters and their values were estimated by numerically maximizing the so called Quality factor Q [105]. The quality factor is defined as  $S = \frac{\epsilon_\gamma}{\sqrt{(\epsilon_P)}}$  where  $\epsilon_\gamma$  and  $\epsilon_P$  are the  $\gamma$  and hadron acceptances respectively. After the numerical maximization of the quality factor [106, 107], the following set of image parameters were applied for  $\gamma$ /hadron classification.

---

Length (L)	$0.110^0 \leq L \leq (0.235 + 0.0265 \ln(size))$
Width	$0.065^0 \leq W \leq (0.085 + 0.0120 \ln(size))$
DISTANCE (D)	$0.4^0 \leq D \leq 1.4^0$
SIZE (S)	$S \geq 50 \text{ pe}$
Alpha ( $\alpha$ )	$\leq 18^0$

---

#### 3.3.2 Artificial Neural Network

The ANN consists of many inputs [108] which are multiplied by weights (strength of the respective signals), and then computed by a mathematical function which determines the activation of the neuron. Another function computes the output of the artificial neuron. The specific output demanded by the user can be obtained by adjusting the weights of an artificial neuron. Multilayer perceptron (MLP) is perhaps the most popular network architecture which was introduced by Rumelhart and McClelland [109] and discussed at length in most neural network textbooks [110]. Each neuron performs a weighted sum of its inputs and passes it through the transfer function to produce the output. In this work

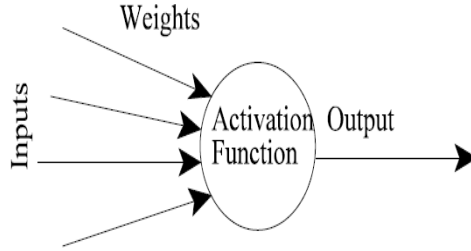


Figure 3.3: Schematic of a typical artificial neural network

we use a multilayer perceptron network with 5 inputs, minimum hidden units 3, maximum hidden units 11 and networks to train 20. For classification tasks, the probabilistic output was generated and misclassification rate was estimated.

### 3.3.3 Naive Bayes Classifier

The Bayesian classifiers gained prominence in early nineties and perform very well [111, 112]. A Naive Bayes classifier is a generative classifier technique based on the concept of probability theory. The Bayes theorem plays a critical role in probabilistic learning and classification. The Bayes theorem states that

$$p(B/A) = \frac{p(A/B)p(B)}{p(A)} \quad (3.2)$$

where,

$p(A)$  = Independent probability of A

$p(B)$  = Independent probability of B

$p(A/B)$  = Conditional probability of A given B

### **3. VARIOUS MACHINE LEARNING METHODS**

---

$p(B/A)$  = Conditional probability of B given A, i.e. the posterior probability.

In “Naive Bayes Classification” the different variables/attributes/features are assumed to be strongly (naive) independent, i.e.,

$$p(< x_1, x_2, x_3 \dots x_n > | y) = \prod_{i=1}^n \Pi(x_i|y) \quad (3.3)$$

Using the strong “independence assumption” and the prior probabilities, the most probable class for a given x is estimated. The best class is the most likely or maximum posteriori (MAP) class. The MAP estimate gives

$$\arg \max_B p(B/A) = \arg \max_B p(A/B) p(B) \quad (3.4)$$

The training and evaluation from this method is very fast but the assumption of strong independence among parameters is a condition generally not satisfied in the real world problem.

#### **3.3.4 Standard Discriminant Analysis**

Standard Discriminant Analysis is also known as Discriminant Function Analysis (DFA). DFA combines the aspects of multivariate analysis of variance with the ability to classify observations into known categories. It is a multivariate technique which not only contributes in the classification but also estimates how good the classification is. In this method, the discrimination functions like canonical correlations are constructed and each function is assessed for significance. The estimation of the significance of a set of discrim-

### 3.3. Different classification methods

---

inant functions is computationally identical to multivariate analysis of variances. After estimating the significance, one proceeds for classification. It generally turns out that first one or two functions play an important role while the rest can be neglected. Each discrimination function is orthogonal to the previous function.

In the present case, it is known that each class belongs to either  $\gamma$  or hadron.; thus, a priori probability of these classes are known. In this work, the prior probabilities are taken for classification.

#### 3.3.5 Support Vector Machine

Support Vector Machines (SVMs) are a set of supervised learning algorithms developed by Vladimir Vapnik in the mid 90's for classification and regression problems. SVMs learn by example to make prediction about new instances. SVMs algorithms are based on statistical learning theory and has a wide range of applications in the real world problems. Due to its sound mathematical foundation, SVMs have become one of the most popular machine learning methods in recent times. The SVM was introduced by Boser, Guyon and Vapnik [113] in 1992. SVM belong to supervised machine learning models used for classification and regression. It is based on the concept of decision planes termed as hyperplanes. The Hyperplanes are constructed in the multidimensional space for classification. The decision planes separate the classes. SVM estimates the decision planes between different known classes of objects and applies the decision planes to objects of unknown classes. These unknown objects are classified based on their position in the multidimensional parameter space with respect to the separation boundaries. The Basic idea of SVM incorporates two components: 1. Optimal hyperplane for linearly separable

### 3. VARIOUS MACHINE LEARNING METHODS

---

structures. 2. Extending the structures which are not linearly separable by mapping the data to a higher dimensional space, i.e. the kernel trick.

#### 3.3.5.1 Support Vector Machines for binary classification problem

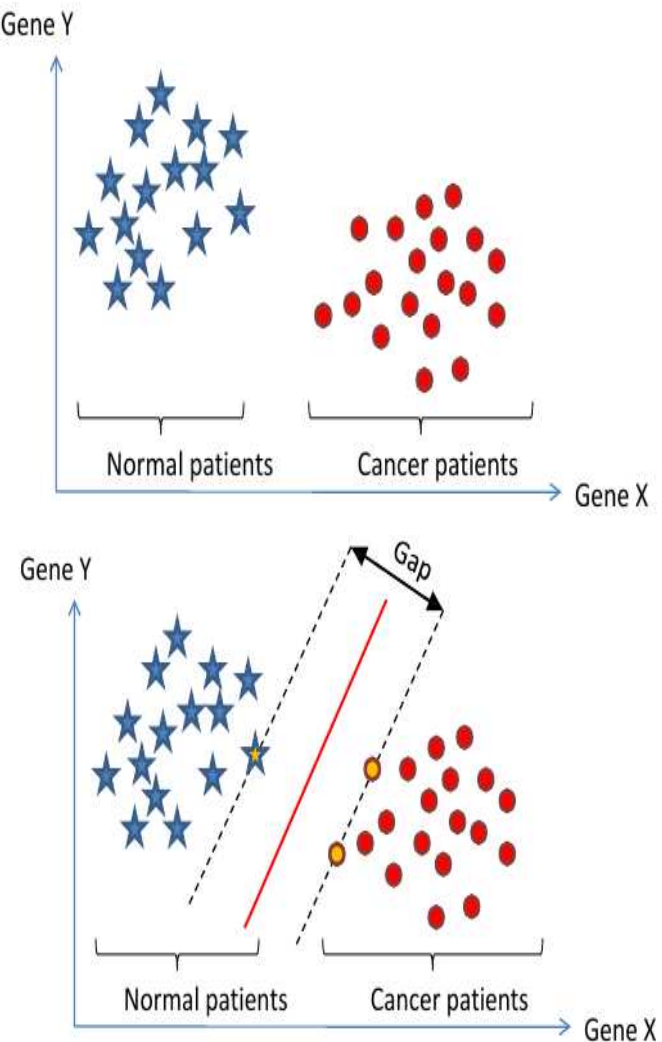


Figure 3.4: Classification problem

Let us consider a dataset consisting of two classes represented by red dots and blue dots.

Now, find a linear surface, technically known as "*hyperplane*" which can separate the two classes (red and blue) and has the largest distance (gap, technically known as "*margin*") between the border line classes. The largest distance between the border line cases is

### 3.3. Different classification methods

---

technically known as "*Support Vectors*". A typical example is shown in Figure 3.4. In Support Vector Machines, the two classes are separated by a optimal hyperplane by using the biggest possible margin. Margin is a distance between optimal hyperplane and a vector which lies closest to it. Maximizing the margin between the training patterns and the decision boundary has many advantages [113]. It amounts to minimizing the maximum loss, as opposed to some average quantity such as the mean squared error. This has several desirable consequences: 1) The resulting classification rule achieves an error less separation of the training data if possible. 2) Outliers or meaningless patterns are identified by the algorithm and can therefore be eliminated easily with or without supervision. This contrasts classifiers based on minimizing the mean squared error, which quietly ignore atypical patterns.

#### 3.3.5.2 Statement of linear SVM

For the case of linearly separable data, let us suppose that for a given set  $X$  of training samples  $\mathbf{x}_i \in \mathbb{R}^d$  and the corresponding labels  $y_i \in \{-1, 1\}$ ,  $i = 1, \dots, n$ , SVM would like to find a classifier, i.e. a hyperplane to separate the one class from the another (negative instances from the positive one). As clear from Figure 3.5 that infinite number of hyperplanes are possible. The SVM tries to find a classifier which maximizes the gap between data points on the boundaries. These data points are known as the support vectors.

### 3. VARIOUS MACHINE LEARNING METHODS

---

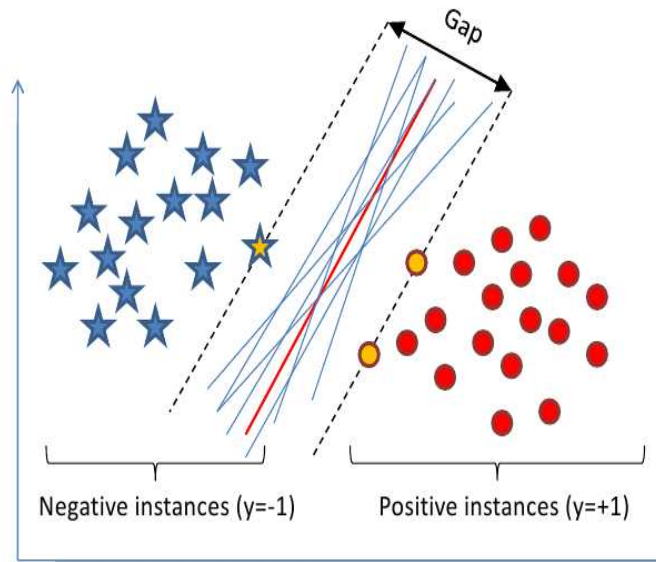


Figure 3.5: Statement of linear SVM.

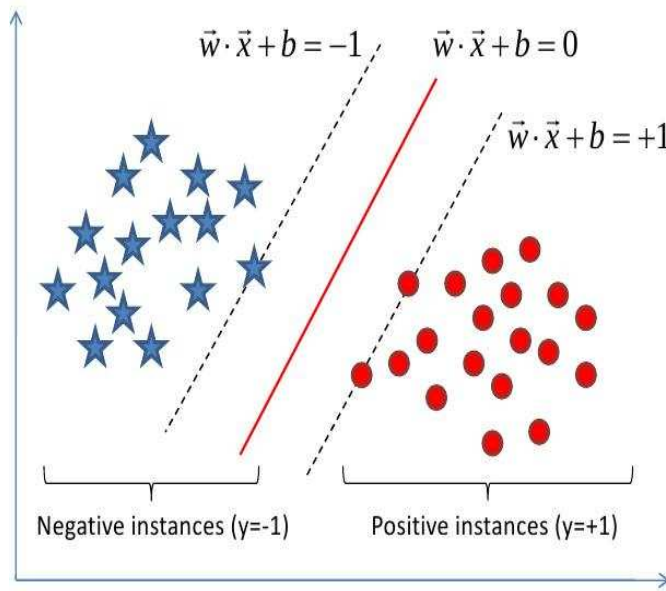


Figure 3.6: A maximal margin hyperplane with its support vectors in linear SVM.

#### 3.3.5.3 Optimal hyperplane for linear SVM

We know that the equation of parallel hyperplanes represented by red line is

$$\vec{w} \cdot \vec{x} + b = 0$$

### 3.3. Different classification methods

---

Therefore, the equation of parallel hyperplane between negative and positive instances are

$$\vec{w} \cdot \vec{x} + b = 1 \quad (y_i = 1)$$

$$\vec{w} \cdot \vec{x} + b = -1 \quad (y_i = -1)$$

Above equations can be written as

$$\vec{w} \cdot \vec{x} + b - 1 = 0$$

$$\vec{w} \cdot \vec{x} + b + 1 = 0$$

We know that the distance between two hyperplanes is  $\frac{|(b_1 - b_2)|}{\|\vec{w}\|}$ , therefore, the distance D between two hyperplanes is given by

$$D = \frac{2}{\|\vec{w}\|}$$

It is clear from Figure 3.6 that the hyperplane guaranteeing the best performance is the one where the maximal margin of separation between the two classes is  $\frac{2}{\|\vec{w}\|}$ . Such hyperplane is known as the optimal hyperplane. Since we want to maximize the gap, i.e. margin, equivalently we would like to minimize  $\|\vec{w}\|$ . It directs to following constrained

### 3. VARIOUS MACHINE LEARNING METHODS

---

optimization problem:

$$\underset{(\vec{w}, b)}{\text{minimize}} \quad \frac{1}{2} \| \vec{w} \|^2 \quad (3.5)$$

subject to

$$y_i(\vec{w} \cdot \vec{x} + b) \geq 1 \quad i = 1, 2, 3 \dots \quad (3.6)$$

This formulation ensures that maximum margin classifier classifies each instance correctly because we assumed that data is linearly separable. Then for a given new instance  $\mathbf{x}$ , the classifier is  $f(\vec{x}) = \text{sign}(\vec{w} \cdot \vec{x} + b)$ .

#### 3.3.5.4 Dual formulation

The SVM is a binary classifier such that for a given set  $X$  of training samples  $\mathbf{x}_i \in \mathbb{R}^d$  and the corresponding labels  $y_i \in \{-1, 1\}$ ,  $i = 1, \dots, N$ , it finds a maximum-margin hyperplane separating  $\mathbf{x}_i$  for which  $y_i = -1$  from  $\mathbf{x}_i$  for which  $y_i = 1$  [114].

In case of dual formalism, the  $\vec{w}$  is defined in terms of  $\alpha_i$ . It is defined as

$$\mathbf{w} = \sum_{i=1}^m y_i \alpha_i \mathbf{x}_i, \quad (3.7)$$

in which  $\alpha_i \in \mathbb{R}$ ,  $i = 1, \dots, N$ , are obtained during optimization. Then, the decision function of a test sample  $\mathbf{x}$  is

$$f(\mathbf{x}) = (\mathbf{w} \cdot \mathbf{x} + b) = \left( \sum_{i=1}^m y_i \alpha_i \mathbf{x}_i \cdot \mathbf{x} + b \right), \quad (3.8)$$

here  $\mathbf{b}$  is the bias term, also obtained during optimization. For non-support vectors  $\mathbf{x}_i$ ,  $\alpha_i = 0$ .

### 3.3. Different classification methods

The linear decision plane is too much limited in its application because of heterogeneous nature of experimental data. Here the non linear classifiers based on kernel feature play a vital role. The kernel functions provide a simple bridge from linearity to non-linearity. The kernel function (mathematical function) maps the data into higher dimensional hyperplane (feature space), where each coordinate corresponds to one feature of the data items. In this way, the data is transformed into a set of points in a Euclidean space, leading to the classification.

#### 3.3.5.5 Non linear SVM

In [113], the authors proposed a modification in SVM for the cases in which the training data are not linearly separated in the feature space. When such a decision surface, i.e. a hyperplane does not exist to separate two classes, as shown in the left panel of Figure 3.7 then data is mapped into a higher dimensional space where a separating

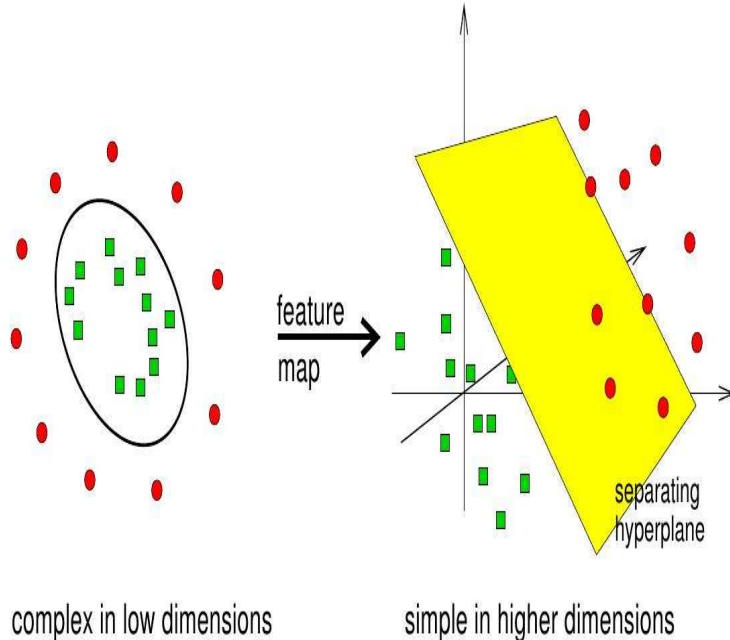


Figure 3.7: projection of data into higher dimensional space

### 3. VARIOUS MACHINE LEARNING METHODS

---

hyperplane is available (right panel of Figure 3.7). This projection of data is carried out by a mathematical operation, technically known as "*Kernel operation*". Instead of linearly separating the samples in the original space  $\mathbf{x}$  of the training samples in  $X$ , the samples are projected onto a higher dimensional space in which they are linearly separated. One advantage of this method is that in addition to separating non-linear data, the optimization problem of the SVM remains almost the same: instead of calculating the inner product  $\vec{\mathbf{x}}_i \cdot \vec{\mathbf{x}}$ , it uses a kernel  $K(\vec{\mathbf{x}}_i, \vec{\mathbf{x}})$  that is equivalent to the inner product  $\phi(\vec{\mathbf{x}}_i) \phi(\vec{\mathbf{x}})$  in a higher dimensional space  $\phi$ . When using the kernel trick, we do not need to know the  $\phi$  space explicitly.

Using kernels, the decision function of a test sample  $\vec{\mathbf{x}}$  becomes

$$f(\mathbf{x}) = \left( \sum_{i=1}^m y_i \alpha_i K(\vec{\mathbf{x}}_i, \vec{\mathbf{x}}) + b \right). \quad (3.9)$$

- The most used kernel for SVM is the RBF kernel [115], defined as follows.

$$K(\vec{\mathbf{x}}_i, \vec{\mathbf{x}}) = e^{-\gamma \|\vec{\mathbf{x}} - \vec{\mathbf{x}}_i\|^2}. \quad (3.10)$$

Other useful kernels are

- Gaussian Kernel

$$K(\mathbf{x}_i, \mathbf{x}_j) = e^{\frac{-\|\mathbf{x}_i - \mathbf{x}_j\|^2}{2\sigma^2}} \quad (3.11)$$

- Polynomial

$$K(\mathbf{x}_i, \mathbf{x}_j) = (\mathbf{x}_i \cdot \mathbf{x}_j)^p \quad (3.12)$$

### 3.3. Different classification methods

---

- Sigmoid Kernel (used in neural net)

$$K(\mathbf{x}_i, \mathbf{x}_j) = \tanh(\kappa \mathbf{x}_i \mathbf{x}_j - \delta)^p \quad (3.13)$$

In the present work, the Radial Basis Function (RBF) and Polynomial kernels are used. A polynomial of degree 3 with type 2 classification was employed. The parameter gamma = 0.2 and  $\nu = 0.5$  were considered. For the Radial basis function, these parameters were 0.2 and 0.35 respectively.

#### 3.3.6 Random Forest Method

Random Forest (RF) is a flexible multivariate selection method. The algorithm for Random Forest was developed by Leo Breiman and Adele Cutler [102]. The Random Forests are a combination of tree predictors such that each tree depends on the values of a random vector sampled independently and with the same distribution for all trees in the Forest [116]. The classification tree, also known as the “Decision tree” are machine learning prediction models constructed by recursively partitioning the data set. Each binary recursive partitioning splits the data sets into different branches. The tree construction starts from the root node (the entire dataset) and ends at the leaf. Every leaf node is assigned with a class. The Random Forest method combines the concept of ‘bagging’ [117] and ‘Random Split Selection’ [118].

##### 3.3.6.1 Bagging

The *Random Forest* builds on bagging [117] technique where bagging stands for “Bootstrapping” and “Aggregating” techniques. The basic idea of bagging is to use bootstrap

### 3. VARIOUS MACHINE LEARNING METHODS

---

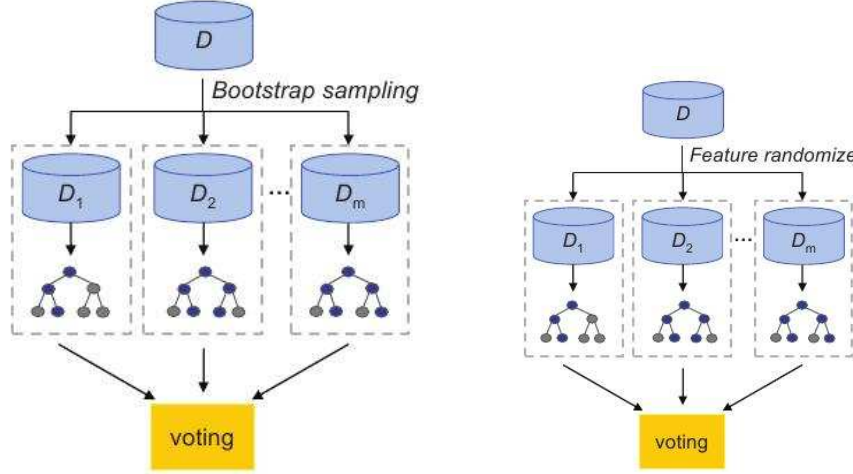


Figure 3.8: Bootstrap sampling

re-sampling to generate multiple versions of a predictor and combining them to make the classification. Bootstrapping is based on random sampling with replacement. It ensures that the probability of selecting an event in the sampling (with replacement) procedure is constantly  $\frac{1}{n}$ . Therefore, the probability of not selecting an event is equal to  $(1 - \frac{1}{n})$ . If the selection process is repeated  $n$  times, where  $n$  is very large, the probability of not selecting an event will be  $\sim \frac{1}{3}$ . Therefore, only  $\frac{2}{3}$ , i.e. ( $\sim 70\%$ ) events are taken for each bootstrap sample.

#### 3.3.6.2 Random Split Selection

In addition to bagging, *Random Forest* also employs “Random Split Selection” [118]. At each node of the decision tree,  $m$  variables are selected at random out of the  $M$  input vectors and the best split is selected out of these  $m$ . Typically about square root ( $M = m$ ) number of predictors are selected. The Random forest algorithm can be summarized by Figure 3.9

Two sources of randomness, namely random inputs and random features, make *Random*

### 3.3. Different classification methods

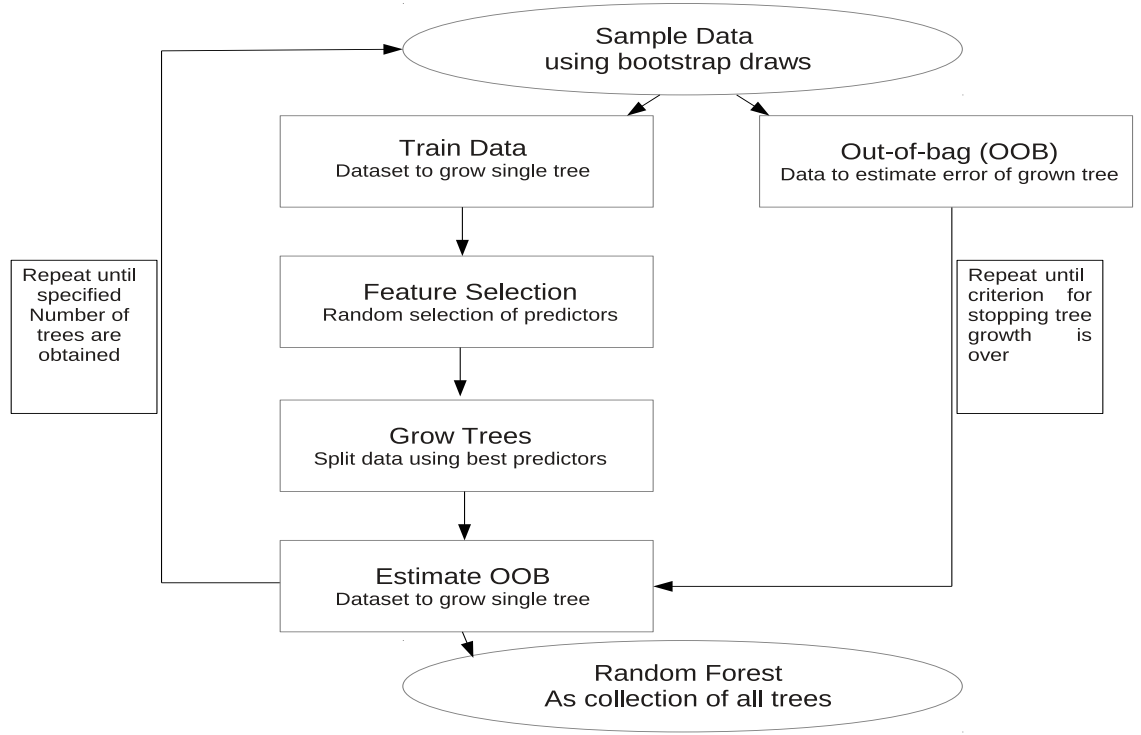


Figure 3.9: Random Forest algorithm

*Forests* accurate classifiers. In order to measure the classification power (separation ability) of a parameter and to optimize the cut value, the Gini index is used which measures the inequality of two distributions. In the case of two classes ( $\gamma$  and hadrons), Gini index can be referred to as Binomial variance of the sample scaled to interval [0,1] [100]. For a node splitting, if  $N_\gamma$  and  $N_h$  is the number of  $\gamma$  and hadrons respectively ( $N = N_\gamma + N_h$ ) then the Gini index is defined as

$$Q_{Gini} = \frac{4}{N} \cdot \sigma_{binomial}^2 = 4 \frac{N_\gamma}{N} \frac{N_h}{N} \quad (3.14)$$

The classification is achieved by splitting each node into successive nodes. The splitting of mother node to daughter nodes is carried out by applying a cut value chosen from

### 3. VARIOUS MACHINE LEARNING METHODS

---

the available attribute/parameters. This cut value is chosen on the basis of Gini index defined above. The splitting process stops when the number of events falls below a user defined value, say “*stop the splitting process if the events in the node falls below say, 10 events*”. The node at which the splitting process stops is known as the terminal node. Let us say that each terminal node is assigned a class label  $k$  where  $k = 0$  represents the  $\gamma$  event and  $k = 1$  represents hadron event. Suppose the terminal node contains a mixture of events of different types/classes then one can calculate a mean value by taking into account the class populations  $N_h$  of hadrons and  $N_\gamma$  of gammas.

$$k = \frac{N_h}{(N_h + N_\gamma)} \quad (3.15)$$

A typical classification tree is shown in Figure 3.10. We have taken the simulation data after characterizing the Cherenkov images. The image contains a mixture of two classes, viz.  $\gamma$  and hadron. In the shown tree, we have used various Hillas parameters. The cut values like **asym**  $\geq 0.53$ ; **length**  $\geq 0.18$ ,  $\leq 0.41 \dots$  is chosen on the basis of Gini index. The label **1** represents one class, (in our case  $\gamma$ ) and label **2** represents the other class (hadron in our case). After calculating the value of **k** for all the trees, the mean classification is obtained by taking the average of **k** over all the trees. This *mean classification* is known as the *hadronness*. All the events are now classified on the basis of hadronness. If its value is closer to 1, we classify the event as hadron like event and if its values is closer to 0, the event is classified as  $\gamma$  like event.

Breiman [116] estimated the error rate on out-of-bag data (i.e. oob data). Each tree is constructed on a different bootstrap sample. Since in each bootstrap training set about

### 3.3. Different classification methods

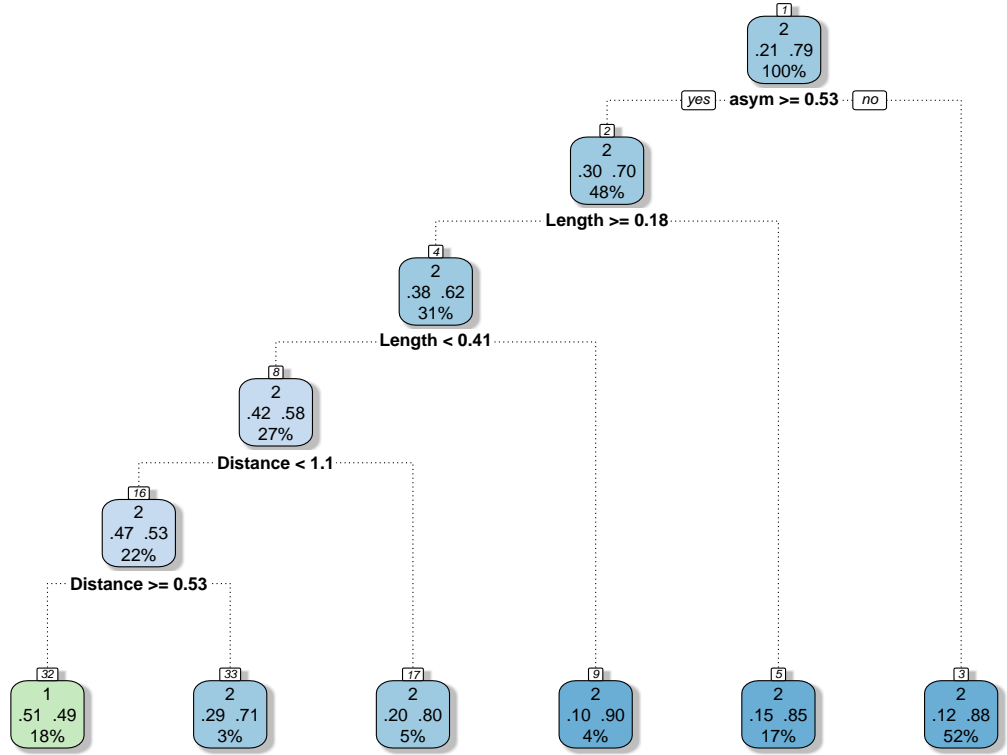


Figure 3.10: Classification tree

one third of the instances are left out (i.e. out-of-bag), we can estimate the test set classification error by putting each case left out of the construction of the  $t^{th}$  tree down the  $t^{th}$  tree. The oob error estimate is the misclassification proportion on oob data. Figure 3.11 shows the estimated OOB error rate. The number of trees needed by the Random Forest to utilize its full potential must be chosen large enough in such a way that the convergence of error  $\sigma$  takes place. Its value is given by [93]

$$\sigma(n_{tree}) = \sqrt{\frac{\sum_{i=1}^{n_{sample}} (h_i^{est}(n_{tree}) - h_i^{true})^2}{n_{sample}}} \quad (3.16)$$

$\sigma(n_{tree})$  is the rms error of the estimated hadronness.  $h_i^{est}(n_{tree})$  denotes the estimated

### 3. VARIOUS MACHINE LEARNING METHODS

---

hadronness (which depends on the number  $n_{tree}$  of combined trees) and  $h_i^{true}$  is the true hadronness of event  $i$  in the sample, which contains  $n_{sample}$  events in total. The convergence process is shown in Figure 3.11 for the training of RF on an MC gamma and MC hadron sample taken from the section 3.2. It is clear that 100 trees are sufficient for error convergence.

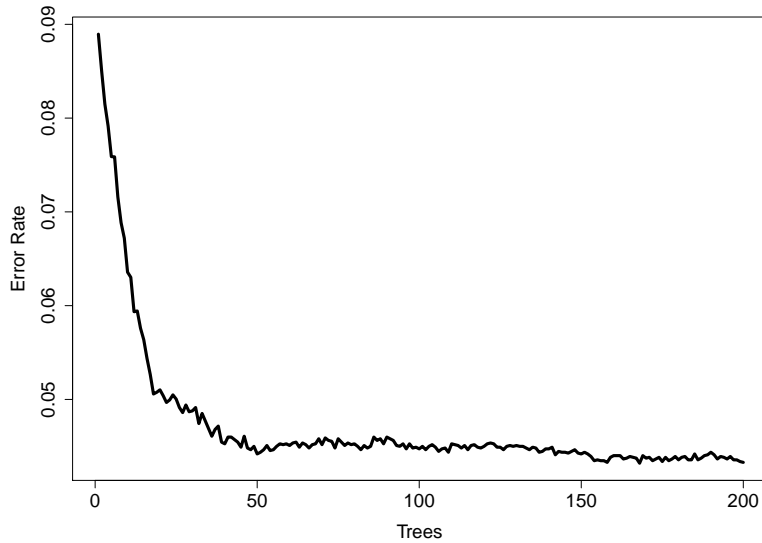


Figure 3.11: The Error ( $\sqrt{\sigma^2}$ =rms) of estimated hadronness as function of the number of trees.

#### Random Forest Fundamentals

The mathematical foundation of Random Forest method is described in [116]. Some of the useful variables to predict the strength of classification using this method are described below:

#### Definition

A Random Forest is a classifier consisting of a collection of tree structured classifiers  $h(x, \Theta_k)$ ,  $k=1, \dots$  where the  $\Theta_k$  are independent identically distributed random vectors

### **3.3. Different classification methods**

---

and each tree casts a unit vote for the most popular class at input  $\mathbf{x}$ .

#### **Accuracy of Random Forest**

The accuracy of Random Forest is characterized by the **margin function**. The margin function measures the extent to which the average number of votes at  $\mathbf{X}, Y$  for the right class exceeds the average vote for any other class.

If  $h_k(X)$  are an ensemble of classifiers and with the training set drawn at random from the distribution of the random vector  $Y$ , then the **margin function** is defined as

$$mg(\mathbf{X}, Y) = av_k I(h_k(\mathbf{X}) = Y) \max_j \neq Y av_k I(h_k(\mathbf{X}) = j) \quad (3.17)$$

$I$  is the indicator function. The larger the margin, the more confidence in the classification.

#### **Random Forest Prediction**

The predictions of the Random Forest are taken to be the average of the predictions of the trees:

$$\text{Random Forest Prediction} = \frac{1}{K} \sum_{K=1}^K K^{\text{th}} \text{Tree Response} \quad (3.18)$$

where  $K$  = total number of trees

#### **Generalization error**

### 3. VARIOUS MACHINE LEARNING METHODS

---

The generalization error is defined as

$$PE = P_{Y,X}(mg(\mathbf{X}, Y) < 0) \quad (3.19)$$

where the subscripts X,Y indicate that the probability is over the X,Y space. The generalization error is also known as the classification error.

In Random Forests,  $h_k(\mathbf{X}) = h(\mathbf{X}, \Theta_k)$ . For a large number of trees, all the sequences  $\Theta_k$  converges.

The strength and Correlation of Random Forest is estimated by the generalization error. For random forest, an upper bound can be derived for the generalization error in terms of two parameters that are measures of how accurate the individual classifiers are and of the dependence between them. The interplay between these two gives the foundation for understanding the workings of random forest.

The expectation value of the margin is called strength. This strength is defined as

$$s = E_{\mathbf{X},Y} mg(\mathbf{X}, Y). \quad (3.20)$$

An upper bound for the generalization error is given by

$$PE \leq \rho \frac{(1 - s^2)}{s^2} \quad (3.21)$$

where  $\rho$  denotes the mean correlation between the trees and  $s$  is the strength of the set of classifiers  $h(\mathbf{x}, \theta)$ . To improve the accuracy, the randomness injected in combining the

### **3.4. Comparison of Classification methods**

---

trees has to minimize the correlation while maintaining strength.

In this study, the original Random Forest code in fortran [102] was employed and a total of 100 trees were generated . The variable defined in the above code as  $mtry = 2/3$  was taken. Almost similar results were obtained in each case. The resultant output of this code was compared with the implementation of Random Forest in the statistical package R [119]. It is worth mentioning here that the Fortran code encounter some memory issues when the number of training/test events crosses a certain threshold. However, this limitation was not encountered in the Random Forest implementation in R.

## **3.4 Comparison of Classification methods**

The above listed methods were employed to classify the events into  $\gamma$  and hadron classes. A total of 7938 events of each type were considered as described in the earlier section. Around 70% of the events were used for training all the machine learning methods and rest of the data was used as a test sample. Same training and test data was used by all the methods to have a one to one correspondence in the results. After training, the test sample was passed through the trained classifier and prediction of  $\gamma$  and hadron class were made. Our aim is to identify the best classifier. The accuracy of prediction rules can be evaluated by the ROC (Receiver Operator Characteristic) curves. These curves were first time applied to distinguish enemy planes (true signal) from the noise signal (false signal). The ROC plots are graphical technique [120] to compare the classifiers and visualize their performance. These curves are applied virtually in the field of decision making, like in the signal detection theory ( [121] and more recently in the medical field [122].

### 3. VARIOUS MACHINE LEARNING METHODS

---

#### 3.4.1 Evaluation

We are attending a binary classification problem where the two cases are  $\gamma$  and hadrons.

For a binary classification problem, a total of 4 possible outcomes are possible. The two outcomes are related to the correct classification for the two classes and two for incorrect classification. The True Positive (TP) class denotes the correct classification of class  $\gamma$  and True Negative (TN) class represents the correct classification of class hadron. The False Negative (FN) class reflects the class  $\gamma$  incorrectly classified as class hadron and False Positive (FP) class is the incorrect classification of class hadron as class  $\gamma$ . These four outcomes can be used to estimate the level of misclassification. Each classifier's performance was evaluated by generating a confusion matrix which is a  $2 \times 2$  matrix representing all the above 4 possible outcomes. Table 3.1 shows the generic table for a two class problem.

		True Class	
		$\gamma$	hadron
Predicted Class	$\gamma$	TP	FP
	hadron	FN	TN

Table 3.1: Confusion matrix

The four possible outcomes are used to generate the ROC plot. The ROC plot is a diagnostics tool for binary classification as a function of a class discriminating cut value, known as threshold. This matrix, known as the *confusion – matrix*, evaluates the fraction of correctly/incorrectly classified events. From the confusion matrix, the class  $\gamma$

### 3.4. Comparison of Classification methods

---

acceptance represented as True positive rate (TPR) was estimated by defining it as  $TPR = \frac{TP}{TP+FN}$  [120]. The class hadron acceptance, represented as False Positive Rate (FPR) was estimated by defining it as  $FPR = \frac{FP}{FP+TN}$ . It is to be noted that we are not generating the ROC curves in the strict sense. The ROC curves, by definition lies between (0, 0) and (1, 1). In the present study, the hadron acceptance was plotted in logarithmic axis for better visualization. Therefore, the ROC plots in this study differs from the conventional ROC plots.

In order to find the best classifier, the decision boundary for prediction was varied. Each decision boundary generated one point in  $\gamma$ -acceptance (tpr) and hadron acceptance (fpr) curve. A *tpr* Vs *fpr* plot is referred to as a decision-plot. The decision-plot was generated for each classifier. If the decision-plot inclines towards the left side, it indicates greater accuracy, i.e. a higher ratio of true positive to false positive. In order to compare various classifiers, the decision plot is generated for all the machine learning methods. The top most plot in the decision-plot turns out to be the best classifier because for the same hadron acceptance, upper plot gives the highest  $\gamma$ -acceptance.

The decision plot is the qualifying metric to select the most suitable classification method. In addition to the decision-plot, the difference among various classifiers was also quantified by estimating the signal strength at a representative  $\gamma$ -acceptance value. The decision about the best classifier was arrived by using the “tpr” – “fpr” decision-plot. The quantifying metric is designated as “signal strength”, defined as  $\sigma = \frac{S}{\sqrt{(2B+S)}}$  where  $S = \epsilon_\gamma N_S$  and  $B = \epsilon_p N_B$  [123] are the signal and background events respectively. Since the conventional dynamic Supercuts method estimated the  $\gamma$ -acceptance at 57.4%, the

### 3. VARIOUS MACHINE LEARNING METHODS

---

hadron acceptance from each classifier was derived from the decision-plot at this value.

The signal strength was estimated by taking  $N_B = 10,000$  and  $N_S = 500$  [92]. The

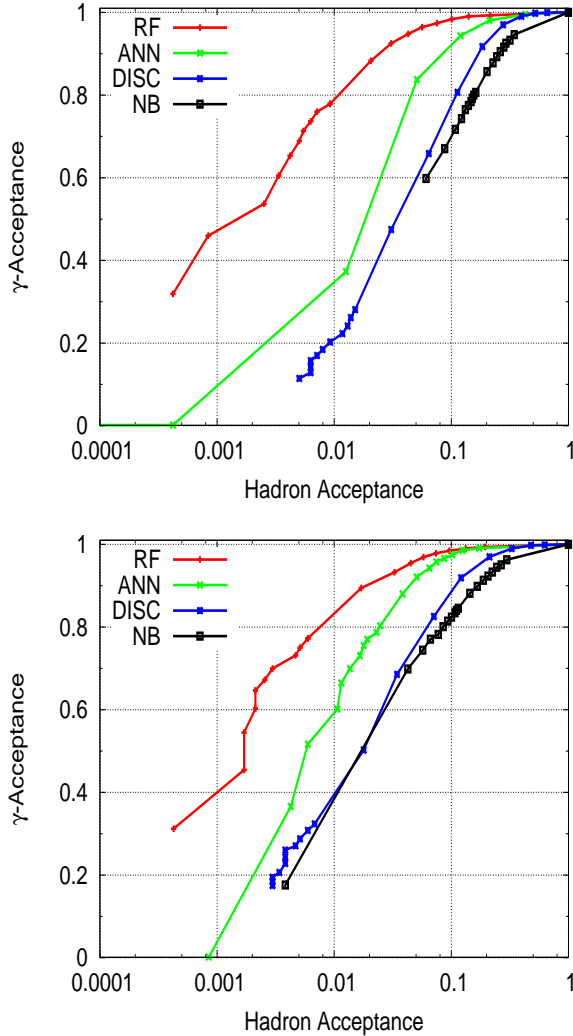


Figure 3.12: Signal vs background acceptance. The top panel is the classification result by using the 5 attributes/parameters. The bottom panel represents it for 7 attributes/parameters

decision plot was generated for two sets of image parameters. As mentioned earlier, two sets were considered to evaluate the classification strength as a function of the number of image parameters. The decision-plots for these two cases are shown in Figure 3.16. The comparison shows that Random Forest method yields better classification strength. This

### 3.4. Comparison of Classification methods

difference in the classification is albeit small, of the order of  $\sim 10\%$  ( $\gamma$ -ray acceptance) for a given hadron acceptance range. This difference results because of more number of image parameters and guides us to choose seven image parameters for better classification. The decision-plot for rest of the methods reflect the same tendency. Any classifier yielding the maximum gamma acceptance for a given hadron acceptance decides the superiority of the classifier. Figure 3.13 shows the  $\gamma$ -acceptance as a function of projected hadron-rejection for 4 representative projected hadron-rejection values, viz 90%, 99.3%, 99.6%, 99.9%. For

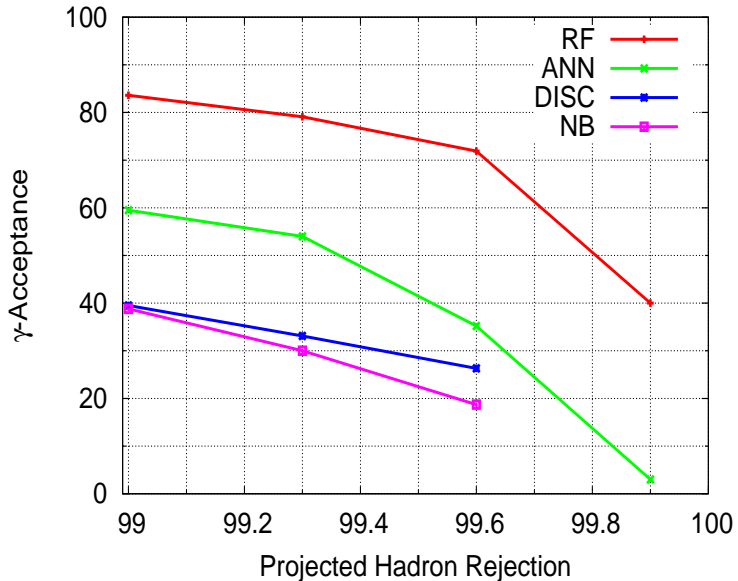


Figure 3.13: Gamma acceptance as a function of projected hadron rejection

a hadron rejection of 99.9%, the RF method yields  $\sim 40\%$   $\gamma$ - acceptance. Compared to it, the ANN method gets  $\sim 3\%$   $\gamma$ -acceptance. Rest of the two classifiers fair quite poorly. In addition to estimating the signal strength, the misclassification rate was also estimated by using the confusion matrix. The misclassification rate and the signal strength are shown in Table 3.2

The positive effect of more number of parameters is better visible by the quantification of

### 3. VARIOUS MACHINE LEARNING METHODS

---

<b>Classification method</b>	Misclassification Rate %	Signal Strength
	$R_5/R_7$	$\sigma_5 / \sigma_7$
Random Forest	5.44 / 4.43	15.46 / 15.73
Automated Neural Network	7.40 / 5.82	9.8 / 13.30
Standard Discriminant Analysis	12.11 / 10.08	8.10 / 10.37
Naive Bayes Classifiers	20.57 / 14.00	7.8 / 10.32
Support Vector Machine		
i) with RBF kernal	9.18 /16.08	na
ii)with polynomial Kernel	10.19 /16.12	na

Table 3.2: Misclassification rate and signal strength with two sets (7 and 5)image parameters

misclassification rate as well as the signal strength. It is to be noted that the entries for Support Vector Machine in Table 3.2 are absent, only the misclassification rate is given. It is to be noted that the ANN, DISC, NB methods produce the probabilistic output but in the case of SVM, the STATISTICA package gives the hard predictions, and hence the generation confusion matrix is not possible. Table 3.2 for SVM with both the kernels (RBF and polynomial) suggest that for the given dataset, gamma and hadron acceptance will remain lower compared to that of RF and ANN method.

### **3.4. Comparison of Classification methods**

---

The strength of ROC curves is generally exploited by comparing various classifiers and the suitable classifier is selected. The classifier is selected on the basis of its position in the ROC space. However, selecting the classifier on this basis is over simplistic. The Precision-Recall (PR) curves are more fundamental than the ROC plots. According to the theorem [124], “For a fixed number of positive and negative examples, one curve dominates a second curve in ROC space if and only if the first dominates the second in Precision-Recall space. The precision is defined as  $\text{Precision} = \frac{TP}{TP+FP}$ . The Precision essentially reflects the fraction of examples classified as positive which are truly positive, i.e., predicted positives (here class  $\gamma$ ). The Recall is the True Positive Rate. In the PR space, the recall is plotted on the x-axis and the Precision is plotted on the y-axis. The classifier attaining the top position in the PR space and hence in the ROC space (as per the above mentioned theorem) is declared as the best classifier. Therefore, in order to conclude the best classifier, it is important to evaluate the classifier performance in PR space. The Precision-Recall plot is generated for both the sets of image parameters and is shown in Figure 3.14.

The Random Forest method retains the top most position in the ROC curve as well as in the PR-space compared to rest of the classifiers. Therefore it is concluded that the Random Forest method is the best classifier. It is to be noted that the superiority of PR curve over ROC plots is more pronounced when there is a skew in the class distribution in a dataset.

### 3. VARIOUS MACHINE LEARNING METHODS

---

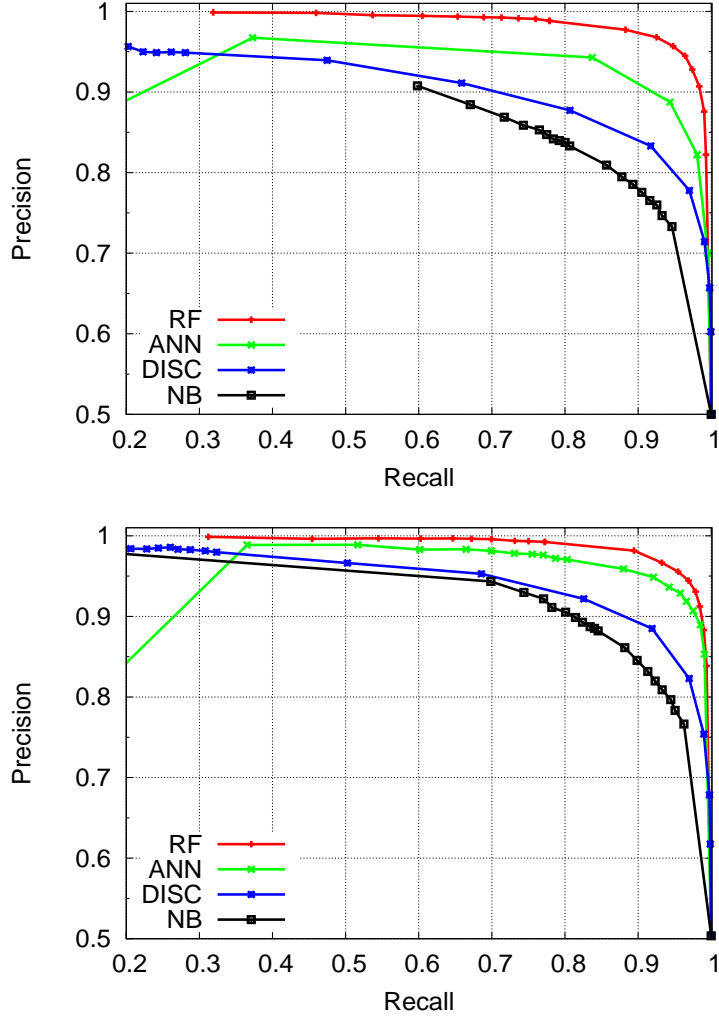


Figure 3.14: Precision Recall curves. The top panel represents the PR curve for the 5 attributes/parameters. The bottom panel represents it for 7 attributes/parameters

#### 3.4.2 Conclusion

Five different machine learning methods were evaluated and compared to decide about the suitability of these methods for  $\gamma$ -hadron segregation. Given the position of all the methods in the ROC space, PR-space and the misclassification rate for the given dataset, the trend reflects the superiority of Random Forest and the Artificial Neural Network compared to rest of the methods, i.e. Standard Discriminant method, Naive Bayes Classifier

### **3.4. Comparison of Classification methods**

---

and Support Vector Machine. The signal strength was estimated by using the confusion matrix at a representative value of  $\gamma$ -acceptance of 0.574. This value was chosen because the conventional dynamic Supercuts method yields the same  $\gamma$ -acceptance. This method yields a signal strength of  $\sigma_{0.574} = 12.92$ , whereas the signal strength are 15.73 and 13.30 from the Random Forest method and the Artificial Neural Network method respectively. It is clear that these two methods yield better results compared to the conventional dynamic Supercuts method. For the given dataset, Random Forest method gives almost 20% improvement in the signal strength over the Artificial Neural Network method. Similar trend is repeated in the estimation of misclassification rate. It is difficult to make a generalized statement about the superiority of Random Forest methods over any other methods, However, the dominance of Random Forest method in ROC plot as well as in the Precision-Recall space indicates that for the given dataset, the Random Forest method is the best classifier. In addition to above classifying metric, the Random Forest method has additional advantage in terms of computational time over the perceptron based method like Artificial Neural Network. As the number of perceptrons increase, it becomes computationally very expensive. Apart from it, unlike Artificial Neural Network method acts as a black box whereas the Random Forest method is quite easy to understand. Random Forest method demands very little processing capabilities. Random Forest method takes care of parameters with little or no separation power whereas the performance of Artificial Neural Network performance is severely affected by the inclusion of such parameters. Our results are in sync with the earlier study ([92] carried out by using the simulated data for the MAGIC telescope.

## 3.5 Other machine learning methods

In addition to the five machine learning methods, various machine learning methods from the TMVA package ([125]) were tested and their resultant decision-plot is presented. Various machine learning methods are as follows: Boosting Decision Tree (BDT), BDT with gradient boost (BDTG), BDT with decorrelation (BDTD) + Adaptive Boost, TMlpANN (ROOT's own ANN), Fisher Boost (Linear discriminant with Boosting) and Probability Density Estimator Range-Search (PDERS). For all these methods, the default settings given by the TMVA developers were used. It is clear from the decision-plot (Fig. 3.15) that the RF method outperforms all the other methods.

In the next section, we will validate the Random Forest method by using the Markarian (Mrk) 421 and Crab Nebula observation of 2005-2006 by the TACTIC telescope.

## 3.6 Random Forest method Application on Mrk421 observation

Mrk421 in the high state was observed in 2005 – 2006 by various Imaging Atmospheric Cherenkov Telescope (IACTs). MAGIC telescope observed this source from April 22 to April 30, 2006 [126]. Whipple telescope [127] carried out the observation in April and June 2006. This source was also observed by TACTIC telescope from 27 December 2005 - 30 April 2006 for a total of  $\sim 201$  hrs [89]. Previous analysis of this data led to a detection of flaring activity from the source at Energy  $> 1$  TeV. A spell of  $\sim 97$  hrs of

### 3.6. Random Forest method Application on Mrk421 observation

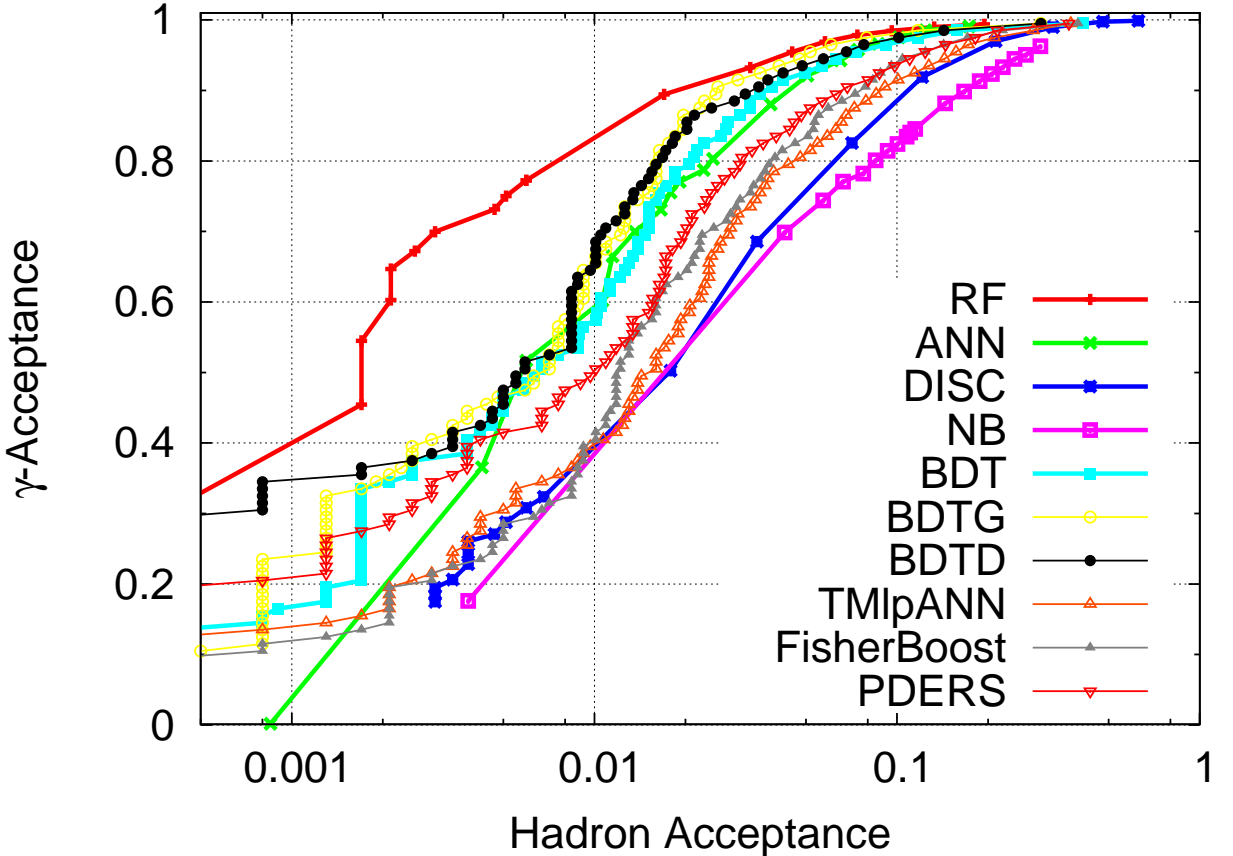


Figure 3.15: The decision-plot of various machine learning methods

this data revealed strong detection of gamma-ray signal with daily flux of  $> 1$  Crab unit on several days. The analysis was carried out by the Dynamic Supercuts method. Here we re-analyze the entire dataset using the Random Forest method.

#### 3.6.1 Mrk 421 observation

TACTIC telescope observed Mrk 421 for a total of  $\sim 201$  hrs between December 07, 2005 - April 30, 2006. The source was observed for six different lunation labelled as Spell I - Spell VI. The observation was restricted to a zenith angle  $\leq 45^\circ$

### 3. VARIOUS MACHINE LEARNING METHODS

---

#### 3.6.1.1 Database used for Mrk421 analysis

A Monte Carlo simulated database was generated by using the CORSIKA air shower code [97] with the Cherenkov option. The simulations were carried out for the TACTIC telescope [98] at the Mount Abu observatory at an altitude of  $\sim 1300$ m. A total of 74000  $\gamma$ -ray events in the energy range from 1-20 TeV were selected according to the differential spectral index 2.6. These events were generated at five zenith angles:  $5^0, 15^0, 25^0, 35^0$  and  $45^0$ . The Cherenkov photons triggered the telescope after encountering the wavelength dependent photon absorption, reflection coefficient of the mirror facets, light cone used in the camera and the quantum efficiency of photomultiplier tubes. All the triggered events underwent the usual image cleaning procedure [99] to eliminate the background noise. In order to have a robust and well contained image inside the camera, pre-filtering cuts of size  $\geq 50$  photoelectrons and  $0.4^0 \leq distance \leq 1.4^0$  were applied. It yielded a total of 60000 events for  $\gamma$ -rays.

However, it is generally not advisable to use Monte Carlo hadrons while using the observation data because the hadronic showers have large fluctuations. Moreover, the generation of hadron showers is much more time consuming owing to their very small trigger probability. In the presence of ON or OFF source observational data, there is no need to use the simulated protons, the cosmic ray protons can be used from the observational data. In the present study, the actual events recorded by the TACTIC telescope have been used in place of simulated protons. A database of  $\sim 17000$  simulated proton events were generated using CORSIKA. Also same number of events were extracted randomly from ON source observation where all the events with  $\alpha > 27^0$  were treated as

### 3.6. Random Forest method Application on Mrk421 observation

cosmic ray proton events. Figure 3.16 shows the comparison of various image parameters from simulated and observational protons extracted from the ON source observation. It

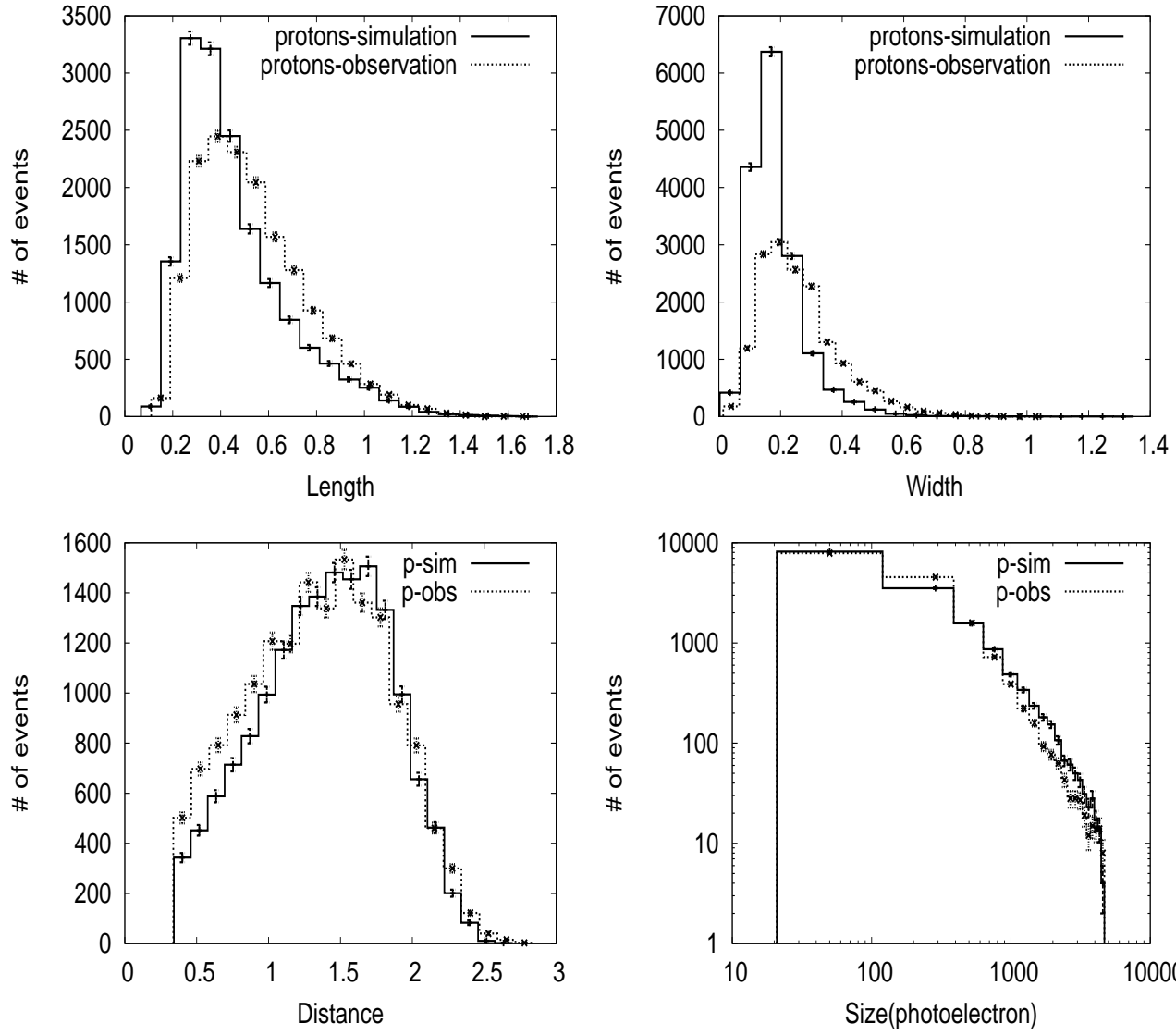


Figure 3.16: Comparison of various image parameters like length, width, distance as well as size (photoelectron) from Monte Carlo simulation protons and real cosmic ray proton events detected by the TACTIC telescope. We have used 1 photoelectron = 6.3 counts

is evident from this figure that the simulated hadrons mimic the observational hadrons quite closely. Therefore, simulated protons can safely be replaced by the observational

### 3. VARIOUS MACHINE LEARNING METHODS

---

events acquired by the TACTIC telescope.

#### 3.6.1.2 Image parameters for classification

The procedure to use of zenith angle and size for classification has been described in the Section 3.2.1. Before the classification, we first compartmentalize the continuous zenith angle distribution of observed events by replacing  $\sim 10^0$  bin of zenith angle with a single zenith angle value. Accordingly in the present work, we approximate all the observational zenith angle between  $0 - 10^0$  by  $5^0$  zenith angle,  $10 - 20^0$  by  $15^0$  etc. After taking into account all such factors, Hillas parameters used to characterize the Cherenkov events namely zenith angle, length, width, distance, size (photoelectrons) and Frac2 have been computed. For the classification purpose, alpha parameter was not considered even though alpha is a very powerful parameter as it carries the signature of the progenitor ( $\gamma$  or proton). If the alpha parameter is used in the classification then the hadronic background can not be evaluated.

#### 3.6.1.3 $\gamma$ -hadron classification methods

The problem of  $\gamma$ /hadron segregation is formulated as a two class problem: viz  $\gamma$  represents one class and the hadron is the second class. Here we will apply the Random Forest method for  $\gamma$ -hadron classification. As mentioned earlier [89], the previous analysis of this data was carried out by using the Dynamic Supercuts method, described in Section 3.3.1. By employing this method, the optimum number of cut parameters and their values were estimated by numerically maximizing the so called Quality factor Q [105], defined as

$$Q = \frac{\epsilon_\gamma}{\sqrt{(\epsilon_P)}} \quad (3.22)$$

### 3.6. Random Forest method Application on Mrk421 observation

---

Here  $\epsilon_\gamma$  and  $\epsilon_P$  are  $\gamma$  and hadron acceptances respectively. After the numerical maximization of the quality factor, the set of image parameters are shown in Table 3.3.

Parameter	Cut Values
LENGTH (L)	$0.11^\circ \leq L \leq (0.235 + 0.0265 \times \ln S)^\circ$
WIDTH (W)	$0.06^\circ \leq W \leq (0.085 + 0.0120 \times \ln S)^\circ$
DISTANCE (D)	$0.52^\circ \leq D \leq 1.27^\circ \cos^{0.88}\theta$ ; ( $\theta \equiv$ zenith ang.)
SIZE (S)	$S \geq 450d.c$ ; (6.5 digital counts $\equiv$ 1.0 pe )
ALPHA ( $\alpha$ )	$\alpha \leq 18^\circ$
FRAC2 (F2)	$F2 \geq 0.35$

Table 3.3: Dynamic Supercuts selection criteria [89]

#### 3.6.1.4 $\gamma$ -hadron segregation using the Random Forest method

A total of 60,000  $\gamma$ -ray events resulted after applying the precuts defined in the earlier section. It was demonstrated (Figure 3.16) that the events extracted from ON Source observation beyond  $\alpha \geq 27^\circ$  matched well with that of simulated proton events. In order to have a balanced dataset for  $\gamma$  and hadrons, we extracted a total of 60,000 events from the ON source observations available from Mrk 421 and Crab Nebula observations carried out in 2005 – 06. A total of 30,000 events each from Mrk 421 and Crab Nebula observations were extracted respectively. For the present study, the zenith angle was restricted to  $45^\circ$ . A total of 70% events from  $\gamma$  and hadrons were used to train the Random forest and the remaining 30% events were used as a test sample. The frequency distribution of

### 3. VARIOUS MACHINE LEARNING METHODS

---

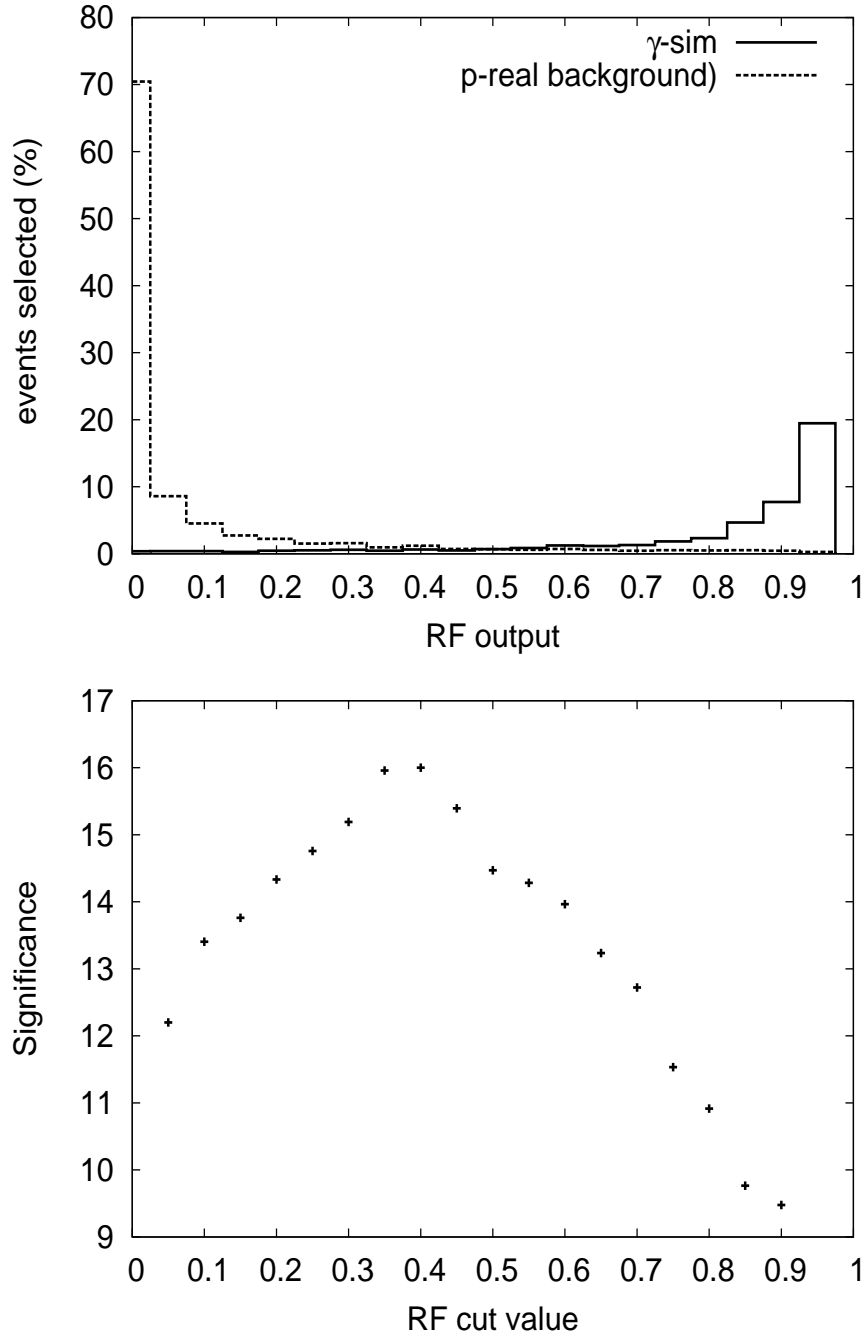


Figure 3.17: The top panel shows the simulated  $\gamma$  and observational protons for the estimation of optimum cut value of the Random Forest output. A total of 34120 events for simulated  $\gamma$  and actual background events were employed as a test sample. The bottom panel shows the significance as a function of Random Forest cut value.

### 3.6. Random Forest method Application on Mrk421 observation

---

predicted  $\gamma$  and hadron events from Random Forest for a test sample containing 17820  $\gamma$  and 16300 background events extracted from actual observation is shown in Figure 3.17. Any cut value above 0.25 will be able to remove most of the background events, leading to a better background rejection and hence will result in a better sensitivity. Quantitatively, the optimized cut value can be obtained either by maximizing Quality factor or by maximizing the signal significance. Figure 3.17 also shows the significance as a function of cut value. On the basis of this optimized significance, a cut value at 0.35 was chosen.

#### 3.6.2 Variable Importance

The Random forest method also helps in evaluating the most important parameters useful in the classification. Figure 3.18 shows the variable importance of various image parameters. It shows that the Frac2 parameter is the most important parameter for the classification. The parameter in the decreasing order of importance are width, length, zenith, dens and size. The observed variable importance is consistent with that obtained by similar systems in the TeV energy ranges.

#### 3.6.3 Alpha plot analysis for Mrk 421 using Random Forest

The recorded data with the telescope was subjected to standard image cleaning procedure [128] using picture and boundary threshold of  $6.5\sigma$  and  $3\sigma$ . Image cleaning procedure yields the pixels containing Cherenkov events only. All such events were processed to characterize the images using the Hillas parameters [26]. Typically  $\gamma$ -ray events have narrow elliptical shapes whereas hadronic events are more irregular. These differences in image shape are used for the segregation of  $\gamma$ / hadron events. The segregation of  $\gamma$ -ray like images from the sea of background hadron images by standard Dynamic Supercuts

### 3. VARIOUS MACHINE LEARNING METHODS

---

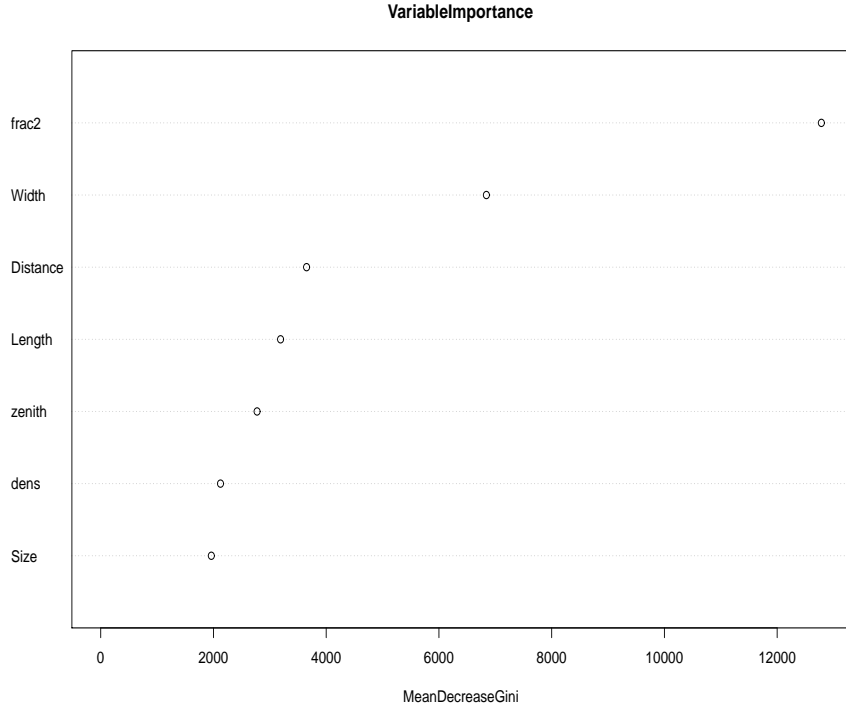


Figure 3.18: The variable importance estimated by the Random Forest method

method yields an excess of 1236  $\gamma$ -ray events with a statistical significance of  $11.49\sigma$  [89]. The frequency distribution of ALPHA parameter determines the excess number of  $\gamma$ -ray events. The background events were extracted from  $27^0 \leq \alpha \leq 81^0$  whereas  $\alpha \leq 18^0$  defines the region of signal events. Before employing the Random Forest for Mrk 421 data, we validated the method by analyzing the Crab Nebula data observed during the near same lunation (November 10, 2005 to January 30, 2006). The Random forest method yielded a total of  $(1080 \pm 113)$  events for a total of  $\sim 101.44$  h of observation. Same data was analyzed by restricting the zenith angle of observation to  $15^{\circ}$ - $45^{\circ}$ , a zenith angle range similar to that of Mrk 421 observation. A total of  $(634 \pm 73)$  events were obtained in an observation time of  $\sim 63.33$  h with a corresponding  $\gamma$  ray rate of  $\sim (10.01 \pm 1.1$   $h^{-1}$ . This  $\gamma$ -ray rate is designated as a reference of 1 Crab Unit (CU). The same trained

### 3.6. Random Forest method Application on Mrk421 observation

---

forest was employed for estimating the excess events as well as the energy spectrum for Mrk 421. All the observation spells were analyzed individually. The Table 3.4 shows the spell wise analysis. The significance of the signal was calculated by using Li & Ma [123].

Spell	Obs. time ( hrs. )	$\gamma$ -ray events	$\gamma$ -ray rate ( $\text{h}^{-1}$ )	Significance ( $\sigma$ )
I	9.24	23 (9)	2.49 (0.97)	1.72 (0.37)
II	35.71	322 (275)	9.01 (7.70)	6.91 (5.79)
III	61.53	730 (676)	11.86 (10.99)	13.8 (10.64)
IV	34.54	131 (91)	3.79 (2.64)	3.2 (1.94)
V	31.14	100 (61)	3.38(1.96)	3.2 (1.61)
VI	29.55	151 (123)	5.10 (4.16)	4.0 (3.86)
All data	201.72	1457 (1236)	7.22 (6.13)	14.6 (11.49)
II +III	97.24	1052 (951)	10.82 (9.78)	13.8 (12.00)

Table 3.4: Detailed Spell wise analysis report of Mrk 421 data due to RF (DSC)

The data from all the spells (I-VI) yielded a total of  $(1457 \pm 90)$  events with a statistical significance of  $14.6 \sigma$ . Figure 3.19 shows the  $\alpha$  plot for the Mrk 421 source for the entire observation  $\sim 202$  h. It demonstrates that compared to the Dynamic Supercuts method, which produced a total of  $(1236 \pm 110)$  events with a statistical significance of  $11.5 \sigma$ , the Random Forest method leads to an improvement in the excess  $\gamma$ -ray events by  $\sim 18\%$ .

### 3. VARIOUS MACHINE LEARNING METHODS

---

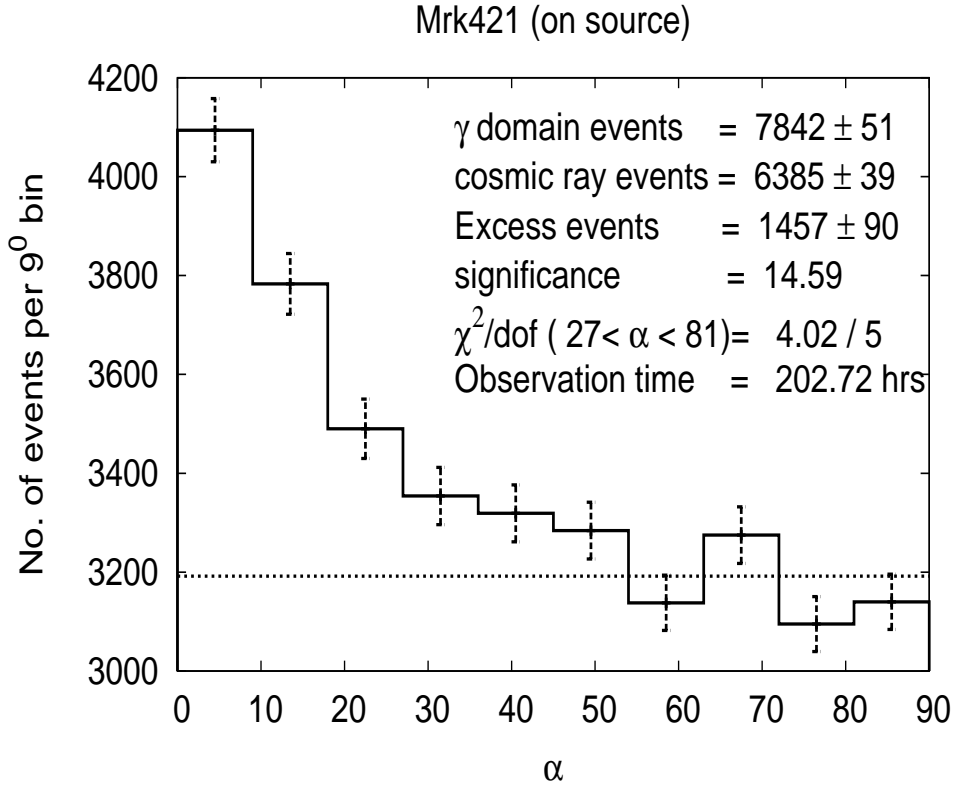


Figure 3.19: On source  $\alpha$  plot for Mrk 421 during December 07, 2005 - April 30, 2006 for  $\sim 202$  h. The expected background events were obtained using the background region ( $27^\circ \leq \alpha \leq 81^\circ$ )

and significance by  $\sim 26\%$ .

## 3.7 Energy spectrum of Mrk 421

The primary  $\gamma$ -ray energy reconstruction was carried out by using few Hillas image parameters by applying the Artificial Neural Network method (ANN) [89, 107]. For a single imaging telescope, the energy reconstruction is a function of image parameters size (number of phototelectron), zenith angle and Distance. The energy estimation was carried out by employing a 3:30:1 ( i.e. 3 nodes in the input layer, 30 nodes in hidden layer and 1 node in the output layer) configuration of ANN with back propagation training al-

### 3.7. Energy spectrum of Mrk 421

---

gorithm [129]. We used a total of 10,000  $\gamma$ -ray showers for training the network. The showers were generated at five zenith angles ( $5^0$ ,  $15^0$ ,  $25^0$ ,  $35^0$  and  $45^0$ ). The effective area as a function of zenith angles and energy was estimated by the standard procedure [103]. The trained network provided the weights which were used to estimate the energy of excess  $\gamma$ -ray events.

The differential photon flux per energy bin is a direct function of zenith angle, energy-dependent effective area and  $\gamma$ -ray retention. Eventually, the spectrum is obtained by using the formula

$$\frac{d\Phi}{dE}(E_i) = \frac{\Delta N_i}{\Delta E_i \sum_{j=1}^5 A_{i,j} \eta_{i,j} T_j} \quad (3.23)$$

where  $\Delta N_i$  and  $d\Phi(E_i)/dE$  are the number of events and the differential flux at energy  $E_i$ , measured in the  $i^{th}$  energy bin  $\Delta E_i$  and over the zenith angle range of  $0^{\circ}$  -  $45^{\circ}$ , respectively.  $T_j$  is the observation time in the  $j^{th}$  zenith angle bin with corresponding energy-dependent effective area ( $A_{i,j}$ ) and  $\gamma$ -ray acceptance ( $\eta_{i,j}$ ). The 5 zenith angle bins ( $j=1-5$ ) used are  $0^{\circ}$ - $10^{\circ}$ ,  $10^{\circ}$ - $20^{\circ}$ ,  $20^{\circ}$ - $30^{\circ}$ ,  $30^{\circ}$ - $40^{\circ}$  and  $40^{\circ}$ - $50^{\circ}$  with effective collection area and  $\gamma$ -ray acceptance values available at  $5^{\circ}$ ,  $15^{\circ}$ ,  $25^{\circ}$ ,  $35^{\circ}$  and  $45^{\circ}$ . The number of  $\gamma$ -ray events ( $\Delta N_i$ ) in a particular energy bin is calculated by subtracting the expected number of background events from the  $\gamma$ -ray domain events. In order to validate the trained ANN, the spectrum from Crab Nebula was reproduced. The spectrum of crab nebula is fitted by a power law with ( $d\Phi/dE = f_0 E^{-\Gamma}$ ) with  $f_0 \sim (1.944 \pm 0.15) \times 10^{-11} cm^{-2}s^{-1}TeV^{-1}$

### 3. VARIOUS MACHINE LEARNING METHODS

---

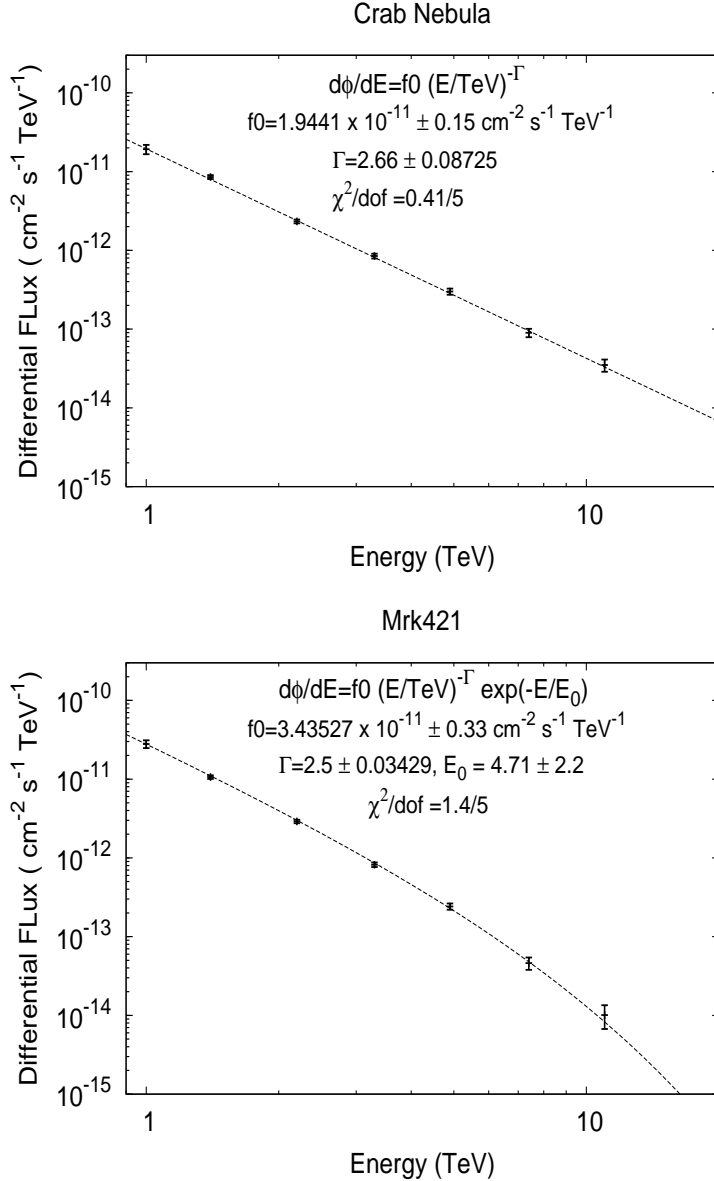


Figure 3.20: The top panel shows the Crab Nebula spectrum during November 10, 2005 - January 30, 2006 for  $\sim 101$  hrs. The bottom panel shows the Mrk 421 spectrum during Spell II and III during December 07, 2005 - April 30, 2006 for  $\sim 97.24$  hrs.

and  $\Gamma \sim 2.66 \pm 0.08725$ . After reproducing the Crab Nebula spectrum, we obtained the spectrum of Mrk 421 for the spells II and III where the source was emitting at more than 1 CU. The resultant spectrum is well fitted by a simple power law with exponential cut off ( $d\Phi/dE = f_0(E/E_0)^{-\Gamma}$ ) with  $f_0 \sim (3.435 \pm 0.33) \times 10^{-11} \text{ cm}^{-2} \text{s}^{-1} \text{TeV}^{-1}$  and

$\Gamma \sim 2.5 \pm 0.03429$  and  $E_0 = 4.71 \pm 2.2$ . Both the obtained spectra (Figure 3.20) match well with the previously reported results [89].

#### 3.7.1 Result and Discussion

The extragalactic source Mrk 421 was observed by the TACTIC imaging telescope during December 07, 2005 - April 30, 2006 for  $\sim 202$  hrs. Previous analysis of this data using the Dynamic Supercuts method led to a detection of flaring activity from the source at Energy  $> 1$  TeV. Here we reanalyzed this data by using the machine learning method Random Forest. The Dynamic Supercuts method as well as the Random Forest method showed that the Mrk 421 was in the high state in Spell II and III. The key result of this study is that the Random Forest method estimated more excess  $\gamma$ -ray like events compared to previous results [89]. This is so because while the Dynamic Supercuts method estimated a total of 1236 excess  $\gamma$ -ray like events from the entire data, the Random Forest method yielded a total of 1457 events, i.e. 221 events more. The signal strength estimated by the Random Forest method was  $14.6 \sigma$  as compared to the same obtained by Dynamic Supercuts method ( $11.49 \sigma$ ). The energy spectrum of Mrk 421 as measured by the TACTIC telescope for spell II and III is compatible with a power law with exponential cut off. In addition to the source detection in high state in Spell II and III, TACTIC also observed this source during the last lag of Spell VI in the month of April 2006. It may be mentioned that during this period, this source was also observed by various groups. Whipple telescope [127] carried out the observation in April and June 2006. MAGIC telescope observed this source from April 22 to April 30, 2006 [126]. Both these groups detected this source in high state. However, TACTIC has only a  $4.10 \sigma$  (see Table 3.4)

### **3. VARIOUS MACHINE LEARNING METHODS**

---

detection during this period.

The applicability and superiority of Random Forest method over Dynamic Supercuts method for the TACTIC telescope has been demonstrated by the present study.

# 4

## MACE Sensitivity estimate

#### 4. MACE SENSITIVITY ESTIMATE

---

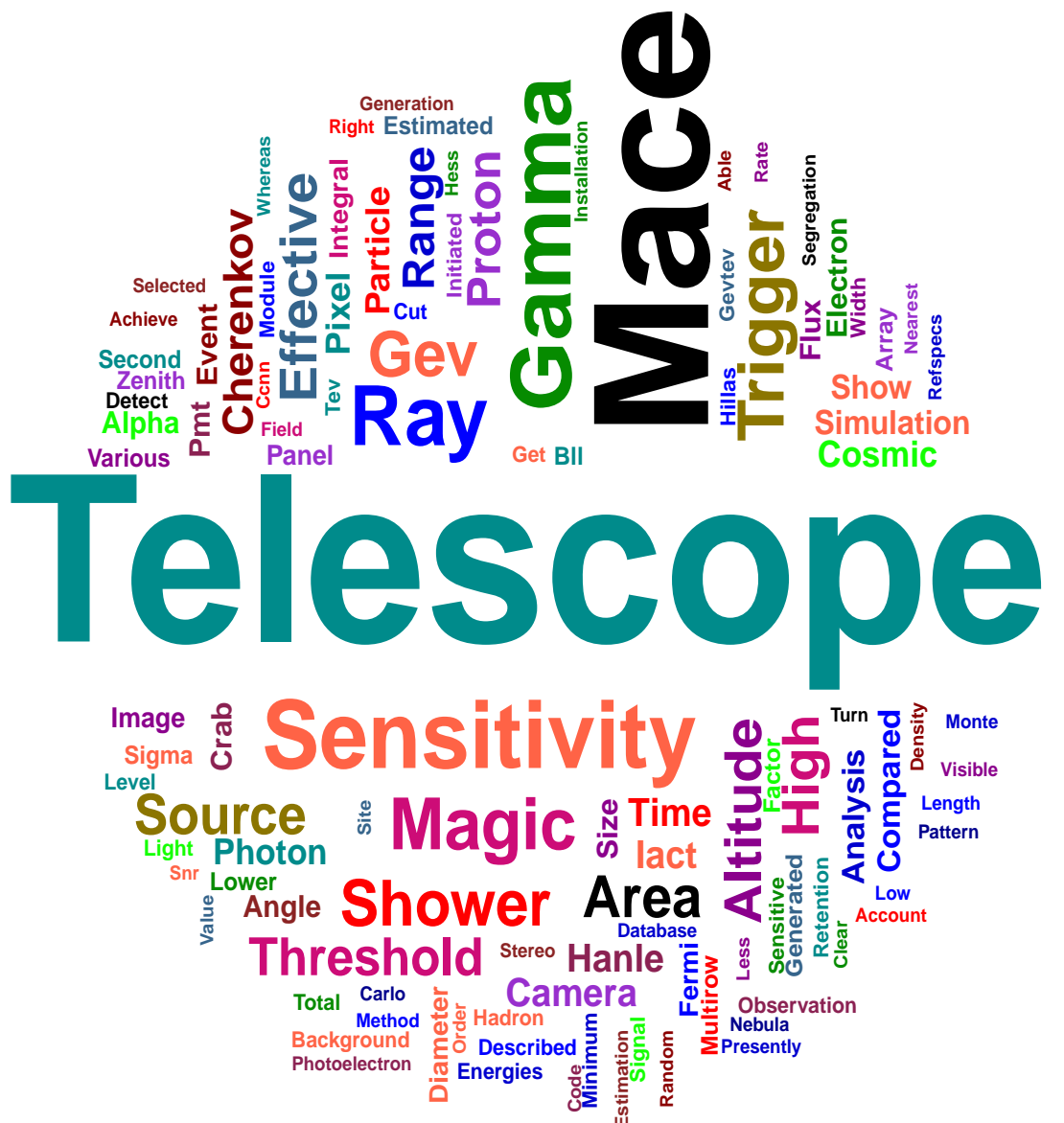


Figure 4.1: Summary of Chapter 4. The size of word represents the number frequency.



Figure 4.2: MACE 21m diameter dish in Hyderabad.

The MACE (Major Atmospheric Cherenkov Experiment) is a 21 m diameter  $\gamma$ -ray telescope which is presently being installed at Hanle in Ladakh, India (**32° 46' 46" N, 78° 58' 35" E**) at an altitude of 4270 m a.s.l. Once operational, it will become the highest altitude very high energy (VHE)  $\gamma$ -ray telescope in the world based on Imaging Atmospheric Cherenkov Technique (IACT). In this chapter, we discuss the sensitivity estimate

#### 4. MACE SENSITIVITY ESTIMATE

---

of the MACE telescope by using a substantially large Monte Carlo simulation database at  $5^\circ$  zenith angle. The sensitivity of MACE telescope is estimated by carrying out the  $\gamma$ -hadron segregation using the Random Forest method. It is estimated that the MACE telescope will have an *analysis* energy threshold of 38 GeV for image intensities above 50 photoelectrons. The integral sensitivity for point like sources with Crab Nebula-like spectrum above 38 GeV is  $\sim 2.7\%$  of Crab Nebula flux at  $5\sigma$  statistical significance level in 50 hrs of observation.

Presently three major operational IACT based telescopes are MAGIC [93], HESS [?] and VERITAS [130] MAGIC telescope consists of  $2 \times 17$  m diameter telescopes on the Canary island of La Palma. The analysis energy threshold of stereo MAGIC telescope is  $\sim 84$  GeV [93]. The VERITAS telescope is an array of four 12 m diameter telescopes at southern Arizona, USA. It has an analysis energy threshold of  $\sim 135$  GeV [131]. HESS telescope, situated in Namibia, is a mixed array consisting of four 12 m telescopes, named as HESS-I and one 28 m large size telescope, named as HESS-II. HESS-I alone operates at an analysis energy threshold of  $\sim 158$  GeV [132] whereas the preliminary simulation studies show that HESS-II has an analysis energy threshold of  $\sim 50$  GeV [133]. In order to augment the capability of IACT based telescopes in few GeV to few TeV energy range, an international consortium of worldwide researchers are setting up an open observatory known as the Cherenkov Telescope Array (CTA) [134]. CTA will consist of two large arrays of IACT based telescopes, one in the Northern Hemisphere with an emphasis to study extragalactic objects and a second array in the Southern Hemisphere to concentrate on galactic sources. The Southern array which is being set up

---

first will deploy telescopes of various diameters to cater to the wide energy range of few tens of GeV to few tens of TeV. A compact array of 4 x 23 m diameter telescopes will cater to the lower end of energy range.

In the same endeavour, a new Indian initiative in gamma-ray astronomy, the Himalayan Gamma Ray Observatory (HIGRO), is setting up an IACT based telescope known as the **MACE** (**M**ajor **A**tmospheric **C**herenkov **E**xperiment) at Hanle in the Ladakh region of northern India. MACE, presently being set up at an altitude of 4270m, is a 21m diameter telescope with a total light collector area of  $\sim 337 \text{ m}^2$  with effective focal length of  $\sim 25 \text{ m}^2$ . Compared to the high altitude of MACE telescope, MAGIC, HESS and VERITAS telescopes are operational at an altitude of 2225 m, 1800 m and 1275 m respectively. The idea of an IACT based telescope at high altitude (5 km) was introduced by Aharonian et al. (2006) [128]. They discussed the concept of a stereoscopic array of several large imaging atmospheric Cherenkov telescopes having an energy threshold of 5 GeV. Although it should be noted that they discussed about a stereo array, whereas MACE is a standalone single telescope. The stereoscopic approach has many advantages compared to the stand alone IACT. This approach allows unambiguous reconstruction of shower parameters. It also leads to effective suppression of night sky background and muon background because of the reduction in the random coincidences, leading to reduced pixel trigger threshold and hence lower energy threshold. In addition to it, the hadronic showers are rejected more efficiently compared to a single IACT based telescope on shape cuts in multiple views. The simultaneous observation of air shower by stereoscopic telescope, compared to a single telescope, leads to improved shower direction

## 4. MACE SENSITIVITY ESTIMATE

---

reconstruction as well as core location. The main advantage of having a stereoscopic array of 20 m diameter telescope at an altitude of 5 km is very low  $\gamma$  ray energy threshold  $\sim 5$  GeV on account of less absorption of Cherenkov photon, as well due to geometric effect on account of higher altitude leading to higher photon density.

In the present Chapter, we will discuss the performance of the MACE telescope by estimating its sensitivity. This study is organized as follows. In Section 4.1, we will introduce the MACE telescope. Section 4.2 will have a discussion the generation of Monte Carlo simulation database. In section 4.3, we will estimate the Integral sensitivity for the MACE telescope. Results and discussion will be presented in section 4.4.

### 4.1 The MACE telescope

The MACE is an Indian effort to set up a very high energy (VHE)  $\gamma$ -ray IACT based telescope. The installation of this telescope is presently going on at Hanle (**32° 46' 46" N, 78° 58' 35" E**) in Ladakh, India at an altitude of 4270 m a.s.l. It is a 21 m diameter telescope which will deploy a photomultiplier tube (PMT) based imaging camera consisting of 1088 pixels. The diameter of each PMT is 38 mm with angular resolution of  $0.125^\circ$  and an optical field of view of the full camera  $\sim 3.4^\circ \times 4^\circ$ . In order to reduce the dead space between the PMTs, a light concentrator having a hexagonal entry aperture of 55 mm and a circular exit aperture of 32 mm is placed on top of the PMTs. The imaging camera of MACE telescope has been designed in a modular manner consisting of 68 modules of 16 channels each. The MACE camera layout has been shown in Figure 4.3. The detailed trigger scheme is described in [135]. Out of 1088 pixels, the innermost 576 pixels ( $24 \times 24$ ) will be used for trigger generation. The trigger field of view

## 4.1. The MACE telescope

---

is  $\sim 2.6^\circ \times 3^\circ$ . Conventionally, the event trigger in an Atmospheric Cherenkov Telescope is generated by demanding a fast coincidence between few PMTs, generally 2-6. Since the  $\gamma$ -ray images are more compact compared to the background events, the chance coincidence rate can be reduced by limiting the n-fold topological combination of pixels. The MACE telescope uses nearest neighbour close cluster patterns. It has an option of using various programmable trigger configuration such as 2 CNN (close cluster nearest neighbour pairs), 3 CNN (close cluster nearest neighbour triplets), 4 CNN (close cluster nearest neighbour quadruplets). Here CNN is defined as the pattern in which if any one of the fired pixels is removed, the remaining pixels should be still adjacent. MACE trigger will be generated in two stages: In the first stage a m-fold coincidence in a module between nearest neighbor pixels with a coincidence gate width of 5 ns is demanded. In the second stage, partial triggers from individual modules are collated so that events spread over adjacent modules (2,3 or 4) satisfying the chosen multiplicity condition generate the trigger. The MACE camera layout with 3, 4 and 5 CNN trigger patterns is shown in Figure 4.3.

MACE Telescope will use a quasi-parabolic light collector to image the Cerenkov flash on a PMT camera. The light collector of the telescope will be made of 356 mirror panels of  $984\text{ mm} \times 984\text{ mm}$  size fixed at a square pitch of 1008 mm on a paraboloid shape dish. Each panel will consists of four  $488\text{ mm} \times 488\text{ mm}$  facets of spherical mirrors made of aluminum with a  $SiO_2$  coating. The total light collector area will be  $\sim 337\text{ m}^2$ . The mirror facets have a graded focal length of 25 - 26.5 m which ensures that the on-axis spot size is minimum at the focal plane.

#### 4. MACE SENSITIVITY ESTIMATE

---

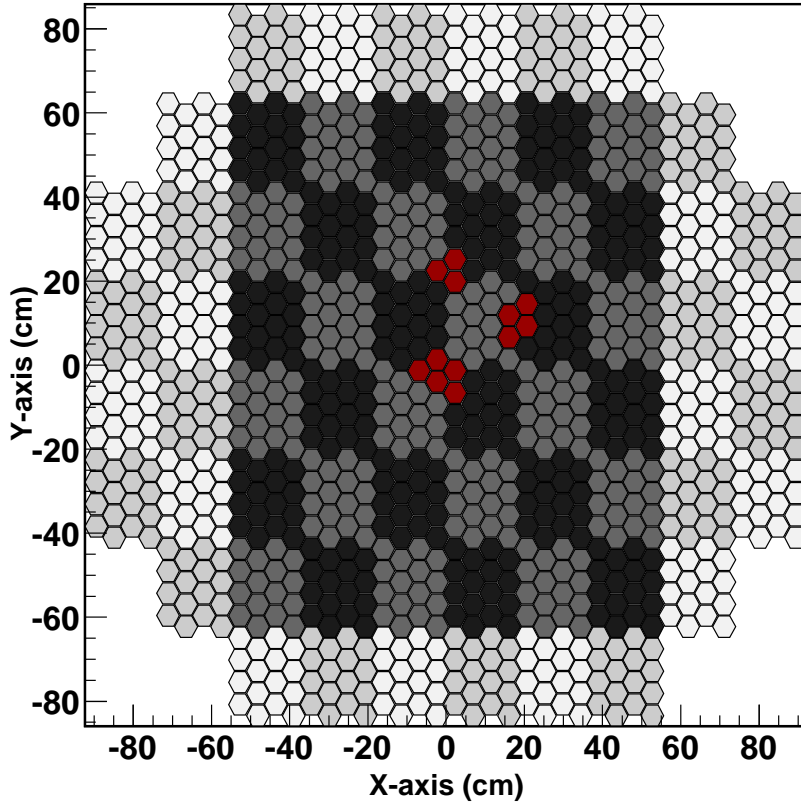


Figure 4.3: The MACE camera layout showing a total of 1088 pixels divided into 68 modules with 16 PMT each. The trigger is generated from the darker shaded area consisting of 576 pixels. Typical trigger pattern of various programmable scheme (3,4,5 CNN) is shown in red color.

## 4.2 Generation of Monte Carlo simulation database

A Monte Carlo simulation database at  $5^\circ$  zenith angle was generated. The extensive air shower (EAS) library for MACE simulation was generated using a standard air shower simulation package CORSIKA (v6.990). This code is developed at Karlsruhe university and available for use on request. This Monte Carlo method based code simulates the secondary particle cascade generation in the atmosphere as high energy primary particle enters the Earth's atmosphere and undergoes many electromagnetic as well as hadronic

## 4.2. Generation of Monte Carlo simulation database

---

interactions. Many models to simulate these interactions are available in this code and the Cerenkov light generation by the relativistic leptons as they zip through the atmosphere is also simulated.

For this work, we have used EGS4 model for the electromagnetic interactions. For low energy (upto 100GeV) hadronic interactions, we have used GHEISHA model while high energy interactions are modelled using QGSJet-I model. We have used CEFFIC option to incorporate the en-route absorption of Cerenkov photon. We have used US standard atmosphere model supplied with CORSIKA package. The observation level was set to the altitude of the telescope site. The Earth's magnetic field values measured at the Hanle are  $31.95 \mu T$  for horizontal component along local north direction and  $38.49 \mu T$  for vertical component in downwards direction. The Cerenkov photons were stored within the wavelength range 240 nm – 650 nm as the MACE camera PMTs are sensitive in this range.

Using this setup, we generated EAS library for four primary particles –  $\gamma$ -ray, proton, electron and  $\alpha$  particle. The spectral indices used are 2.59 [136] for  $\gamma$ -ray, 2.7 for proton, 3.26 for electron and 2.63 for  $\alpha$  particle. Other input parameters which vary with particle type, are listed in Table 4.1. In this work we focused on estimating the sensitivity of the telescope for on-axis point sources only (view cone angle is maintained at zero value for  $\gamma$ -ray showers). The protons, electrons and alpha particles are simulated diffusively in a certain view cone angles, as described in the Table 4.1. We generated more than 34 million  $\gamma$ -ray showers and nearly 1 billion showers for cosmic rays in two energy band encompassing over 3 decades of energies using three high-end workstations

#### 4. MACE SENSITIVITY ESTIMATE

---

particle type	Energy Range	View cone angle(deg)	Scatter radius(m)	No. of showers (million)	No. of Triggered showers
$\gamma$ -ray	10GeV–20TeV	$0^\circ$	400	22.8	1,314,306
	400GeV–20TeV	$0^\circ$	500	12.8	1,569,866
proton	20GeV–20TeV	$3^\circ$	500	356	308,099
	400GeV–20TeV	$3^\circ$	550	64	169,221
electron	10GeV–20TeV	$3^\circ$	500	384	432,631
	400GeV–20TeV	$3^\circ$	550	64	330,909
$\alpha$ particle	100GeV–20TeV	$3.5^\circ$	550	326	391,653

Table 4.1: Monte Carlo simulation database

comprising of 32 processors each during the actual runtime of more than six months. The telescope simulation program took these shower events as input and ray-traced them to the focal plane of the telescope. The two level trigger logic used in simulation exactly mimics the actual trigger design to be implemented for the MACE telescope. For triggering criteria [135], we have used 9 p.e. as the discrimination threshold for a pixel and the trigger configuration of 4 CCNN pixels was used. For simulation studies, a general purpose IACT simulation code was employed [135] to asses the performance of the MACE telescope. In brief, the general purpose simulation code incorporated the specification for the MACE telescope like camera, reflector and trigger configuration along with the wavelength dependent photon absorption. A poissonian Night Sky Background (NSB) background in each pixel was added in this code. The NSB observation was carried out

## 4.2. Generation of Monte Carlo simulation database

---

at the MACE telescope installation site [137] during 2003 - 2007 using CCD images taken with the Himalayan Chandra Telescope (HCT). The estimated NSB rate per pixel turns out to be  $\sim 1.46$  photoelectrons [135]. The Cherenkov photons falling on the image plane of the camera underwent usual image analysis procedure developed by Hillas [26]. The spatial distribution (of Cherenkov photons) generates different patterns for signal ( $\gamma$ -rays generated Cherenkov photons) as well as for background (protons, electrons, alpha particles generated Cherenkov photons) events. This difference in shape and size is exploited for the extraction of signal. All these parameters are affected by the NSB, therefore, the conventional practice of image cleaning [99] is employed. We employed a two step image cleaning procedure: picture and boundary and picture thresholds of  $10\sigma$  and  $5\sigma$  was used respectively. The clean Cherenkov images were characterized by various Hillas image parameters like Length, Width, Distance, Alpha, Size, Frac2 and asymmetry. Once clean images were obtained, the  $\gamma$ -hadron segregation was carried out by using the Random Forest method, described in [138, 139].

A typical distribution of various Hillas parameters for all the simulated primaries is shown in Figure 4.4 and 4.5 . Please note that since the frequency distribution of Hillas parameters for all the simulated four species in a single plot appears cluttered, we have presented the distribution for gamma, protons and alpha particles in Figure 4.4 and frequency distribution of gamma and electrons in Figure 4.5. The Figure 4.6 shows the Pearson parametric correlation coefficient depicting linear dependence between two variables for various Hillas parameters. The linear correlation between various parameters for proton and alpha particle initiated showers is almost similar. However, the linear

#### 4. MACE SENSITIVITY ESTIMATE

---

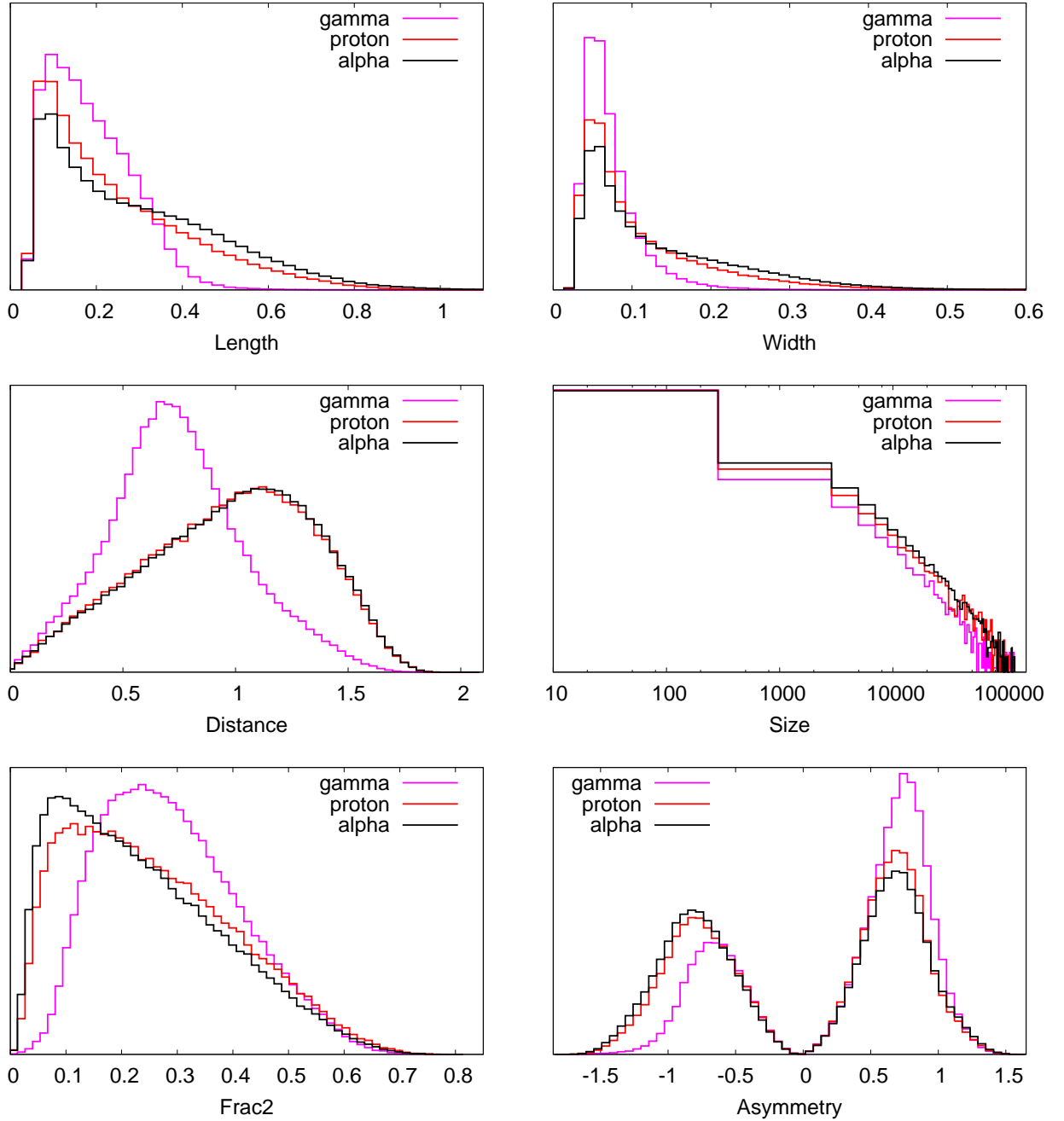


Figure 4.4: Frequency distribution of Hillas parameters for Gamma, proton and alpha particles initiated showers triggering the MACE telescope.

correlation for gamma and electron events is quite different. Any analysis method which can decipher the interdependence among various parameters is helpful in gamma and

## 4.2. Generation of Monte Carlo simulation database

---

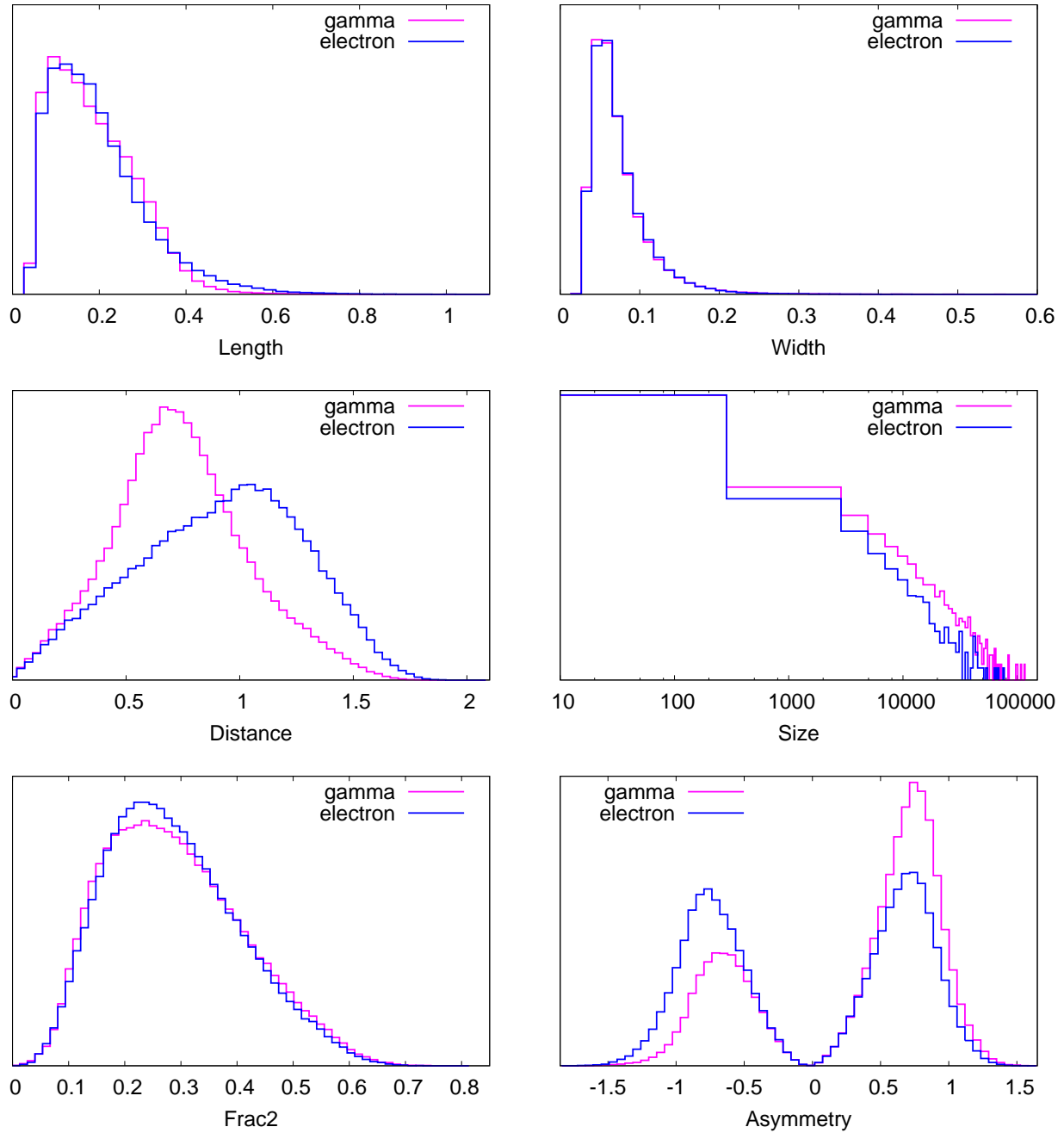


Figure 4.5: Frequency distribution of Hillas parameters for Gamma and electron initiated showers triggering the MACE telescope.

non gamma events segregation. Probably the Random Forest method is quite effective in scrubbing out the interdependence among various parameters, therefore, the segregation

## 4. MACE SENSITIVITY ESTIMATE

---

of electrons from gamma initiated showers did not hinder the gamma and electron events segregation although there is just one radiation length difference in gamma and electrons initiated showers. We have also shown the Length and Width vs Energy distribution plot

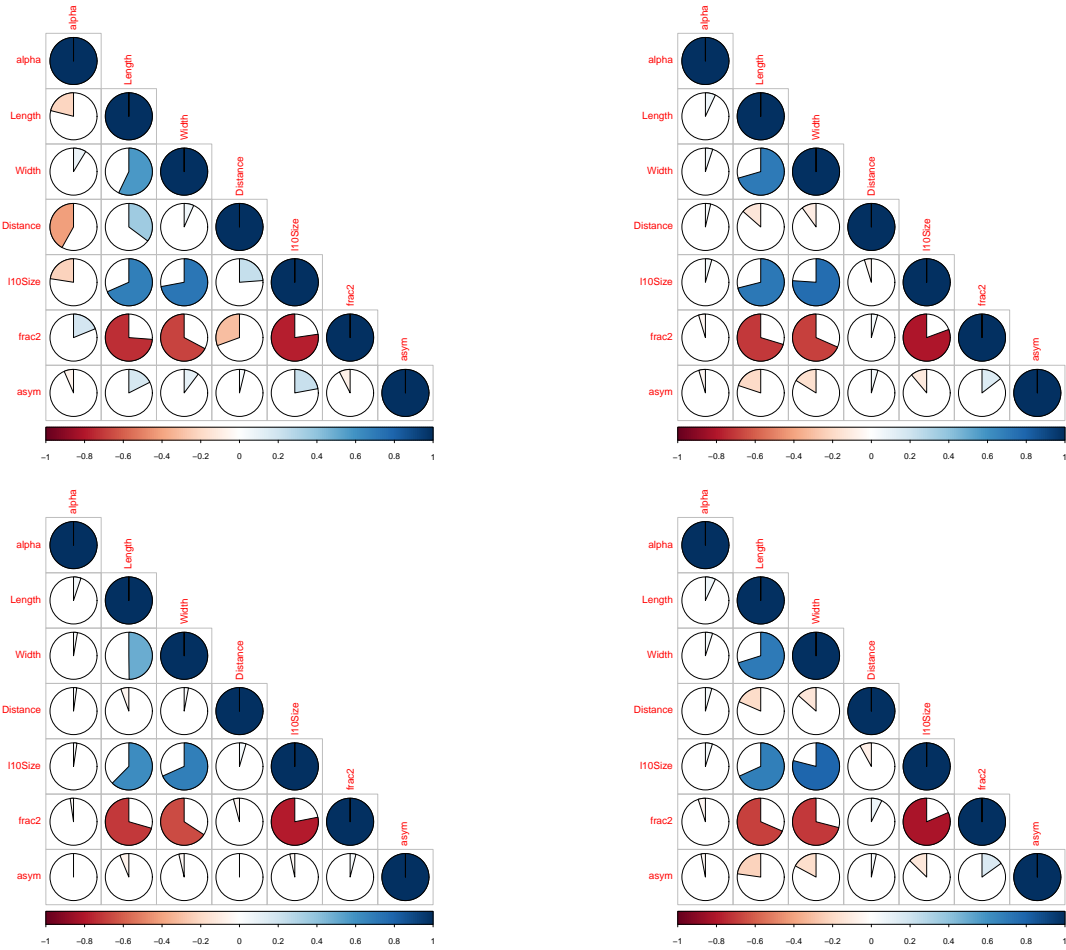


Figure 4.6: The Pearson parametric correlation coefficient showing linear dependence between two variables for various Hillas parameters for: gamma rays (top most left panel), protons (top most right panel), electrons (bottom most left panel), alpha particles (bottom most right panel).

for  $\gamma$  and protons in Figure 4.16 (shown in the Appendix 4.5.2).

### 4.2.1 Height dependent properties of Cherenkov radiation

The TACTIC telescope described in the last chapter is located at an altitude of 1.3 kms a.s.l whereas the altitude of the MACE telescope is  $\sim 4.2$  kms. The properties of Cherenkov radiation is very different at these locations. The Figure 4.7 shows the wavelength dependent Cherenkov emission at these two locations. The difference in the

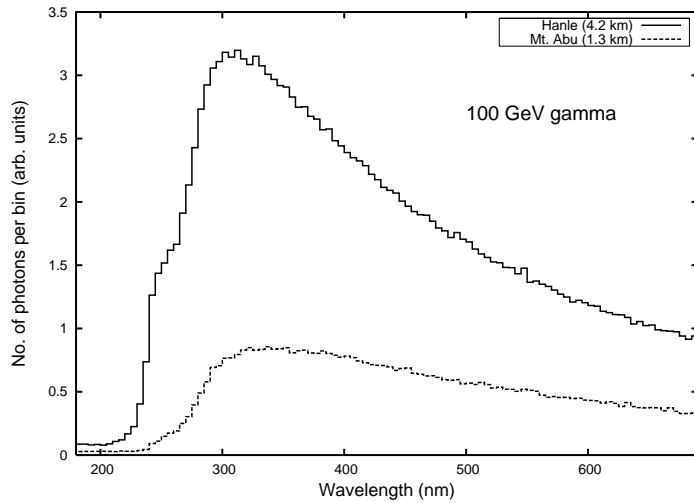


Figure 4.7: Wavelength dependent Cherenkov emission for 100 GeV  $\gamma$ -ray showers arriving within a core distance of 60-80 m at TACTIC ( $\sim 1.3$ km a.s.l) and at Hanle ( $\sim 4.2$ km a.s.l) altitude for vertically incident showers.

Cherenkov photon density at these locations can be understood geometrically. Since the altitude of MACE telescope is higher, geometrically the Cherenkov light pool shrinks at Hanle altitude leading to increased photon density. The Figure 4.8 shows the difference in the photon density at TACTIC and Hanle observation level. However, it should be noted that the increase in the Cherenkov photon density is more for  $\gamma$ -ray initiated showers compared to the proton initiated showers. The possible reason is the truncation of hadronic showers compared to  $\gamma$ -ray initiated showers (visible from the Figure 4.9,

#### 4. MACE SENSITIVITY ESTIMATE

---

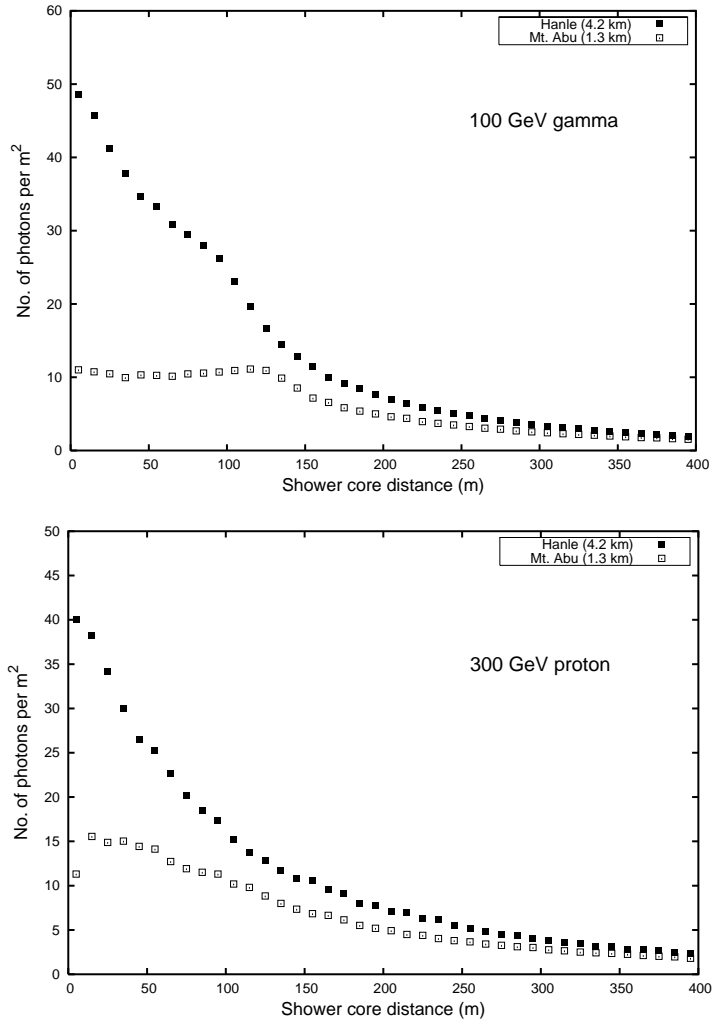


Figure 4.8: Cherenkov Photon density distribution for: Top panel (100 GeV  $\gamma$ -rays), Bottom panel (300 GeV proton).

showing the development of these showers at Hanle altitude). The Figure 4.10 shows the integrated longitudinal distribution of Cherenkov photons as a function of atmospheric thickness  $X$  for  $\gamma$ -rays with energies 100 GeV and 1 TeV and for protons of energies 300 GeV and 5 TeV energies. It is clear from this figure that 1 TeV  $\gamma$ -rays initiated showers gets fully developed ( $\sim 97\%$  Cherenkov photons production is complete). However, a sharp contrast is seen the case of proton initiated showers where only  $\sim 80\%$  of 300 GeV proton shower gets completed. Since the proton initiated showers are not fully developed

### 4.3. Integral Sensitivity

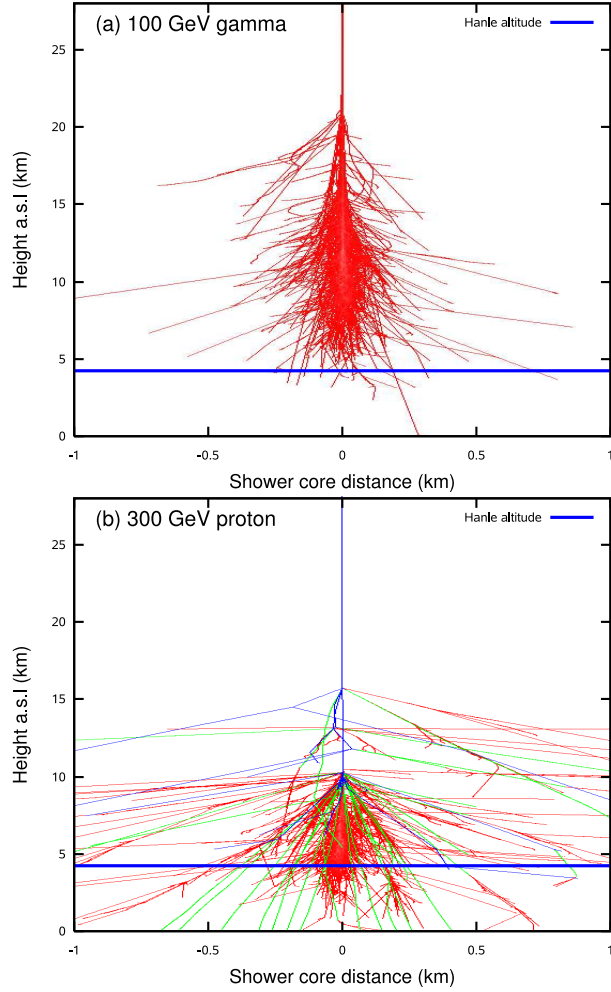


Figure 4.9: Development of 100 GeV  $\gamma$  and 300 GeV proton showers.

at Hanle altitude, it might cause problem in  $\gamma$ -hadron segregation at higher energies.

## 4.3 Integral Sensitivity

The sensitivity of a gamma-ray telescope is determined by its ability to detect gamma-ray signal in overwhelming presence of cosmic ray background. The sensitivity of a telescope depends on amount of area over which the detector is sensitive to the events and it will be called effective area of the telescope. For an IACT based telescope the effective area is orders of magnitude bigger than the size of the light collector. The effective area of

#### 4. MACE SENSITIVITY ESTIMATE

---

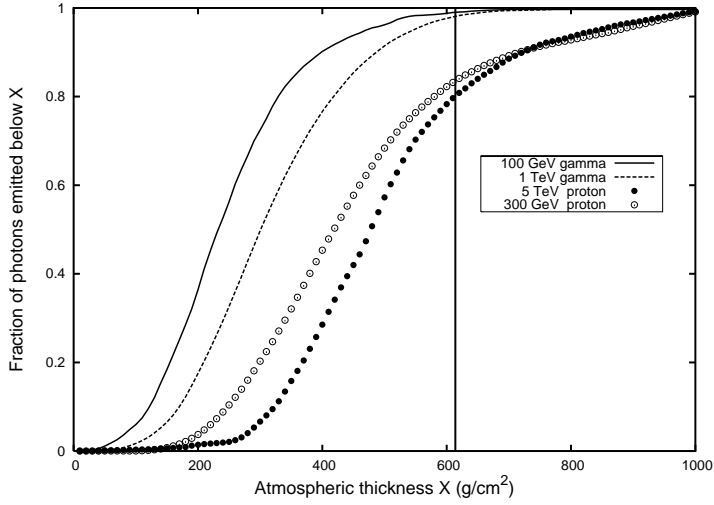


Figure 4.10: Integrated longitudinal distribution of Cherenkov photons for 100 GeV & 1 TeV  $\gamma$  and 300 GeV & 5 TeV of proton showers. The thick vertical line at  $X = 614\text{g}/\text{cm}^2$  is the atmospheric thickness at Hanle (4.2km a.s.l.).

MACE telescope for the  $\gamma$ -rays originating from an on-axis point source is estimated by integrating the total retention factor for  $\gamma$ -rays over all the core distances from the telescope as shown in the equation 4.3. Normally, the effective area is also a function of zenith angle but since we are reporting the results at a particular zenith angle, the zenith angle dependence is not shown explicitly. The effective area is defined as

$$A_{eff}^\gamma(E) = 2\pi \int_0^\infty dR R \times \eta_{total}^\gamma(E, R) \quad (4.1)$$

Here,  $\eta_{total}^\gamma$  is the total retention factor for  $\gamma$ -rays and it includes the trigger retention factor as well as the retention factor due to  $\gamma$ -selection cut. If  $dN_{simulated}$  is the number of events used in the simulation and  $dN_{selected}(E, r)$  is the number of events triggering the telescope as well as selected on the basis of  $\gamma$ -selection cut as described above then

### 4.3. Integral Sensitivity

---

the total retention factor is defined as,

$$\eta_{total}^\gamma(E, r) = \eta_{trigger}^\gamma(E, r) \cdot \eta_{cut}^\gamma(E, r) = \frac{dN_{selected}(E, r)}{dN_{simulated}(E, r)} \quad (4.2)$$

Similarly the effective area for each of the cosmic ray particles (protons, electrons and  $\alpha$  particles) is estimated by integrating its respective total retention factor at different core distances over all the core distances as well as over all the angles within the view-cone solid angle around the optic axis of the telescope, as shown in the following equation;

$$A_{eff}^{\mathbb{X}}(E) = 2\pi \int_0^{\infty} dR R \int_0^{\Omega_{vc}} d\Omega \eta_{total}^{\mathbb{X}}(E, R, \Omega); \quad (\mathbb{X} = proton, electron, \alpha) \quad (4.3)$$

The total retention factor for cosmic ray particles is determined in same manner as in the case of  $\gamma$ -rays and is shown below,

$$\eta_{total}^{\mathbb{X}}(E, r, \Omega) = \frac{dN_{selected}(E, r, \Omega)}{dN_{simulated}(E, r, \Omega)}; \quad (\mathbb{X} = proton, electron, \alpha) \quad (4.4)$$

The trigger effective areas for  $\gamma$ -rays and all the three cosmic ray species are shown in the left panel of Figure 4.11. The after-analysis effective area,  $A_{eff}^\gamma(E)$ , for  $\gamma$ -rays is shown in the right panel of Figure 4.11 along with the trigger effective area for direct comparison. The “analysis effective area” is estimated by applying the hadronness cut value of 0.9 with size greater than 50 photoelectrons. The value of hadronness is chosen by optimizing the sensitivity. It is clear from the right panel of Figure 4.11 that the analysis effective area for  $\gamma$  rays for the MACE telescope is much lower than the trigger effective area.

#### 4. MACE SENSITIVITY ESTIMATE

---

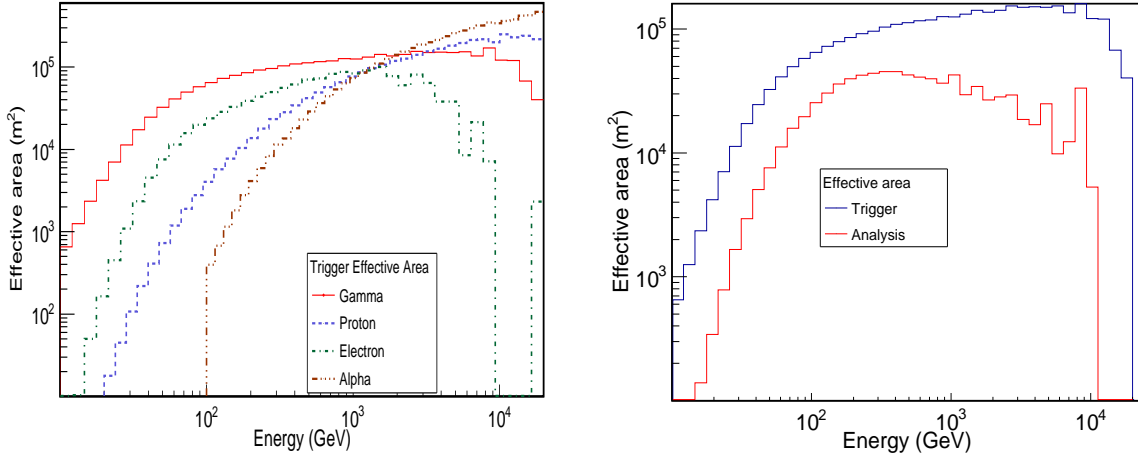


Figure 4.11: Left panel shows the Trigger effective area for the MACE telescope for various cosmic ray particles like electrons, alpha particles, protons as well as cosmic  $\gamma$ -rays. The right panel shows the trigger and analysis effective area for cosmic  $\gamma$ -rays.

This effect is especially visible for higher energies. The effective area above 1 TeV shows large fluctuations on account of poor shower statistics. The effective area after analysis for proton events is shown in Figure 4.15 (shown in Appendix 4.5.1).

The integral sensitivity of an IACT based telescope is determined by calculating the minimum detectable integral flux of gamma-rays from Crab-like source and having energies more than pre-determined threshold energy at  $5\sigma$  confidence level in 50 hours of observation. The threshold energy used in this estimation is the energy at which the differential trigger rate of gamma-ray events having sizes more than certain pre-determined size is maximum. For integral sensitivity estimation, we have used 50 photoelectrons as minimum size and subsequently the size is increased by 1.5 times the earlier value. For each size value we demanded that the source flux for energies more than the threshold energy should be such that the significance as defined by equation 4.5 had

### 4.3. Integral Sensitivity

---

to be  $5\sigma$  in 50 hours of observation time and also at least 10  $\gamma$ -rays should be selected.

$$N_\sigma = \frac{N_\gamma}{\sqrt{N_\gamma + 2N_{CR}}} \quad \text{where, } N_{CR} = N_p + N_e + N_\alpha \quad (4.5)$$

Here,  $N_\gamma$  is the number of  $\gamma$ -rays selected after the analysis as described in the earlier section and it is defined by the following equation,

$$N_\gamma = T_{obs} \int_{E_{th}}^{E_{max}} dE \frac{dN_\gamma(E)}{dE} A_{eff}^\gamma(E) \quad (4.6)$$

We have used Crab nebula spectrum as measured by HEGRA [136] for this calculation. And the effective area is calculated using equation 4.3. Similarly the number of cosmic ray particles selected after the analysis are estimated using the following equation,

$$N_{\mathbb{X}} = T_{obs} \int_{E_{th}}^{\Omega_{vc}} d\Omega \int_{E_{th}}^{E_{max}} dE \frac{dN_{\mathbb{X}}(E, \Omega)}{dE} A_{eff}^\gamma(E) \quad (\mathbb{X} = proton, electron, \alpha) \quad (4.7)$$

The cosmic rays spectra used in this calculation are as reported in [140, 141]. Here, the cosmic ray flux is assumed to be isotropic within the view-cone solid angle.

Armed with all the required parameters, we have estimated the sensitivity of the MACE telescope. The minimum analysis energy threshold <sup>1</sup> for the MACE telescope is estimated to be  $\sim 38$  GeV for image intensities above 50 photoelectrons. The integral sensitivity for point like sources with Crab Nebula-like spectrum above 38 GeV is  $\sim 2.7\%$  of Crab Nebula flux at  $5\sigma$  statistical significance level in 50 hrs of observation. The

---

<sup>1</sup>The energy at which differential trigger rate for a particular progenitor particle above a certain size range peaks, is called the *Threshold energy* of the telescope for that particle

#### 4. MACE SENSITIVITY ESTIMATE

---

integral sensitivity of the MACE telescope is shown in Figure 4.12. Along with the MACE sensitivity, we have also shown the sensitivity of the MAGIC-I telescope [142]. It is clear from Figure 4.12 that compared to the MAGIC-I telescope, MACE telescope will have a lower energy threshold (as expected on account of higher altitude). Also, it is clear that MACE telescope will be more sensitive than the MAGIC-I telescope upto 150 GeV.

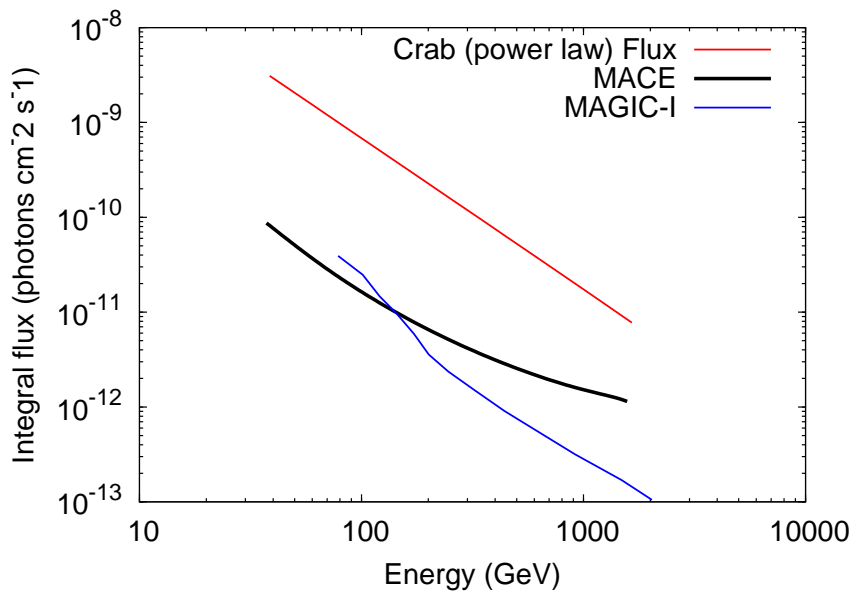


Figure 4.12: Integral sensitivity of the MACE telescope at  $5^\circ$  zenith angle. The sensitivity of the MAGIC-I telescope is also shown.

## 4.4 Results and Discussion

We have estimated the sensitivity of the MACE telescope where the  $\gamma$ -hadron segregation was carried out by employing the Random Forest method. The sensitivity was estimated by generating a substantially large Monte Carlo simulation database at  $5^\circ$  zenith angle. We generated  $\sim 1 \times 10^9$  EAS for various relevant cosmic ray species ( $\gamma$ , Proton, Electron, alpha particles). The MACE telescope is very sensitive in the low energy range, especially

#### 4.4. Results and Discussion

---

below 150 GeV. The analysis energy threshold of MACE telescope turns out to be  $\sim 38$  GeV for size cut  $> 50$  photoelectrons. The MACE telescope will be able to detect a minimum of  $\sim 2.7\%$  Crab flux in 50 hrs of observation. Since the MACE telescope in the present study will operate in mono mode, it is worthwhile to compare the sensitivity of the MACE telescope with respect to the MAGIC-I telescope. Figure 4.12 shows that MACE telescope is able to achieve a better threshold energy of  $\sim 38$  GeV whereas the threshold energy of the MAGIC-I telescope is  $\sim 80$  GeV. Apart from the lower energy threshold, MACE telescope appears to be more sensitive than the MAGIC-I telescope up to an energy of  $\sim 150$  GeV. The high altitude of MACE telescope compared to the MAGIC-I telescope leads to a lower energy threshold compared to the MAGIC-I telescope. It was demonstrated [128] that stereoscopic array of 20 m diameter IACTs based telescope installed at an altitude of  $\sim 5$  km can achieve a  $\gamma$  ray threshold energy of  $\sim 5$  GeV. Therefore, the MACE telescope on account of higher altitude is expected to achieve a low energy threshold. It is also shown [135] that for a  $\sim 1300$  m altitude, the Cherenkov photon density is  $\sim 0.5$  photons/m<sup>2</sup>, while for Hanle altitude it is  $\sim 0.9$  photons/m<sup>2</sup> up to a core distance of  $\sim 100$  m for  $\gamma$  rays of energy 10 GeV. The increase in Cherenkov photon density with increasing altitude is more pronounced for  $\gamma$  ray showers than hadron showers. Therefore the trigger probability for  $\gamma$  ray showers is more than trigger probability for hadron showers leading to better performance of the MACE telescope in the sub 100 GeV energy range.

## 4. MACE SENSITIVITY ESTIMATE

---

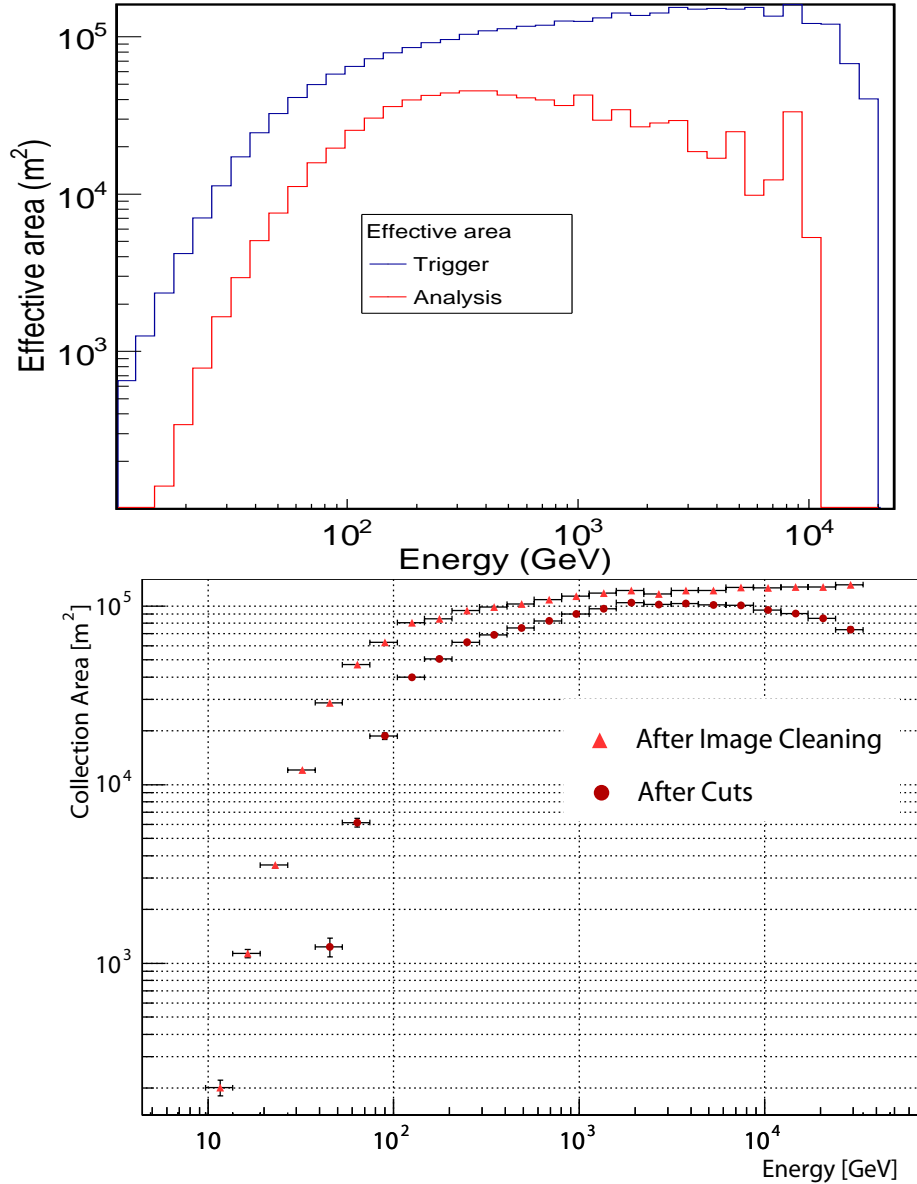


Figure 4.13: The top panel shows the Trigger and analysis effective area for the MACE telescope for cosmic  $\gamma$ -rays. The bottom panel shows it for the MAGIC-I telescope [143].

### 4.4.1 MACE telescope sensitivity in the high energy range

Since the sensitivity of the MACE telescope deteriorates compared to the MAGIC-I telescope in high energy range, its reason was investigated by comparing the effective area of MACE and MAGIC-I telescope for cosmic  $\gamma$ -rays. In the high energy range ( $>$

#### 4.4. Results and Discussion

---

350 GeV), the analysis effective area for the MAGIC-I telescope [143] goes to  $\sim 7 \times 10^4 m^2$  [Trigger effective area  $\sim 1 \times 10^5 m^2$ ] whereas for the MACE telescope, analysis effective area goes to  $\sim 4.5 \times 10^4 m^2$  [Trigger effective area  $\sim 1 \times 10^5 m^2$ ] (Figure 4.13). Clearly, the analysis effective area of the MACE telescope is  $\sim 36\%$  lesser than that of MAGIC-I telescope. Therefore, the sensitivity of the MACE telescope deteriorates in the high energy range compared to the MAGIC-I telescope.

Probably MACE camera design (as shown in Figure 4.3) plays a role in the poorer sensitivity of MACE telescope in the high energy range. It is shown in the literature [128] that:

- “*An inner region with diameter  $\sim 3^\circ$  provides high detection efficiency for -rays, and can be treated as optimal zone for the hardware trigger*”.

In the case of MACE camera, the trigger field of view is  $2.6^\circ \times 3^\circ$  which is less than what is described above. In the above paper, it is also stated that

- “*On the other hand, the IACT technique requires that the camera should be larger than the trigger zone by about one degree, in order to avoid a distortion of the Cherenkov images because of a limited FoV*”.

The MACE camera field of view is  $3.5^\circ \times 4.0^\circ$ , which is again lesser than what is mentioned above (i.e.  $1^\circ$  more than the prescribed hardware trigger). In addition to it, as per the camera design, all the four corners of the camera does not contain any pixel. Due to the violation of above stated facts as well as no-pixels at the corners, the high energy events get leaked. We also estimated the leakage of high energy events. It is also found that

## 4. MACE SENSITIVITY ESTIMATE

---

leakage has played a major role for high energy events (400 GeV). For example, without the leakage cut, total number of simulated gamma ray events for Energy  $> 400$  GeV were 1,569,866. After the application of leakage cut of 10%, more than 59% triggered gamma ray events (642,182) leaked from the MACE camera. So the leakage of high energy events due to camera design probably leads to poorer sensitivity of the MACE telescope with respect to MAGIC-I telescope.

### 4.4.2 Fermi 2FHL sources observable from MACE

To obtain an immediate source list which can be observed for the estimated sensitivity of MACE telescope, we considered the sources listed in second high energy Fermi catalogue [144]. These sources were detected by Fermi in the 50 GeV – 2 TeV energy range over seven years of its operation. To select sources we used the following criteria:

- the source should be visible from the site of MACE telescope.
- the source should have at least  $3\sigma$  detection in Fermi energy range 171 GeV – 585 GeV (second energy band listed in the catalog).
- the source should have non-zero TS value, signifying mere detection by Fermi, in the Fermi energy range 585 GeV – 2 TeV (third energy band listed in the catalog).

Above criteria have been set because MACE telescope is sensitive around 100 GeV and sources in Fermi catalog having  $3\sigma$  detection in 171 GeV–585 GeV energy range generally have more than  $5\sigma$  detection in 50 GeV–171 GeV energy range. Therefore those sources are the best choice to study the performance of the telescope. The Fermi observed spectra of the selected sources along with the MACE sensitivity curve are shown in Figure 4.14. It shows that MACE is expected to detect many more new sources in future. Table 4.2,

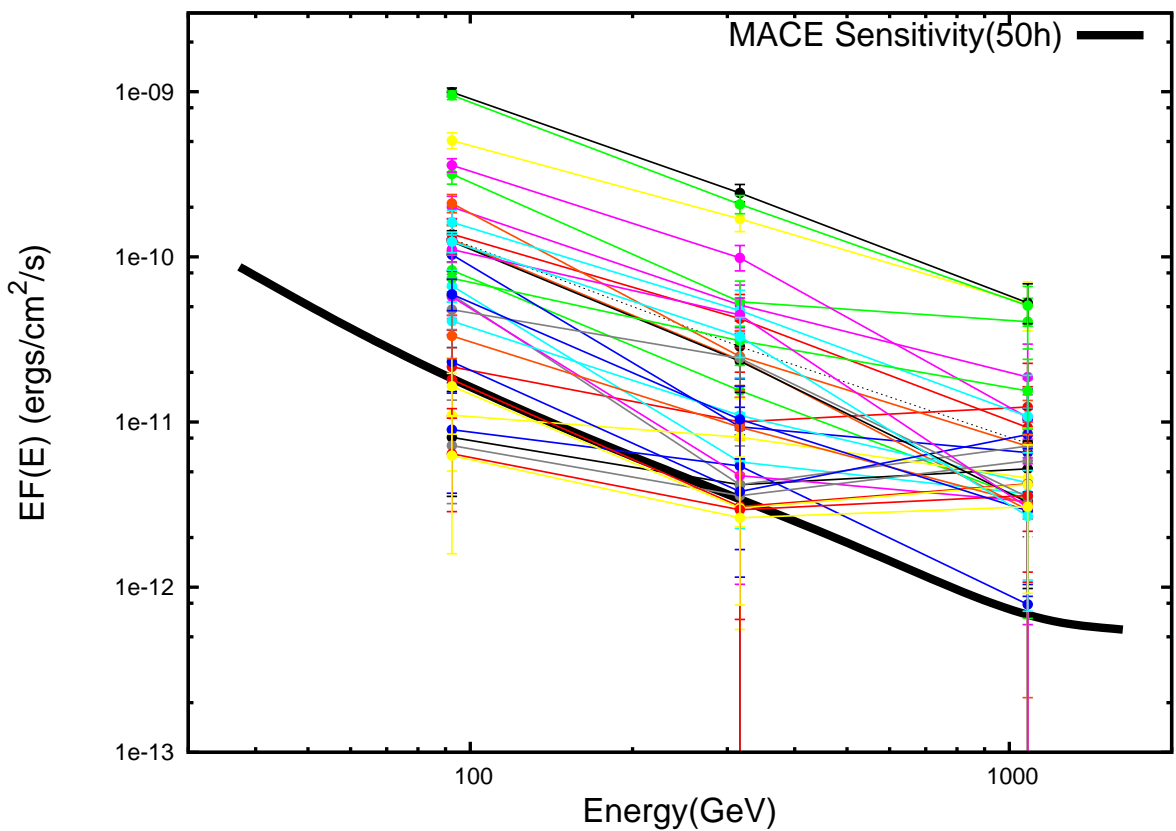


Figure 4.14: MACE integral sensitivity curve along with the sources from second high energy Fermi catalogue chosen such that they are detected with high significance and are visible at MACE telescope site.

## 4. MACE SENSITIVITY ESTIMATE

---

given in the Appendix 4.5.3 lists the sources selected from the second Fermi high energy catalogue visible to the MACE telescope.

### 4.5 Appendix

#### 4.5.1 Effective Area after analysis for protons

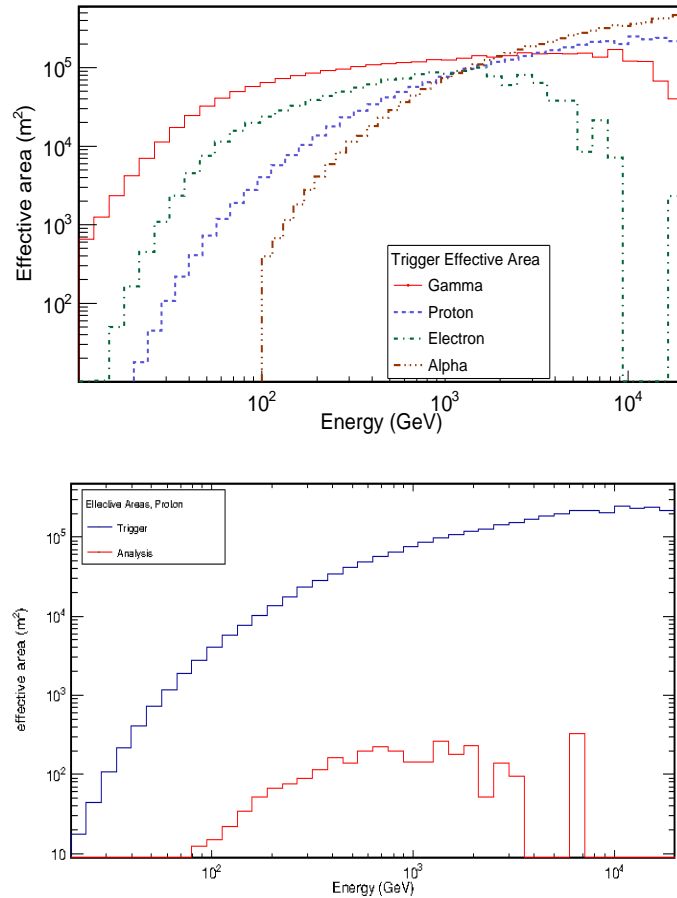


Figure 4.15: Top panel shows the Trigger effective area for the MACE telescope for various cosmic ray particles like electrons, alpha particles, protons as well as cosmic  $\gamma$ -rays. The bottom panel shows the trigger and analysis effective area for cosmic protons.

The effective area for protons after analysis is shown in Figure 4.15.

### 4.5.2 Length/width vs energy distribution

The Figure 4.16 shows the length and width parameter distribution with energy for  $\gamma$  and protons. It is evident from this figure that the length parameter has a strong energy dependence than the width parameter.

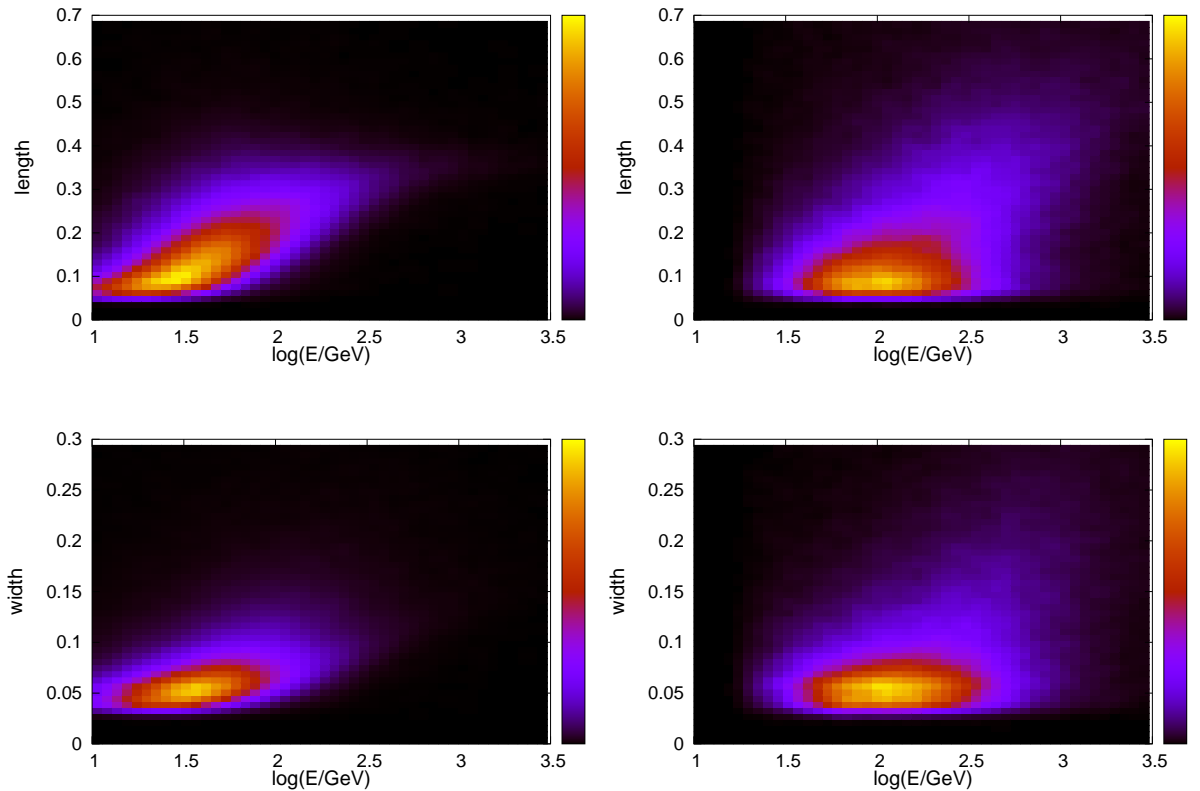


Figure 4.16: The length and width distribution of  $\gamma$  and proton with Energy. The top panel shows the length vs energy distribution of  $\gamma$  and protons whereas the lower panel shows it for width vs Energy.

## 4. MACE SENSITIVITY ESTIMATE

---

### 4.5.3 2FHL Sources visible to MACE telescope

The Table 4.2 list the sources selected from second Fermi high energy catalogue. These sources are visible to MACE telescope.

Source Name	Energy flux (ergs/cm <sup>2</sup> /s)	Spectral index	Associated source	Source Class
2FHLJ1713.5-3945e	4.840E-011	2.03	RXJ1713.7-3946	snr
2FHLJ1745.1-3035	2.689E-011	1.25	–	unk
2FHLJ1745.7-2900	2.449E-011	2.33	GalCentreRidge	spp
2FHLJ1801.3-2326e	2.529E-011	2.55	W28	snr
2FHLJ1805.6-2136e	8.299E-011	1.98	W30	spp
2FHLJ1917.7-1921	1.719E-011	2.44	1H1914-194	bll
2FHLJ1824.5-1350e	2.400E-010	1.89	HESSJ1825-137	pwn
2FHLJ0349.3-1158	1.4700E-011	0.95	1ES0347-121	bll
2FHLJ1834.5-0846e	3.810E-011	2.27	W41	spp
2FHLJ1834.6-0701	1.779E-011	2.25	–	unk
2FHLJ1836.5-0655e	5.560E-011	2.03	HESSJ1837-069	pwn
2FHLJ1840.9-0532e	1.219E-010	2.00	HESSJ1841-055	pwn
2FHLJ0811.9+0238	7.039E-012	1.61	PMNJ0811+0237	bll
2FHLJ1923.2+1408e	1.120E-011	3.76	W51C	snr
2FHLJ0648.6+1516	1.699E-011	2.00	RXJ0648.7+1516	bll
2FHLJ0319.7+1849	1.210E-011	1.45	RBS0413	bll-g
2FHLJ0534.5+2201	3.520E-010	2.13	Crab	pwn
2FHLJ0617.2+2234e	4.970E-011	2.66	IC443	snr
2FHLJ0809.5+3458	1.089E-011	1.09	B20806+35	bll-g
2FHLJ2016.2+3713	9.530E-012	1.74	SNRG74.9+1.2	spp
2FHLJ1104.4+3812	3.290E-010	2.14	Mkn421	bll
2FHLJ2249.9+3826	1.410E-011	1.68	B32247+381	bll
2FHLJ1653.9+3945	1.280E-010	2.13	Mkn501	bll
2FHLJ2021.0+4031e	6.719E-011	1.99	GammaCygni	snr
2FHLJ0316.6+4120	1.330E-011	1.34	IC310	rdg
2FHLJ1015.0+4926	3.300E-011	2.50	1H1013+498	bll
2FHLJ2056.7+4939	1.100E-011	2.33	RGBJ2056+496	bculI
2FHLJ2347.1+5142	2.620E-011	1.85	1ES2344+514	bll
2FHLJ0048.0+5449	7.640E-012	1.30	1RXSJ004754.5+544758	bculI
2FHLJ0431.2+5553e	4.939E-011	1.66	SNRG150.3+4.5	snr
2FHLJ2323.4+5848	1.640E-011	2.45	CasA	snr
2FHLJ2000.1+6508	5.259E-011	1.89	1ES1959+650	bll
2FHLJ0507.9+6737	4.319E-011	2.15	1ES0502+675	bll
2FHLJ0153.5+7113	5.059E-012	1.61	TXS0149+710	bculI

Table 4.2: Sources selected from second Fermi high energy catalogue, which are visible at MACE telescope site and satisfy the criteria defined in the text

#### 4.5.4 MACE present status

The mechanical structure of MACE telescope was first installed at the manufacturing place, Hyderabad, South India in the year 2014. Thereafter the installation was started at Hanle. It was halted by the end of November 2015 due to extremely harsh weather conditions. It is to be noted that the minimum recorded temperature in Hanle is -24°. Figure 4.17. shows the mechanical structure of the MACE telescope at Hanle in November 2015 and 16 Octobre 2016).



Figure 4.17: The left panel shows the installation of MACE 21m diameter dish at Hanle in November 2015. The right panel shows it on October 16, 2016

---



# **5**

## **Conclusion and Future outlook**

## 5. CONCLUSION AND FUTURE OUTLOOK

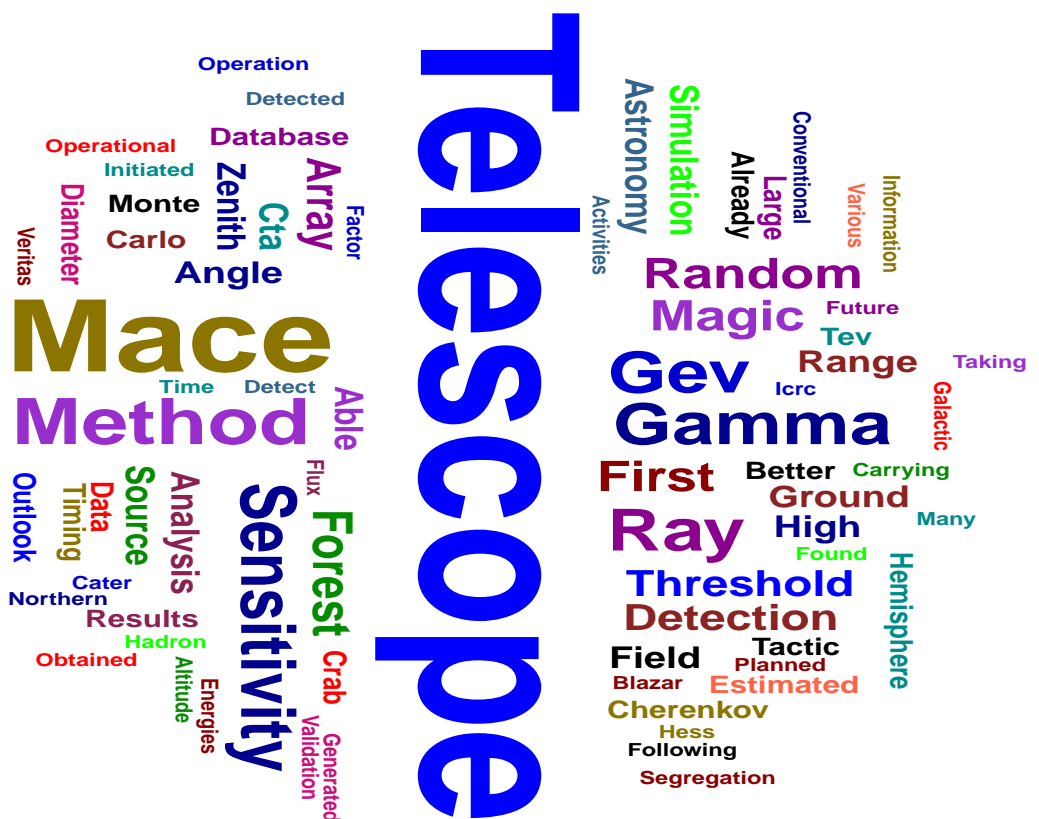


Figure 5.1: Summary of Chapter 5. The size of word represents the number frequency.

---

In this thesis, we have estimated the integral sensitivity of MACE telescope by carrying out the  $\gamma$ -hadron segregation using the Random Forest method. Since the MACE telescope will start operation after sometime, it was planned to apply and validate the Random Forest method on already operational telescope TACTIC installed in Mount Abu, Rajasthan, India. Therefore, the first part of this thesis was devoted to demonstrate the superiority of Random Forest method vis-a-vis various machine learning methods and thereafter, its validation by using the TACTIC observational data. The Random Forest method was validated by re-analysing the Markarian 421 (Mrk 421) data collected by the TACTIC -ray telescope during December 07, 2005 - April 30, 2006. The Application of this method led to an improvement in the signal detection strength by 26% along with a 18% increase in detected rays compared to the conventional Dynamic Supercuts method. After the validation of Random Forest method, the sensitivity of MACE telescope was estimated by using a substantially large simulation database. It was observed that the conventional method for  $\gamma$ -hadron segregation breaks down at  $\sim 140$  GeV. We obtained following results for the MACE telescope by using a Monte Carlo Simulation database generated at  $5^\circ$  zenith angle:

- Due to its high altitude ( $\sim 4200$ m), MACE telescope is able to achieve an analysis energy threshold of 38 GeV for image intensities above 50 photoelectrons.
- The integral sensitivity for point like sources with Crab Nebula-like spectrum above 38 GeV is  $\sim 2.7\%$  of Crab Nebula flux at  $5 \sigma$  statistical significance level in 50 hrs of observation.
- The sensitivity of the MACE telescope below 150 GeV ( $\gamma$ -ray energy) is better than

## 5. CONCLUSION AND FUTURE OUTLOOK

---

the MAGIC-I telescope.

- The MACE telescope will be able to detect many astrophysical sources available from second Fermi high energy catalogue visible from the Hanle altitude (Figure 4.14).

### 5.1 Future outlook

#### 5.1.1 Planned activities

In order to estimate the sensitivity of the MACE telescope in all the zenith angle ranges, we are generating a similar Monte Carlo simulation database. We will be taking up following activities:

- A large Monte Carlo simulation database consisting of more than 1 billion showers has already been generated at  $30^\circ$  and  $40^\circ$  zenith angle each. The sensitivity of MACE telescope will be estimated in low ( $< 30^\circ$ ) as well as high zenith angle ( $> 30^\circ$ ) ranges.
- The energy reconstruction will be carried out by using the Random Forest method.
- It has been shown by the MAGIC group that for a single dish telescope, by using the timing information, background gets reduced by a factor two, which in turn results in an enhancement of about a factor 1.4 of the flux sensitivity to point-like sources [145]. We have also initiated a study to include the timing information of the Cherenkov pulses in estimating the revised sensitivity of the MACE telescope.

### 5.1.2 Outlook

The operational IACT based telescopes like MAGIC, HESS, VERITAS have revolutionized the field of ground based high energy  $\gamma$ -ray astronomy. The last International conference on Cosmic Rays (ICRC2015) [146], announced many spectacular discoveries like first gravitationally lensed blazar detected at the VHE energies, the first evidence of the detection of a PeVatron at the Galactic Center, the detection of the most distant blazar at TeV energies with a redshift of  $z=0.939$ , first morphological study of a SNR interacting with a molecular cloud, the first detection of a superbubble (in the LMC), first detection of pulsed emission from the Crab pulsar above 1 TeV etc. One of the most exciting developments right now in the field of ground based  $\gamma$ -ray astronomy is taking shape is the form of CTA (Cherenkov Telescope Array) [147]. CTA is an array of about  $\sim 50 - 100$  Cherenkov telescopes at the northern hemispheres with an emphasis to study extragalactic objects and another array at Southern hemisphere to concentrate galactic sources. The array will consist of telescopes of various diameters to cater to the wide energy range of few tens of GeV to  $> 100$  TeV. A compact array of  $4 \times 23$  m diameter telescopes will cater to the lower end of the energy range. Apart from the very large field of view of CTA, which will help CTA to operate in survey mode, the analysis energy threshold will be  $\sim 20$  GeV. HESS-II has an analysis energy threshold of  $\sim 50$  GeV. In such a golden era of ground based gamma ray astronomy, the timing of setting up the large diameter (21 m) IACT based telescope by BARC in Northern hemisphere can not be better. We hope to reap the rich dividend in the field of ground based gamma ray astronomy with MACE telescope.



# References

- [1] T. C. WEEKES, M. F. CAWLEY, D. J. FEGAN, ET AL. “Observation of TeV gamma rays from the Crab nebula using the atmospheric Cerenkov imaging technique”. *Astrophys. J.*, **342**, 379–395 (1989).
- [2] V. F. HESS. “ber Beobachtungen der durchdringenden Strahlung bei sieben Freiballonfahrten”. *Physikalische Zeitschrift*, **13**, 1084–1091 (1912).
- [3] [https://www.nobelprize.org/nobel\\_prizes/physics/laureates/1936/hess-bio.html](https://www.nobelprize.org/nobel_prizes/physics/laureates/1936/hess-bio.html).
- [4] D. V. SKOBELZYN. *The Early Stage of Cosmic Ray Particle Research*, pp. 47–52 (Springer Netherlands, Dordrecht, 1985).
- [5] D. SKOBELZYN. “Über eine neue Art sehr schneller  $\beta$ -Strahlen”. *Zeitschrift fur Physik*, **54**, 686–702 (1929).
- [6] D. SKOBELZYN. “Die Intensitätsverteilung in dem Spektrum der  $\gamma$ -Strahlen von Ra C”. *Zeitschrift fur Physik*, **43**, 354–378 (1927).
- [7] R. A. MILLIKAN AND C. D. ANDERSON. “Cosmic-Ray Energies and Their Bearing on the Photon and Neutron Hypotheses”. *Physical Review*, **40**, 325–328 (1932).
- [8] C. D. ANDERSON. “The Apparent Existence of Easily Deflectable Positives”. *Science*, **76**, 238–239 (1932).
- [9] C. D. ANDERSON. “The Positive Electron”. *Physical Review*, **43**, 491–494 (1933).
- [10] P. AUGER, P. EHRENFEST, R. MAZE, J. DAUDIN, AND R. A. FRÉON. “Extensive Cosmic-Ray Showers”. *Reviews of Modern Physics*, **11**, 288–291 (1939).
- [11] G. T. ZATSEPIN AND V. A. KUZ’MIN. “Upper Limit of the Spectrum of Cosmic Rays”. *Soviet Journal of Experimental and Theoretical Physics Letters*, **4**, 78 (1966).
- [12] <http://www.cosmic-ray.org/resprojects.html>.
- [13] [http://www.icrr.u-tokyo.ac.jp/as/project/agasa\\_org.html](http://www.icrr.u-tokyo.ac.jp/as/project/agasa_org.html).
- [14] R. U. ABBASI, T. ABU-ZAYYAD, M. ALLEN, ET AL. “First Observation of the Greisen-Zatsepin-Kuzmin Suppression”. *Physical Review Letters*, **100**(10), 101101 (2008).

## REFERENCES

---

- [15] M. LONGAIR. *High Energy Astrophysics: Volume 1, Particles, Photons and their Detection* (Cambridge University Press, 1992).
- [16] T. K. GAISSER. *Cosmic Rays And Particle Physics* (Cambridge University Press, 1990).
- [17] K. GREISEN. “End to the Cosmic-Ray Spectrum?” *Phys. Rev. Lett.*, **16**, 748–750 (1966).
- [18] D. BERGMAN. “Observation of the GZK Cutoff Using the HiRes Detector”. *Nuclear Physics B - Proceedings Supplements*, **165**, 19 – 26 (2007).
- [19] T. C. WEEKES. *Very high energy gamma-ray astronomy* (2003).
- [20] P. MORRISON. “On gamma-ray astronomy”. *Il Nuovo Cimento (1955-1965)*, **7**(6), 858–865 (2007).
- [21] <http://heasarc.gsfc.nasa.gov/docs/heasarc/missions/explorer11.html>.
- [22] G. COCCONI. “An air shower telescope and the detection of  $10^{12}$  eV photon sources”. *International Cosmic Ray Conference*, **2**, 309 (1960).
- [23] G. ZATSEPIN AND A. CHUDAKOV. “On the methods of searching for local sources of high energy photons”. *Journal of Experimental and Theoretical Physics*, **41**(3), 655 (1961).
- [24] R. MIRZOYAN. “Brief history of ground-based very high energy gamma-ray astrophysics with atmospheric air Cherenkov telescopes”. *Astroparticle Physics*, **53**, 91 – 99 (2014). Centenary of cosmic ray discovery.
- [25] M. F. CAWLEY, D. J. FEGAN, K. HARRIS, ET AL. “A high resolution imaging detector for TeV gamma-ray astronomy”. *Experimental Astronomy*, **1**, 173–193 (1990).
- [26] A. M. HILLAS. “Cerenkov light images of EAS produced by primary gamma”. In F. C. JONES, ed., “International Cosmic Ray Conference”, vol. 3 of *International Cosmic Ray Conference*, pp. 445–448 (1985).
- [27] <http://www.cbpf.br/~icrc2013/>.
- [28] J. HOLDER. “Ground-Based Gamma Ray Astronomy”. *Brazilian Journal of Physics, arXiv eprints 1407.1080*, **44**, 450–464 (2014).
- [29] A. BYKOV, N. GEHRELS, H. KRAWCZYNSKI, ET AL. “Particle Acceleration in Relativistic Outflows”. *Space Science Review, arXiv eprints 1205.2208*, **173**, 309–339 (2012).
- [30] L. BERGSTRÖM AND H. SNELLMAN. “Observable monochromatic photons from cosmic photino annihilation”. *Phys. Rev. D*, **37**, 3737–3741 (1988).
- [31] F. M. RIEGER, E. DE OÑA-WILHELM, AND F. A. AHARONIAN. “TeV astronomy”. *Frontiers of Physics, arXiv eprints 1302.5603*, **8**, 714–747 (2013).
- [32] G. AMELINO-CAMELIA, J. ELLIS, N. E. MAVROMATOS, D. V. NANOPoulos, AND S. SARKAR. “Tests of quantum gravity from observations of  $\gamma$ -ray bursts”. *Nature, arXiv eprints 9712103*, **393**, 763–765 (1998).

## REFERENCES

---

- [33] S. FUNK. “Ground- and Space-Based Gamma-Ray Astronomy”. *Annual Review of Nuclear and Particle Science, arXiv eprints 1508.05190*, **65**, 245–277 (2015).
- [34] G. B. RYBICKI AND A. P. LIGHTMAN. *Radiative Processes in Astrophysics* (Wiley, 1979).
- [35] P. V. RAMANA MURTHY AND A. W. WOLFENDALE. *Gamma-ray astronomy* (Cambridge Astrophysics Series, Cambridge: University Press, 1986, 1986).
- [36] G. R. BLUMENTHAL AND R. J. GOULD. “Bremsstrahlung, Synchrotron Radiation, and Compton Scattering of High-Energy Electrons Traversing Dilute Gases”. *Rev. Mod. Phys.*, **42**, 237–270 (1970).
- [37] <http://www.cv.nrao.edu/course/astr534/InverseCompton.html>.
- [38] M. HARWIT. *Astrophysical Concepts* (1988).
- [39] R. SCHLICKEISER. *Cosmic Ray Astrophysics* (2002).
- [40] T. PADMANABHAN. *Theoretical Astrophysics: Volume 1, Galaxies and Cosmology*. Theoretical Astrophysics (Cambridge University Press, 2000).
- [41] Y. UCHIYAMA, T. TAKAHASHI, F. A. AHARONIAN, AND J. R. MATTOX. “ASCA View of the Supernova Remnant  $\gamma$  Cygni (G78.2+2.1): Bremsstrahlung X-Ray Spectrum from Loss-flattened Electron Distribution”. *ApJ*, **571**, 866–875 (2002).
- [42] M. G. HAUSER AND E. DWEK. “The Cosmic Infrared Background: Measurements and Implications”. *Ann. Rev. Astronomy Astrohysics*, **39**, 249–307 (2001).
- [43] [http://www.springer.com/in/book/9783642809538?wt\\_mc=ThirdParty.SpringerLink.3.EPR653.Abo](http://www.springer.com/in/book/9783642809538?wt_mc=ThirdParty.SpringerLink.3.EPR653.Abo)
- [44] E. DWEK AND F. KRENNRICH. “The extragalactic background light and the gamma-ray opacity of the universe”. *Astroparticle Physics*, **43**, 112–133 (2013).
- [45] J. ZHANG, E.-W. LIANG, S.-N. ZHANG, AND J.-M. BAI. “Radiation Mechanisms and Physical Properties of GeV-TeV BL Lac Objects”. *ArXiv, e-prints 1108.0146* (2011).
- [46] A. DOMNGUEZ, J. D. FINKE, F. PRADA, ET AL. “Detection of the Cosmic -Ray Horizon from Multiwavelength Observations of Blazars”. *The Astrophysical Journal*, **770**(1), 77 (2013).
- [47] M. PUNCH, C. W. AKERLOF, M. F. CAWLEY, ET AL. “Detection of TeV photons from the active galaxy Markarian 421”. *Nature*, **358**, 477 (1992).
- [48] J. QUINN, C. W. AKERLOF, S. BILLER, ET AL. “Detection of Gamma Rays with E greater than 300 GeV from Markarian 501”. *Astrophys. J.l*, **456**, L83 (1996).
- [49] M. CATANESE, C. W. AKERLOF, H. M. BADRAN, ET AL. “Discovery of Gamma-Ray Emission above 350 GeV from the BL Lacertae Object 1ES 2344+514”. *ApJ*, **501**, 616–623 (1998).
- [50] F. AHARONIAN, A. AKHPERJANIAN, J. BARRIO, ET AL. “Evidence for TeV gamma ray emission from Cassiopeia A”. *A&A*, **370**, 112–120 (2001).

## REFERENCES

---

- [51] P. M. CHADWICK, K. LYONS, T. J. L. MCCOMB, ET AL. “PKS 2155-304 - a source of VHE  $\gamma$ -rays”. *Astroparticle Physics*, **11**, 145–148 (1999).
- [52] Y. I. NESHPOR, A. A. STEPANYAN, O. P. KALEKIN, ET AL. “Blazar 3C 66A: Another extragalactic source of ultra-high-energy gamma-ray photons”. *Astronomy Letters*, **24**, 134–138 (1998).
- [53] Y. I. NESHPOR, N. N. CHALENKO, A. A. STEPANIAN, ET AL. “BL Lac: A New Ultrahigh-Energy Gamma-Ray Source”. *Astronomy Reports*, **45**, 249–254 (2001).
- [54] <http://tevcat.uchicago.edu/>.
- [55] W. B. ATWOOD, A. A. ABDO, M. ACKERMANN, ET AL. “The Large Area Telescope on the Fermi Gamma-Ray Space Telescope Mission”. *ApJ, arXiv eprints 0902.1089*, **697**, 1071–1102 (2009).
- [56] MIGUEL MOSTAFÁ FOR THE HAWC COLLABORATION. “The High Altitude Water Cherenkov Observatory”. *ArXiv e-print 1310.7237* (2013).
- [57] HAWC COLLABORATION, A. U. ABEYSEKARA, R. ALFARO, ET AL. “The HAWC Gamma-Ray Observatory: Design, Calibration, and Operation”. *ArXiv e-print 1310.0074* (2013).
- [58] HAWC COLLABORATION, A. U. ABEYSEKARA, R. ALFARO, ET AL. “The HAWC Gamma-Ray Observatory: Observations of Cosmic Rays”. *ArXiv e-print 1310.0075* (2013).
- [59] HAWC COLLABORATION, A. U. ABEYSEKARA, R. ALFARO, ET AL. “The HAWC Gamma-Ray Observatory: Sensitivity to Steady and Transient Sources of Gamma Rays”. *ArXiv e-prints 1310.0071* (2013).
- [60] A. A. ABDO, B. ALLEN, D. BERLEY, ET AL. “TeV Gamma-Ray Sources from a Survey of the Galactic Plane with Milagro”. *ApJL, arXiv eprints 0705.0707*, **664**, L91–L94 (2007).
- [61] R. ATKINS, W. BENBOW, D. BERLEY, ET AL. “TeV Gamma-Ray Survey of the Northern Hemisphere Sky Using the Milagro Observatory”. *ApJ*, **608**, 680–685 (2004).
- [62] A. CARRAMIÑANA AND FOR THE HAWC COLLABORATION. “First year results of the High Altitude Water Cherenkov observatory”. *ArXiv e-prints 1609.01768* (2016).
- [63] M. TAVANI, A. BULGARELLI, V. VITTORINI, ET AL. “Discovery of Powerful Gamma-Ray Flares from the Crab Nebula”. *Science, arXiv eprints 1101.2311*, **331**, 736 (2011).
- [64] <http://www.astronomerstelegram.org/?read=8922>.
- [65] J. HINTON. “Ground-based gamma-ray astronomy with Cherenkov telescopes”. *New Journal of Physics*, **11**(5), 055005 (2009).
- [66] J. HINTON AND W. HOFFMAN. “Teraelectronvolt Astronomy”. *Annual Review of Nuclear and Particle Science, arXiv eprints 1508.05190*, **47**, 523–565 (2009).
- [67] P. A. ČERENKOV. “Visible Radiation Produced by Electrons Moving in a Medium with Velocities Exceeding that of Light”. *Physical Review*, **52**, 378–379 (1937).

## REFERENCES

---

- [68] I. E. TAMM AND I. FRANK. “Coherent Radiation of Fast Electrons in a Medium”. *Doklady Akad. Nauk SSSR*, **14**, 107 (1937).
- [69] [http://www.nobelprize.org/nobel\\_prizes/physics/laureates/1958/](http://www.nobelprize.org/nobel_prizes/physics/laureates/1958/).
- [70] <http://www.gae.ucm.es/~emma/docs/tesina/node4.html>.
- [71] K. YADAV. *TeV Gamma-Ray Observations of Mrk421 and H1426+428 with TACTIC Imaging Telescope*. Ph.D. thesis, PhD Thesis (2011).
- [72] J. V. JELLEY, ed. *Cerenkov radiation and its applications* (London: Pergamon Press, London, UK, 1958).
- [73] H. J. VÖLK AND K. BERNLÖHR. “Imaging very high energy gamma-ray telescopes”. *Experimental Astronomy*, **25**, 173–191 (2009).
- [74] <http://www.gae.ucm.es/~emma/docs/tesina/node9.html>.
- [75] <https://www.ikp.kit.edu/corsika/>.
- [76] T. C. WEEKES. “The Atmospheric Cherenkov Imaging Technique for Very High Energy Gamma-ray Astronomy”. *ArXiv, eprints 0508253* (2005).
- [77] V. A. ACCIARI, E. ALIU, T. AUNE, ET AL. “Simultaneous Multiwavelength Observations of Markarian 421 During Outburst”. *ApJ, arXiv eprints 0907.3923*, **703**, 169–178 (2009).
- [78] P. T. REYNOLDS, C. W. AKERLOF, M. F. CAWLEY, ET AL. “Survey of candidate gamma-ray sources at TeV energies using a high-resolution Cherenkov imaging system - 1988-1991”. *ApJ*, **404**, 206–218 (1993).
- [79] R. KOUL, A. K. TICKOO, S. K. KAUL, ET AL. “The TACTIC atmospheric Cherenkov imaging telescope”. *Nuclear Instruments and Methods in Physics Research A*, **578**, 548–564 (2007).
- [80] K. K. YADAV, R. KOUL, A. KANDA, ET AL. “Real-time data acquisition and control system for the 349-pixel TACTIC atmospheric Cherenkov imaging telescope”. *Nuclear Instruments and Methods in Physics Research A*, **527**, 411–422 (2004).
- [81] N. BHATT, K. K. YADAV, A. KANDA, ET AL. “On a single-counts rate stabilization scheme employed in the imaging camera of the TACTIC  $\gamma$ -ray telescope”. *Measurement Science and Technology*, **12**, 167–171 (2001).
- [82] R. J. PROTHEROE, C. L. BHAT, P. FLEURY, ET AL. “Very High Energy Gamma Rays from Markarian 501”. *25th International Cosmic Ray Conference*, **8**, 317 (1997).
- [83] TELESCOPE ARRAY COLLABORATION. “Observations of TeV gamma ray flares from Markarian 501 with the Telescope Array Prototype”. *ArXiv Astrophysics e-prints* (1998).
- [84] P. CHANDRA, K. K. YADAV, R. C. RANNOT, ET AL. “TeV observations of Mrk 421 with the TACTIC  $\gamma$ -ray telescope during 2006-8”. *Journal of Physics G Nuclear Physics*, **37**(12), 125201 (2010).

## REFERENCES

---

- [85] K. K. YADAV, R. C. RANNOT, P. CHANDRA, ET AL. “Search for TeV  $\gamma$ -rays from H1426+428 during 2004–2007 with the TACTIC telescope”. *Journal of Physics G Nuclear Physics*, **36**(8), 085201 (2009).
- [86] S. V. GODAMBE, R. C. RANNOT, P. CHANDRA, ET AL. “Very high energy  $\gamma$ -ray observations of Mrk 501 using the TACTIC imaging  $\gamma$ -ray telescope during 2005–06”. *Journal of Physics G Nuclear Physics*, **35**(6), 065202 (2008).
- [87] S. V. GODAMBE, R. C. RANNOT, K. S. BALIYAN, ET AL. “Very high energy  $\gamma$ -ray and near infrared observations of 1ES2344+514 during 2004–05”. *Journal of Physics G Nuclear Physics*, **34**, 1683–1695 (2007).
- [88] K. K. YADAV, P. CHANDRA, A. K. TICKOO, ET AL. “Observations of TeV  $\gamma$ -rays from Mrk 421 during December 2005 to April 2006 with the TACTIC telescope”. *Astroparticle Physics*, **27**, 447–454 (2007).
- [89] K. K. YADAV, P. CHANDRA, A. K. TICKOO, ET AL. “Observations of TeV  $\gamma$ -rays from Mrk 421 during December 2005 to April 2006 with the TACTIC telescope”. *Astroparticle Physics*, **27**, 447–454 (2007).
- [90] K. K. SINGH, K. K. YADAV, A. K. TICKOO, ET AL. “Search for TeV  $\gamma$ -ray emission from blazar 1ES1218+304 with TACTIC telescope during March–April 2013”. *New Astron. arXiv eprints 1410.2369*, **36**, 1–8 (2015).
- [91] A. K. TICKOO, R. KOUL, R. C. RANNOT, ET AL. “Long term performance evaluation of the TACTIC imaging telescope using 400 h Crab Nebula observation during 2003–2010”. *Pramana*, **82**(3), 585–605 (2014).
- [92] R. K. BOCK, A. CHILINGARIAN, M. GAUG, ET AL. “Methods for multidimensional event classification: a case study using images from a Cherenkov gamma-ray telescope”. *Nuclear Instruments and Methods in Physics Research A*, **516**, 511–528 (2004).
- [93] J. ALBERT AND AND CO-AUTHORS. “Implementation of the Random Forest method for the Imaging Atmospheric Cherenkov Telescope MAGIC”. *Nuclear Instruments and Methods in Physics Research A*, **588**, 424–432 (2008).
- [94] S. OHM, C. VAN ELDIK, AND K. EGBERTS. “ $\gamma$ /hadron separation in very-high-energy  $\gamma$ -ray astronomy using a multivariate analysis method”. *Astroparticle Physics*, **31**, 383–391 (2009).
- [95] A. FIASSON, F. DUBOIS, G. LAMANNA, J. MASBOU, AND S. ROSIER-LEES. “Optimization of multivariate analysis for IACT stereoscopic systems”. *Astroparticle Physics*, **34**, 25–32 (2010).
- [96] F. DUBOIS, G. LAMANNA, AND A. JACHOLKOWSKA. “A multivariate analysis approach for the imaging atmospheric Cherenkov telescopes system H.E.S.S.” *Astroparticle Physics*, **32**, 73–88 (2009).

## REFERENCES

---

- [97] D. HECK, J. KNAPP, J. N. CAPDEVIELLE, G. SCHATZ, AND T. THOUW. “CORSIKA: A Monte Carlo Code to Simulate Extensive Air Showers”. *Forschungszentrum Karlsruhe Report FZKA*, **6019**, 1 (1998).
- [98] M. K. KOUL, A. K. TICKOO, V. K. DHAR, ET AL. “Simulation studies for optimizing the trigger generation criteria for the TACTIC telescope”. *Nuclear Instruments and Methods in Physics Research A*, **646**, 204–218 (2011).
- [99] HEGRA COLLABORATION, A. KONOPELKO, F. AHARONIAN, ET AL. “Detection of gamma rays above 1 TeV from the Crab Nebula by the second HEGRA imaging atmospheric Cherenkov telescope at La Palma”. *Astroparticle Physics*, **4**, 199–215 (1996).
- [100] T. HENGSTEBECK. *Measurement of the energy spectrum of the BL Lac object PG1553+113 with the MAGIC telescope in 2005 and 2006*. Ph.D. thesis (2007).
- [101] <http://STATISTICAhttp://www.statsoftindia.com/>.
- [102] [http://www.stat.berkeley.edu/~breiman/RandomForests/cc\\_software.htm](http://www.stat.berkeley.edu/~breiman/RandomForests/cc_software.htm).
- [103] G. MOHANTY, S. BILLER, D. A. CARTER-LEWIS, ET AL. “Measurement of TeV gamma-ray spectra with the Cherenkov imaging technique”. *Astroparticle Physics*, **9**, 15–43 (1998).
- [104] A. M. HILLAS, C. W. AKERLOF, S. D. BILLER, ET AL. “The Spectrum of Teravolt Gamma Rays from the Crab Nebula”. *ApJ*, **503**, 744–759 (1998).
- [105] M. GAUG. “Detection of atmospheric muon-neutrinos with the AMANDA neutrino telescope”. *DESY-THESIS-2001-022* (2001).
- [106] M. K. KOUL, A. K. TICKOO, V. K. DHAR, ET AL. “Simulation studies for optimizing the trigger generation criteria for the TACTIC telescope”. *Nuclear Instruments and Methods in Physics Research A*, **646**, 204–218 (2011).
- [107] V. K. DHAR, A. K. TICKOO, M. K. KOUL, ET AL. “ANN-based energy reconstruction procedure for TACTIC  $\gamma$ -ray telescope and its comparison with other conventional methods”. *Nuclear Instruments and Methods in Physics Research A*, **606**, 795–805 (2009).
- [108] C. GERSHENSON. “Artificial Neural Networks for Beginners”. *CoRR*, cs.NE/0308031 (2003).
- [109] D. E. RUMELHART, J. L. McCLELLAND, AND C. PDP RESEARCH GROUP, eds. *Parallel distributed processing: explorations in the microstructure of cognition, vol. 1: foundations* (MIT Press, Cambridge, MA, USA, 1986).
- [110] C. M. BISHOP. *Neural Networks for Pattern Recognition* (Oxford University Press, Inc., New York, NY, USA, 1995).
- [111] P. LANGLEY, W. IBA, AND K. THOMPSON. “An Analysis of Bayesian Classifiers”. In “AAAI”, pp. 223–228 (1992).
- [112] N. FRIEDMAN, D. GEIGER, M. GOLDSZMIDT, ET AL. “Bayesian Network Classifiers”. In “Machine Learning”, pp. 131–163 (1997).

## REFERENCES

---

- [113] B. E. BOSEN, I. M. GUYON, AND V. N. VAPNIK. “A training algorithm for optimal margin classifiers”. In “Proceedings of the fifth annual workshop on Computational learning theory”, COLT ’92, pp. 144–152 (ACM, New York, NY, USA, 1992).
- [114] C. CORTES AND V. VAPNIK. “Support Vector Networks”. *Machine Learning*, **20**, 273–297 (1995).
- [115] B. SCHOLKOPF AND A. J. SMOLA. *Learning with Kernels: Support Vector Machines, Regularization, Optimization, and Beyond* (MIT Press, Cambridge, MA, USA, 2001).
- [116] L. BREIMAN. “Random Forests”. *Machine Learning*, **45**(1), 5–32 (2001).
- [117] L. BREIMAN. “Technical Note: Some Properties of Splitting Criteria”. *Machine Learning*, **24**(1), 41–47 (1996).
- [118] D. T. “Technical Note: Some Properties of Splitting Criteria”. *Machine Learning*, **24**(1), 1–22 (1998).
- [119] <http://cran.r-project.org/>.
- [120] T. FAWCETT. “An introduction to ROC analysis”. *Pattern Recognit. Lett.*, **27**(8), 861–874 (2006).
- [121] J. P. EGAN. *Signal detection theory and ROC analysis*. Series in Cognition and Perception (Academic Press, New York, NY, 1975).
- [122] J. A. SWETS. “Measuring the Accuracy of Diagnostic Systems”. *Science*, **240**, 1285–1293 (1988).
- [123] T.-P. LI AND Y.-Q. MA. “Analysis methods for results in gamma-ray astronomy”. *ApJ*, **272**, 317–324 (1983).
- [124] J. DAVIS AND M. GOADRICH. “The relationship between Precision-Recall and ROC curves”. In “Proceedings of the 23rd international conference on Machine learning”, ICML ’06, pp. 233–240 (ACM, New York, NY, USA, 2006).
- [125] A. HOECKER, P. SPECKMAYER, J. STELZER, ET AL. “TMVA: Toolkit for Multivariate Data Analysis”. *PoS*, **ACAT**, 040 (2007).
- [126] J. ALEKSIĆ, H. ANDERHUB, L. A. ANTONELLI, ET AL. “MAGIC TeV gamma-ray observations of Markarian 421 during multiwavelength campaigns in 2006”. *Astronomy & Astrophysics*, **519**, A32 (2010).
- [127] D. HORAN, V. A. ACCIARI, S. M. BRADBURY, ET AL. “Multiwavelength Observations of Markarian 421 in 2005-2006”. *Astrophys. J.*, **695**, 596–618 (2009).
- [128] HEGRA COLLABORATION, A. KONOPELKO, F. AHARONIAN, ET AL. “Detection of gamma rays above 1 TeV from the Crab Nebula by the second HEGRA imaging atmospheric Cherenkov telescope at La Palma”. *Astroparticle Physics*, **4**, 199–215 (1996).
- [129] M. REIDMILLER. *Computer Standards Interfaces*, **16**, 265 (1994).

## REFERENCES

---

- [130] J. HOLDER, R. W. ATKINS, H. M. BADRAN, ET AL. “The first VERITAS telescope”. *Astroparticle Physics*, **25**, 391–401 (2006).
- [131] J. HOLDER AND FOR THE VERITAS COLLABORATION. “Latest Results from VERITAS: Gamma 2016”. *ArXiv e-prints* (2016).
- [132] C. VAN ELDIK FOR HESS COLLABORATION. personal communication, 2016.
- [133] C. STEGMANN AND H. E. S. S. COLLABORATION. “Highlights from H.E.S.S.” In F. A. AHARONIAN, W. HOFMANN, AND F. M. RIEGER, eds., “American Institute of Physics Conference Series”, vol. 1505 of *American Institute of Physics Conference Series*, pp. 194–201 (2012).
- [134] M. ACTIS, G. AGNETTA, F. AHARONIAN, ET AL. “Design concepts for the Cherenkov Telescope Array CTA: an advanced facility for ground-based high-energy gamma-ray astronomy”. *Experimental Astronomy*, **32**, 193–316 (2011).
- [135] C. BORWANKAR, N. BHATT, S. BHATTACHARYYA, ET AL. “Simulation studies of MACE-I: Trigger rates and energy thresholds”. *Astroparticle Physics*, **84**, 97 – 106 (2016).
- [136] F. A. AHARONIAN, A. G. AKHPERJANIAN, J. A. BARRIO, ET AL. “The Energy Spectrum of TEV Gamma Rays from the Crab Nebula as Measured by the HEGRA System of Imaging Air Cerenkov Telescopes”. *ApJ*, **539**, 317–324 (2000).
- [137] C. S. STALIN, M. HEGDE, D. K. SAHU, ET AL. “Night sky at the Indian Astronomical Observatory during 2000–2008”. *Bulletin of the Astronomical Society of India*, **36**, 111–127 (2008).
- [138] J. ALBERT AND AND CO-AUTHORS. “Implementation of the Random Forest method for the Imaging Atmospheric Cherenkov Telescope MAGIC”. *Nuclear Instruments and Methods in Physics Research A*, **588**, 424 (2008).
- [139] M. SHARMA, J. NAYAK, M. KRISHNA KOUL, S. BOSE, AND A. MITRA. “Gamma/hadron segregation for a ground based imaging atmospheric Cherenkov telescope using machine learning methods: Random Forest leads”. *Research in Astronomy and Astrophysics*, **14**, 1491-1503 (2014).
- [140] S. HAINO, T. SANUKI, K. ABE, ET AL. “Measurements of primary and atmospheric cosmic-ray spectra with the BESS-TeV spectrometer”. *Physics Letters B*, **594**, 35–46 (2004).
- [141] B. WIEBEL-SOOTH, P. L. BIERMANN, AND H. MEYER. “Cosmic rays. VII. Individual element spectra: prediction and data”. *aap*, **330**, 389–398 (1998).
- [142] J. ALEKSIĆ, S. ANSOLDI, L. A. ANTONELLI, ET AL. “The major upgrade of the MAGIC telescopes, Part II: A performance study using observations of the Crab Nebula”. *Astroparticle Physics*, **72**, 76–94 (2016).
- [143] J. ALBERT, E. ALIU, H. ANDERHUB, ET AL. “VHE -Ray Observation of the Crab Nebula and its Pulsar with the MAGIC Telescope”. *The Astrophysical Journal*, **674**(2), 1037 (2008).
- [144] M. ACKERMANN, M. AJELLO, W. B. ATWOOD, ET AL. “2FHL: The Second Catalog of Hard Fermi-LAT Sources”. *ApJS*, **222**, 5 (2016).

## REFERENCES

---

- [145] E. ALIU, H. ANDERHUB, L. A. ANTONELLI, ET AL. “Improving the performance of the single-dish Cherenkov telescope MAGIC through the use of signal timing”. *Astroparticle Physics*, **30**, 293–305 (2009).
- [146] M. LEMOINE-GOUMARD. “Status of ground-based gamma-ray astronomy”. *ArXiv, e-prints:1510.01373* (2015).
- [147] <https://portal.cta-observatory.org/Pages/Home.aspx/>.